TEL AVIV UNIVERSITY אוניברסיטת תל-אביב

RAYMOND AND BEVERLY SACKLER
FACULTY OF EXACT SCIENCES
SCHOOL OF PHYSICS & ASTRONOMY

הפקולטה למדעים מדוייקים
ע"ש ריימונד ובברלי סאקלר
בית הספר לפיסיקה ואסטרונומיה

LINE AND CONTINUUM VARIABILITY, AND SIZE-MASS-LUMINOSITY RELATIONSHIPS IN ACTIVE GALACTIC NUCLEI

THESIS SUBMITTED FOR THE DEGREE "DOCTOR OF PHILOSOPHY"

by

Shai Kaspi

SUBMITTED TO THE SENATE OF TEL-AVIV UNIVERSITY

August 1999

This work was carried out under the supervision of

Professor Hagai Netzer

School of Physics and Astronomy

Tel-Aviv University

This work is dedicated to the memory of my brother Ronen and of my father Shaul Kaspi, who both helped and encouraged me in the course of this work but unfortunately never saw its completion.

Contents

Abstract

This work is aimed at measuring the size of the broad line region (BLR) in active galactic nuclei (AGNs) and establishing experimental relations between the luminosity, mass, and BLR size in such objects. It contains new observational results as well as data from the literature, and includes also new theoretical models of AGNs.

The second chapter of the thesis presents the results of an intensive ground-based spectrophotometric campaign to monitor the Seyfert galaxy NGC 4151. No evidence for a time lag between the optical continuum and the UV continuum and emission lines has been found. For the Hα and Hβ emission lines, we find a time lag of $0-3$ days; very different from past results where a time lag of 9 ± 2 days was found for both lines. This may be due to a different variability timescale of the *ionizing* continuum, or to a real change in the BLR gas distribution.

Results of 7.5 years of spectrophotometric monitoring of 28 Palomar-Green quasars are reported in chapter three. The typical sampling intervals are 1–4 months with typically 20–70 observing epochs per object. All sources show continuum and emission line variations, and all 17 objects with adequate sampling show Balmer line variations that follow the continuum variations with time lags of order 100 days. This work increases the available luminosity range for studying the size-mass-luminosity relations in AGNs by two orders of magnitude and doubles the number of objects suitable for such studies. Combining the results for the 17 quasars with previously obtained data for 17 Seyfert 1 galaxies in chapter four, we find that the BLR size scales with the 5100 Å luminosity as $L^{0.70\pm0.03}$, significantly different from previous studies and from simple theoretical predictions. This suggests that the effective ionization parameter in AGNs may be a decreasing function of luminosity. Assuming gravitationally dominated motions of the line emitting gas, the central mass scales with the 5100 Å luminosity as $M \propto L^{0.5\pm0.1}$. This is inconsistent with all AGNs having optical luminosity that is a constant fraction of the Eddington luminosity. There is also an anticorrelation between the full-width at half maximum (FWHM) of the Balmer lines and the AGN luminosity, such that $v_{FWHM} \propto L^{-0.27\pm0.01}$.

Finally, chapter five presents a new scheme for modeling the BLR. This involves photoionization calculations of a large number of clouds, in several pre-determined geometries, and a comparison of the calculated line intensities with observed emission line light curves. Fitting several observed light curves simultaneously provides strong constraints on model parameters such as the run of density and column density across the nucleus, the shape of the ionizing continuum, and the radial distribution of the emission line clouds. Applying the model to the Seyfert 1 galaxy NGC 5548 enables us to successfully reconstruct four ultraviolet emission-line light curves.

Acknowledgments

I sincerely thank my thesis supervisor, Prof. Hagai Netzer for his guidance, support and encouragement in the course of this work.

I also thank Prof. Dan Maoz for his support, the many enlightening discussions, and for introducing me to the observational work.

A special thanks goes to Prof. Brad Peterson for his cooperation and the many discussions, suggestions and data sets which he provided me with.

I deeply thank my overseas collaborators in the PG monitoring campaign, Drs. Buell Jannuzi and Paul Smith for the countless observing nights they had gone through and their many suggestions and comments.

I am grateful to the Astronomy and Astrophysics faculty members and research associates who have taught me much: Profs. Ben-Zion Kozlovsky, Elia Leibowitz, Tsevi Mazeh, Yoel Refhaeli, and Amiel Sternberg, and Drs. Elhanan Almoznino, Sara Beck, Noah Brosch, Marcella Contini, Liliana Formiggini, Itzhak Goldman, Amir Levinson, and Haim Mendelson.

I have benefited a lot from the help of my fellow students and from our many discussions. This thanks goes to Benny Belinko, Avishay Gal-Yam, Uri Giveon, Ana Heller, Orly Kovo, Yiftah Lipkin, Eyal Neistein, Eran Ofek, Ohad Shemmer, Doron Shlush, Susy Steindling, and Drs. Tal Alexander, Oleg Goldshmidt, Alon Retter, and Amnon Stupp.

I am indebted to the Wise Observatory staff: Sammy Ben-Guigui, John Dann, Dr. Peter Ibbetson, and Ezra Mashal, for their dedicated assistance with the observations.

Friedel Loinger is thanked for her support and administrating the computer network which I have extensively used. I am grateful to Sylvia Navon, and Margie Goss for their many administrative actions and advices.

My family deserves special thanks for their support during the past years, and for nursing me during many observing nights at the Wise Observatory.

I acknowledge financial support by the School of Physics and Astronomy at Tel-Aviv University, the Israel Science Foundation, the Jake Adler Chair of Extragalactic Astronomy, and the Colton Scholarships.

This work has done extensive use of NASA's Astrophysics Data System (ADS) Abstract Service, and the NASA/IPAC Extragalactic Database (NED).

Chapter 1

Introduction

1.1 Active Galactic Nuclei Phenomenology

Active Galactic Nuclei (AGNs) are a class of astronomical objects, situated in otherwise normal galaxies, in which violent processes, unrelated to ordinary stellar processes, are taking place. Examples for such processes are: high energy output from a very compact nuclear region, nonstellar continuum emission, nuclear emission-lines from gas which is excited by this continuum, variable continuum and/or emission lines, and polarization of the emitted radiation.

A typical AGN is characterized by a central unresolved energy source which emits a nonstellar continuum that extends from the radio to the γ-ray and can exceed the luminosity of the host galaxy by a large amount. Emission lines are seen in almost all AGNs with widths that are attributed to gas motions with velocities of $\sim$100 to $\sim$10000 $\mathrm{km\,s^{-1}}$.

There are many subclasses of AGNs that can be defined in various ways and in different astronomy wavelength bands.

• At the high luminosity end we find the quasars with luminosity of order $10^{44} - 10^{47}$ ergs $\mathrm{s^{-1}}$ and redshifts between $\sim 0.1-5$. Quasar spectra show broad ($3000-5000$ $\mathrm{km\,s^{-1}}$) permitted emission lines reaching up to $\sim 0.1c$ full width at zero intensity. Strong narrow ($400-1000$ $\mathrm{km\,s^{-1}}$) permitted and forbidden lines are observed in lower luminosity objects but are not so common in the brighter quasars. Quasars are further divided into radio-loud and radio-quiet. The two groups differ in their radio properties as well as in the ratio of optical to X-ray luminosity.

• At the middle luminosity scale we find the Seyfert galaxies, which are divided into two types: type 1 which have broad permitted emission lines and narrow forbidden emission lines, and type 2 which show narrow emission lines and do not have prominent broad emission lines. Seyfert 1s have luminosities of $\sim 10^{44}$ ergs s^{-1} and their spectrum resemble the quasars spectrum (but with two orders of magnitude lower in luminosity). Seyfert 2s have luminosities of $\sim 10^{43}$ ergs s^{-1}.

• At the very faint end we find the Low Ionization Nuclear Emission Line Regions (LINERs) with luminosities of order 10^{41} ergs s^{-1}. LINERs are all nearby objects. The strongest emission lines in their spectra are narrow, resembling, in many ways, Seyfert 2 spectra but with much lower luminosity. Some LINERs show weak broad emission lines.

• Several other subclasses and names are BL-Lac objects, Optically Violent Variables, broad and narrow line radio galaxies, Narrow Line X-ray Galaxies (NLXGs) and more (e.g., Lawrence 1987, Woltjer 1990, Netzer 1990).

The estimated total number of quasars with $m_B < 21$ is $\sim 1.5 \times 10^6$ (Boyle et al. 1987), about 10% of all galaxies are Seyfert galaxies, and about 30% of all galaxies are LINERs. Thus, while quasars are rare, the AGN phenomenon as a whole is quite common.

As mentioned, there are two prominent components in AGNs spectra. The first is the nonstellar continuum which can be fitted, over a limited wavelength range, by a simple power law of the form: $F_\nu \propto \nu^{-\alpha}$, where F_ν is the monochromatic flux at frequency ν. α, the spectral index, is different for each wavelength range and subclass, but in many AGNs (in particular quasars and Seyfert 1s) $\alpha \approx 1 - 1.2$ in the IR range, $\alpha \approx 0.3 - 0.7$ in the optical, and $\alpha \approx 0.9$ at hard X-rays. In the radio wavelength range, there are two categories of AGNs "steep spectrum" and "flat spectrum". The separation takes place at around $\alpha \approx 0.4$ (at 1 GHz).

The second spectral component consists of the strong emission lines. The common lines are due to hydrogen ($L\alpha$, $H\alpha$ and $H\beta$), oxygen (e.g. $OVI\lambda1035$, $[OIII]\lambda5007$), carbon (e.g. $CIII\lambda977$, $CIV\lambda1549$, $CIII]\lambda1909$), helium, magnesium and many iron lines. Regarding the line width, there are two distinct categories: broad emission-lines with $3000 < FWHM < 10,000$ km s^{-1} (those are usually the permitted and semi-forbidden lines), and narrow emission-lines with $300 < FWHM < 1000$ km s^{-1} (usually the forbidden

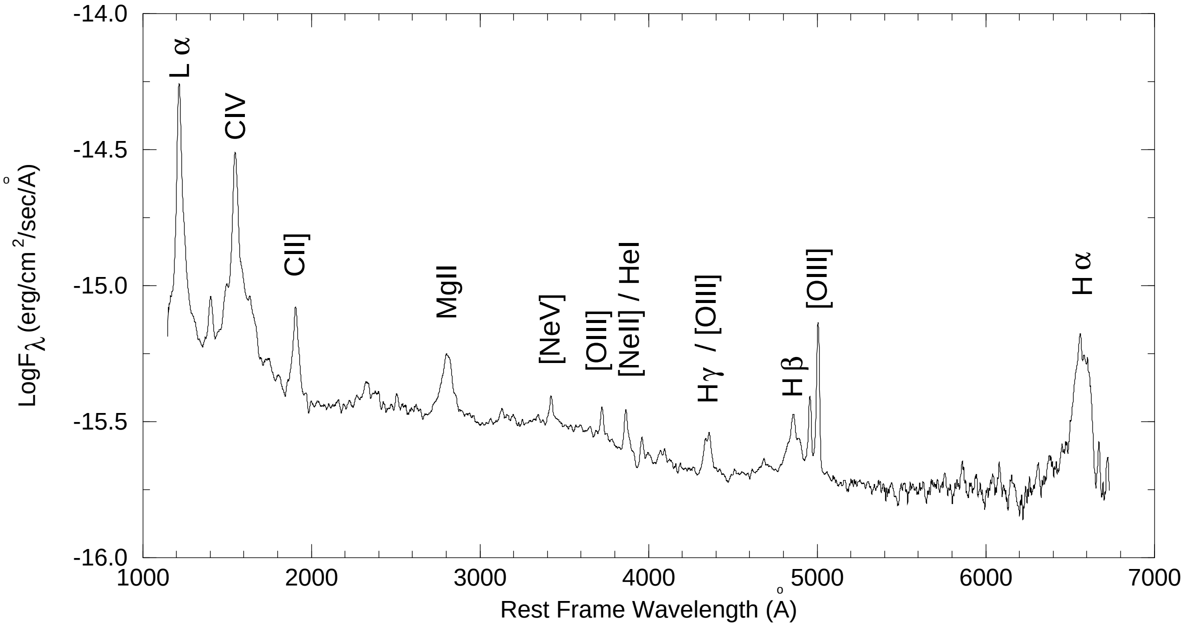

Fig. 1.1.— Spectrum of the radio-loud quasar 3C 215.

lines). A typical spectrum of a radio-load quasar (3C 215) is shown in Figure 1.1, where the distinction between broad lines (e.g., $H\alpha$, $H\beta$) and narrow lines (e.g. $[OIII]$) is very clear. In many AGNs, the profiles show a broad component with a narrow component superimposed on it. Most AGNs show rather similar line ratios, despite of a very large range in continuum luminosity.

AGNs line profiles exhibit a great variety: in some objects different lines have similar profiles while in others the same profiles differ significantly. Some line profiles are symmetric while others are not. Some are smooth while others show a clear multi-component structure. Finally, even the line redshift, as determined from the center of the profile, is not always the same for all lines of a given source. Some of these properties do not seem to be strongly correlate with luminosity while others (e.g. the line redshift) are.

Repeated observations of many AGNs clearly show that the luminosity of most objects changes on different time scales. Furthermore, it was found that changes in the intensity of the continuum flux is often followed by corresponding changes in the strength of the broad emission lines, while the narrow lines do not show such a response. This will be discussed in detail in the body of the thesis. Line profile variations are also observed in some sources (e.g., Gilbert et al. 1999) but this topic is not discussed in this work.

1.2 The Standard Model

The above observations, as well as others not related to emission lines, have resulted in the so-called "standard model" for AGNs. While this working model is still not completely established, it describes many of the observations and represent a broad consensus among researchers in the field. The model includes a black hole which is fed by accretion trough an accretion disk. The release of gravitational energy by the accreted material can roughly explain the observed continuum emission, in luminosity and spectral energy distribution. There are alternative radiation processes that can produce the shape of the observed continuum but they do not seem to explain several of the observed properties. The small size of such "central engines" is consistent with the short variability time scale. For a review of this model see, e.g., Netzer (1990), Waltjer (1990), Blanford (1990), Antonucci (1993), Peterson (1997).

The strong continuum emission originating from the vicinity of the central black hole, photoionizes the gas around it. At a distance of $\sim$ 0.1 pc (which, as we show below, is a function of the source luminosity) we find the "Broad Line Region" (BLR) which is the region emitting the broad emission lines. Further out, at a distance of $\sim$ 100 pc, we find the "Narrow Line Region" (NLR) where the narrow emission lines are produced by similar processes. Photoionization models (see below) and the relative strength of various emission lines indicate that the gas temperature in the BLR is of order 1–3 $\times 10^4$ K and the particle density is $n \geq 10^9$ cm^{-3}. The typical gas density in the NLR is $10^3 - 10^6$ cm^{-3} and the gas temperature is similar to that in the BLR. Under these conditions, the large widths of the lines cannot be explained by thermal motion since the sound speed in a 10^4 K gas amount to only $\sim$ 10 km s^{-1}. A reasonable explanation for the large widths of the emission-lines is Doppler broadening due to bulk motion of the gas.

The BLR is too small to be resolved by any astronomical observations and the main source of information about it comes from emission line studies. The chemical composition of the gas in the BLR and the NLR is roughly known from emission line studies although the analysis of the broad lines is complicated and somewhat uncertain due to the large optical depth in many lines. The general ideas about the BLR structure involve "clouds" that are simply large gas concentrations. Some models suggest giant stars as the BLR clouds, others consider arbitrary dense condensations. The clouds are moving around the black hole in a velocity pattern that is yet unknown. As for the NLR, the model suggests gas clouds that are less dense and slower (to explain the narrowness of the lines). The NLR is spatially resolved in nearby AGNs, e.g. Evans et al. (1993) found a biconial structure for the NLR in NGC 4151. The geometry of the NLR in more distant AGNs is not known.

The standard model explains the emission lines as resulting from photoionization, i.e., the interaction of the central radiation with atoms and ions in the BLR and the NLR. Photoionization can explain most of the emission line fluxes, and the line ratios. Continuum luminosity changes are explained as changes in accretion rate onto the black hole. The variable photoionizing flux results in flux variation of the broad emission lines, with a time delay characteristic of the size of the BLR (the light travel time from the central source to the BLR). Those changes are not seen in the narrow lines since the NLR is three orders of magnitude larger. The large dimension cause the line variations to smear out and represent the mean level of intensity of the central source.

There are attempts to unify several AGNs subclasses into one model called *The Unified Scheme*. Attempts to explain Seyfert 1s and Seyfert 2s diverge into two directions. The first suggests an obscuring torus which surrounds the black hole and the BLR. When observing the AGN from the pole direction, both the BLR and the NLR are seen and the object is classified as a Seyfert 1. When the AGN is observed from the plane of the torus, only the NLR is seen and the AGN is classified as a Seyfert 2. This scheme seems to be successful. In particular, it is confirmed by X-ray observations that, in some cases, penetrate the torus and provide a clear view of the center at high energies. The second approach suggests time evolution of the nucleus. When the nucleus activity is high both the BLR and the NLR are excited and emission lines from both regions are observed. When the nuclear activity is at minimum the broad lines disappear after a short time (the recombination time of the BLR is short due to its high density) but the low density gas in the NLR will show emission lines years later. Hence, the object will turn from Seyfert 1 into Seyfert 2. More speculative attempts are to unify *all* AGNs, including radio loud sources, into one model. Such schemes are far from being complete and there are many features that are currently not explained (see Padovani 1998, Wills 1999, and references therein).

1.3 The Broad Line Region

Since AGNs' central sources are compact and too small to be directly resolved, the BLR is presently the main probe of their inner regions. The dynamics of the BLR gas is determined by gravity and radiation pressure forces, thus the study of line profile is an important source of information. The emitted line spectrum offers a look into the ionizing continuum which is not observable in other ways. The physical structure of the BLR may provide information about the origin of the gas and about the fueling of the central source. Studies of the extended structure (the NLR and beyond) show that, on kiloparsecs scale, AGNs are not spherically symmetric. The origin of this asymmetry may be the asymmetry of the radiation field or, perhaps, something to do with the BLR (absorption or scattering of radiation in certain directions).

1.3.1 BLR Modeling

As the BLRs are not spatially resolved, information about their size, gas distribution, and physics can only be obtained from spectroscopic observations. Understanding the BLRs requires a combination of detailed observations with sophisticated theoretical models.

Photoionization is the most likely excitation mechanism of the line emitting gas for several reasons. AGNs continuum radiation is known to extend well beyond the Lyman edge and can therefore ionize the gas. The systematic time lag between the continuum variability and line variability (see § 1.3.2 below), and the roughly constant line equivalent width in AGNs of similar luminosity, both suggest a causal connection between the continuum and lines. Reliable temperature indicators, such as the C III λ977/C III] λ1909 line ratio, estimate the gas temperature at less than 25000 K, which is not enough to collisionally ionize this ion. Finally, the large range of ionized species is typical of nebula photoionized by a broad band continuum.

Detailed photoionization models of the BLR gas do indeed reproduce, to a fair degree, the observed line spectrum. Those models are usually described in terms of the properties of 'clouds', but it is implicit that this gas may in fact be arranged in anything from spherical clouds (either large or small compared to their ionized depths), to thin sheets, to extended atmospheres, winds or shock-compressed regions surrounding stars, to the surface of accretion disks.

There are number of similar photoionization codes, such as, CLOUDY (Ferland et al. 1998) and ION (Netzer 1996). The input parameters for any of these codes include the ionization continuum flux and the gas density at the illuminated face which are often combined into a single parameter called "the ionization parameter". It is also necessary to specify at least the continuum shape, the dependence of density or pressure on depth, the column density, and the abundances.

One of the important computational limits of these models is their approximate treatment of radiative transfer, usually through the escape probability method (cf. Avrett & Loeser 1988; Collin-Souffrin & Dumont 1989). Probably the most uncertain predictions are the hydrogen Balmer line intensities and the high series of low ionization species like singly ionized magnesium and iron. There are also problems related to interpetation where it is unclear what the input parameters should be. For example, it is not clear what is the input spectrum that the BLR "sees", and this spectrum may depend on the BLR geometry. It is clear that the line spectrum cannot be explained with a one cloud model, and one must consider clouds with a range of densities across the BLR and possibly also in a given location.

Photoionization modeling of the BLR was attempted in the past. Most studies assumed a simple BLR consisting of one or two zones only. Not suprisingly, such models did not produce adequate results. Also, very little has been done to exploit the wealth of information treasured in reverberation mapping archives. While time-averaged spectra of AGNs can reasonably be explained by photoionization models, there is a definite lack of detailed model fittings to actual gas distributions, and motion deduced from modern reverberation studies. In § 5.2.1 we describe and disscuss some of the past studies and contrast them with our own, new detailed models.

1.3.2 Mapping the BLR

The small size of the BLR makes it impossible to get a direct picture, since even in the nearest AGNs the BLR is only several microarcseconds in size. However, it is possible to learn about the BLR in an indirect way by studying the broad line variability. This method, called "reverberation mapping" or "echo mapping", entails detailed comparison of the continuum and the emission line variation to determine the geometry and velocity field of the BLR (see Netzer & Peterson 1997 for a recent review). The method is based on the following assumptions:

1. The ionizing continuum originates in a single, central source with spatial extent of 10–100 gravitational radii, $R_g \approx 1.5 \times 10^{13}(M/10^8 M_\odot)$ cm. This estimate is based on accretion disk models that are generally consistent with the observations.

2. The response time of the BLR clouds to changes in the ionizing flux is much shorter than the light travel time across the BLR. This assumption is supported by a measured light-travel time of days to weeks, and the known recombination time for the BLR gas. densities which is of order 1 hour.

3. The BLR structure and kinematics are constant over the duration of the monitoring period. This places practical time limits on the duration of a single campaign.

4. The observed UV or optical continuum has a simple (though not necessarily linear) relation with the ionizing continuum that drives the line variations.

The first analysis of such reverberation of AGNs' emission-lines was carried out by Bahcall, Kozlovsky, & Salpeter (1972), who calculated the response to the total line intensity in a spherical distribution of gas. They showed that because of the finite light velocity, an external observer will not see the entire emission line region responding instantaneously. A cloud at distance r from the central source and at angle θ to the line of sight will appear to respond after a time

$$t = \frac{r}{c}(1 - \cos\theta) \ . \tag{1.1}$$

The entire region will respond on a time scale characteristic of the light-travel time across the region, r/c. For the spherical distribution of gas, when the recombination time is short, the response to ionizing flux which is constant except in a time interval $0 \le t \le \tau_{on}$, when it is larger by a constant factor (a "boxcar"), the line intensity rises linearly with time for $0 \le t \le \tau_{on}$, is constant for $\tau_{on} < t < 2r/c$, and then decays to its original value in a time τ_{on}, where $r \ge c\tau_{on}/2$ is the radius of the shell.

To calculate the response to a more complicated change in the ionizing flux we need to check the response of the BLR to a flash in the ionizing flux, i.e. a δ-function, and to look at the continuum light curve as a sum of many δ-functions. In the case of a thin shell BLR, the response to a flash in the ionizing flux is as follows: At time t after the flash a distant observer will see emission from a ring of radius $r\sin\theta$ centered on the line of sight, of area $2\pi r^2\sin\theta d\theta$. Since we assume that the gas is optically thick to the ionizing continuum radiation, the energy dE emitted in the lines from the ring is proportional to its area, and the observed intensity I is

$$I(t) = \frac{dE}{dt} \propto \frac{\sin\theta d\theta}{dt} = const \ , \tag{1.2}$$

where the last equality is a result of eq. 1.1. Therefore the response of a shell to a short continuum burst is a "boxcar" function which is constant between $t = 0$, when the part of the BLR on the line of sight is responding, and $t = 2r/c$ when the far side of the BLR responds. This can explain the previous result where a "boxcar" change in the continuum flux was assumed. By dividing this function into many δ-functions, each one producing a "boxcar" variation in the line flux, and summing all those "boxcars", we get the line response described in the previous paragraph.

The same calculation can be done for a ring-shaped BLR of radius r, with axis inclined at an angle i to the line of sight. In cylindrical coordinates coaxial with the ring and origin at the ring center, the delay of line emission emanating from a cloud at azimuthal angle ϕ on the ring is

$$t = \frac{r}{c}(1 - \sin i \cos\phi) \ . \tag{1.3}$$

The area of the ring seen by a distant observer during an interval dt is proportional to $d\phi$, hence

$$I(t) = \frac{dE}{dt} \propto \frac{d\phi}{dt} \propto \frac{1}{\sin\phi} = \frac{1}{\sqrt{1-\cos^2\phi}} = \frac{const.}{\sqrt{\sin^2 i - (1-\frac{ct}{r})^2}}$$
$$\text{for } \tfrac{r}{c}(1-\sin i) \leq t \leq \tfrac{r}{c}(1+\sin i), \text{ and 0 otherwise.} \tag{1.4}$$

Thus the response is double-peaked in time centered on $t = r/c$.

The response of more complicated geometries, such as thick spherical shells and thin disks, to a short continuum flash, can be calculated by integrating the above responses over radius. Also, as noted above, the response of all those geometries to a complicated change in the continuum can be obtained by integrating over the δ-functions assembling it. From those simple examples it can be seen that for each geometry and each change in continuum flux, there is a unique response of the emission lines. Therefore, measuring the continuum and line light curves can result in obtaining the geometry of the BLR. This idea was first introduced and discussed by Blandford and McKee (1982) who refer to the technique as finding the "transfer function".

The transfer function describes the response of an emission-line to a δ-function continuum outburst. The actual continuum behavior in AGNs is complex, and as a result the emission line response is the convolution of the continuum variation and the transfer function. In general, the relationship between the continuum light-curve $C(t)$ and the emission-line light-curve $L(v,t)$ can be described by

$$L(v,t) \;=\; \int_{-\infty}^{\infty} \Psi(v,\tau) C(t-\tau) d\tau \ , \tag{1.5}$$

which is known as the "transfer equation". The aim is usually to use the observables $C(t)$ and $L(v,t)$ to solve this integral equation for $\Psi(v,\tau)$, the transfer function, and thus infer the geometry and kinematics of the BLR. In the original formulation of Blandford and McKee (1982), the transfer function is obtained by Fourier methods using the convolution theorem

$$\tilde{\Psi}(\omega) \;=\; \frac{\tilde{L}(\omega)}{\tilde{C}(\omega)}, \tag{1.6}$$

where $\tilde{L}(\omega)$ is the Fourier transform of $L(t)$, etc., and then transforming $\tilde{\Psi}(\omega)$ back to the time domain. Several theoretical works have studied transfer functions for BLRs with different geometries and velocity fields (e.g., Pérez, Robinson, & de la Fuente 1992, and references therein). However, in practice a stable and unique solution for $\Psi(v,\tau)$ requires a large amount of high-quality data, and this is the main limitation of reverberation mapping. Since high quality spectra of faint objects are not easy to obtain, we will focus on the somewhat simpler problem of solving for the *one-dimensional transfer function* $\Psi(\tau)$, which gives the response of the entire emission line integrated over line-of-sight velocity, i.e.,

$$L(t) \;=\; \int_{-\infty}^{\infty} \Psi(\tau) C(t-\tau) d\tau \ . \tag{1.7}$$

In real situations, solution by Fourier transforms does not work very well since the data are not regularly sampled, and a very large number of points are required (in practice, a transfer function obtained in this way has been published for only one data set, of NGC 4151, by Maoz et al. 1991). However, several other inversion methods have been suggested. They include the maximum entropy method (MEM; Horne 1994; Horne 1997), the subtractive optimally localized averages (SOLA) method (Pijpers & Wanders 1994), and regularized linear inversion (Krolik & Done 1995). All those methods have been tried but did not produce very satisfactory results since high quality data are hard to find and, as argued by Maoz (1997), they do not produce unique transfer functions (i.e., several different geometries can produce the transfer function produced by those methods). Inversion methods will probably do much better when better data sets are available.

1.3.3 Estimating the BLR Size

It is possible to get a fairly good estimate of the BLR size even with lower quality data sets, by cross-correlating the continuum and the emission-line light-curves. This is done in order to find the time shift between the two that maximizes the correlation. This time shift is referred to as the "lag" (for a particular emission line) and represents the first moment of $\Psi(\tau)$. The Cross Correlation Function (CCF) is defined as

$$CCF(\tau) \equiv \int_{-\infty}^{\infty} L(t)C(t-\tau)dt \ . \tag{1.8}$$

Similarly, the continuum Auto-Correlation Function (ACF) is defined as

$$ACF(\tau) \equiv \int_{-\infty}^{\infty} C(t)C(t-\tau)dt \ . \tag{1.9}$$

By using eq. 1.7 for $L(t)$ in eq. 1.8 it is easily shown that

$$CCF(\tau) = \int_{-\infty}^{\infty} \Psi(\tau')ACF(\tau-\tau')d\tau' \tag{1.10}$$

(Penston 1991; Peterson 1993). Thus, the CCF is a convolution of the transfer function and the continuum autocorrelation function. The lag for a certain emission line is defined to be the location of the peak, or centroid, of the CCF. Its measurement depends not only on the transfer function, but also on the characteristics of the continuum variability, as seen from eq. 1.10. This was demonstrated by Netzer (1991) for the data set of NGC 5548.

Cross-correlation techniques, that were used in astronomy for accurate radial velocity measurements, were first introduced into BLR reverberation experiments by Gaskell and Spark (1986). Actual light curves are sets of numbers that need to be cross-correlated in order to measure the time lag. Eq. 1.8 expressed as a sum of two unnormalized data set is

$$CCF(\tau) \ = \ \frac{1}{N\sigma_C\sigma_L}\sum_t C(t)L(t+\tau) \ , \tag{1.11}$$

where N is the number of points, τ, σ_C and σ_L are the rms of the light-curves, and the two light-curves have zero means. τ is an arbitrary temporal shift between the two data sets. The lag is the value of τ which maximizes the correlation coefficient between the two series. To carry out this calculation, the data points need to be evenly spaced, and for a given $C(t)$, $L(t+\tau)$ needs to be measured. Also, the time base of the light-curves needs to be large and the object needs to vary during this time in order to get meaningful results. Those conditions are usually hard to achieved. Bad weather, and period during which the objects cannot be observed, introduce gaps in the data and the object variations are, of course, unpredictable.

One method to overcome some of those difficulties is the interpolated cross-correlation function (ICCF) method of Gaskell & Sparke (1986) and Gaskell & Peterson (1987) as implemented by White & Peterson (1994; and see also a review by Gaskell 1994). In this method, the CCF is calculated twice for the two observed light curves $C(t_i)$ and $L(t_i)$: once by pairing the observed $C(t_i)$ with the interpolated value $L(t_i-\tau)$, and once by pairing the observed $L(t_i)$ with the interpolated value $C(t_i-\tau)$. The final CCF is taken to be the average of these two CCFs. An optional feature is to extrapolate one light curve at a constant level to avoid discarding data.

A major disadvantage of interpolation methods is the lack of rigorous error estimates of the deduced lag. One way to estimate the error, suggested by Gaskell & Peterson (1987), is an analytic estimate for the uncertainty on the CCF peak position. This i rough estimate relies on specific assumptions, such as uniform sampling of the data. Another way, is to assume a certain model for the BLR and to use Monte Carlo simulations to assess the significance of the lag (Maoz & Netzer 1989). Recently, a new way to estimate the time lag uncertainty was suggested by Peterson et al. (1998b). The method uses Monte Carlo simulations but is model independent. In this method, each Monte Carlo simulation is composed of two parts: the first is a "random subset selection" (RSS) procedure which consists of randomly drawing, with replacement, from a light curve of N points a new sample of N points. After the N points are selected, the redundant selections are removed from the sample such that the temporal order of the remaining points is preserved. This procedure reduces the number of points in each light curve by a factor of $\sim 1/e$ and accounts for the effect that individual data points have on the cross-correlation. The second part is "flux randomization" (FR) in which the observed fluxes are altered by random Gaussian deviations scaled to the uncertainty ascribed to each point. This procedure simulates the effect of measurement uncertainties. Peterson et al. (1998b) demonstrate that under, a wide variety of realistic conditions, the combined FR/RSS procedure yields conservative errors, and real uncertainties may, in fact, be somewhat smaller.

Another drawback of the ICCF method is in dealing with correlated errors between the two light-curves. For example, a correlated error may arise by measuring the continuum flux and the emission-line flux from the same spectrum. Such errors will introduce an artificial correlation at lag zero, hence, corrupting the CCF. The largest uncertainty is due to interpolation since AGN variability is very irregular and no interpolation over a large time gap can solve this problem. Good sampling is the only solution to this problem.

A way that partly avoids those problems is the discrete correlation function (DCF) method (Edelson & Krolik 1988). This method uses only observed data points, thus avoiding interpolation (it uses only pairs of data that are separated by τ). To increase the number of pairs and improve the statistics which contribute to the DCF, one often bins several lags together, i.e., all pairs of points in the interval $\tau - \delta$ to $\tau + \delta$ are binned together as one point. This increases the accuracy of the correlation amplitude but the resolution in time becomes worse. The error estimate of this algorithm has been questioned by several authors (e.g., White & Peterson 1994; Edelson et al. 1996). An improved algorithm was recently suggested by Alexander (1997). This new approach applies Fisher's z transformation to the correlation coefficient, and bins the DCF by equal population bins rather than equal time bins. It results in a more robust and statistically reliable method, the Z-transformed Discrete Correlation Function (ZDCF). The ZDCF peak position and its errors are estimated by a maximum likelihood method that takes into account the uncertainty in the ZDCF points.

1.3.4 Previous BLR Mapping

There have been many monitoring campaigns, since the mid-1980's, all aimed at finding the BLR size and its the transfer function. Most projects concentrated on Seyfert 1s galaxies, at the lower luminosity end of the AGN phenomenon, because they are brighter and tend to vary on shorter time-scales.

Low-Luminosity AGNs

The first UV and optical spectroscopic monitoring campaigns have demonstrated the feasibility of reverberation mapping. They demonstrated that the lines responded to continuum variations, on short time scales of few days to weeks (see Peterson 1988 for a summary of those early programs). Some of those campaign were aimed at the measurement of several emission lines, a goal that was achieved for at least 2-3 Seyfert 1s. The following is a short summary of the more important projects.

[1] The Wise Observatory — Seven months monitoring program (with sampling rate of every few days) of a sample of 14 AGNs resulted in a time lag determination for NGC 4151, Mrk 279, and NGC 5548 (Maoz et al. 1990, 1991; Netzer et al. 1990).

[2] Ohio State University — Program of approximately weekly observations for several years to monitor nine Seyfert 1 galaxies which was carried out at the Lowell Observatory's 1.8-m Perkins Telescope (Peterson et al. 1998a and references therein).

[3] CTIO — Monitoring NGC 3227 (Winge et al. 1995) and IC 4329A (Winge et al. 1996), for five months. Observations every few days.

[4] La Palma — Monitoring program carried out by the "Lovers of Active Galaxies" (LAG) in 1990. Eight AGNs were observed and the program resulted with a lag determination for NGC 3227, NGC 4593, NGC 3516, and Mrk 279 (Robinson 1994).

Probably the greatest success has been achieved by the large consortium known as the "International AGN Watch"[1] (IAW; Alloin et al. 1994). The group has carried out several multi-wavelength monitoring programs that relied on UV spectroscopy by the *International Ultraviolet Explorer (IUE)* and the *Hubble Space Telescope (HST)*, and optical spectroscopy with a large network of ground-based telescopes. The IAW efforts have included two major UV monitoring campaigns on NGC 5548 (Clavel et al. 1991;

[1] http://www.astronomy.ohio-state.edu/~agnwatch/

Korista et al. 1995) complemented by a continuing ground-based campaign (which is lasting for more than 8 years now; Peterson et al. 1999, and references therein), and similar campaigns on NGC 3783 (Reichert et al. 1994; Stirpe et al. 1994), Fairall 9 (Rodríguez-Pascual et al. 1997; Santos-Lleó et al. 1997), 3C 390.3 (O'Brien et al. 1998; Dietrich et al. 1998), and NGC 7469 (Wanders et al. 1997; Collier et al. 1998; Welsh et al. 1998). Other monitoring programs have been built around these projects, including extreme UV monitoring of NGC 5548 with the *Extreme Ultraviolet Explorer (EUVE*; Marshal et al. 1997), a multi-wavelength snapshot of NGC 3783 (Alloin et al. 1995), a long-term X-ray monitoring of 3C 390.3 with *ROSAT* (Leighly et al. 1997), and an X-ray monitoring of NGC 7469 with the *Rossi X-Ray Timing Explorer (RXTE*; Nandra et al. 1998). Most recently a long Infrared campaign with the *Infrared Space Observatory (ISO)* simultaneously with ground-based observations was carried out on Mrk 279 (Santos-Lleó M. et al. 1999). The IAW also undertook an intensive multi-wavelength program on NGC 4151 (Crenshaw et al. 1996; Kaspi et al. 1996a; Warwick et al. 1996; Edelson et al. 1996). However, the limited duration of this experiment (only 10 days with *IUE*) did not provide enough data to fully resolve the UV emission-line response in this object.

All the above studies produced general and important results concerning Seyfert galaxies. So far, about 20 low luminosity AGNs (Seyfert 1 galaxies) have been successfully monitored (see Wandel, Peterson, & Malkan 1999, and references therein). In the following we summarize the main results from these reverberation-mapping projects:

1. Changes in continuum luminosity produce changes in broad emission-line fluxes. The typical time-lag is of order light-days to light-weeks, indicating a BLR size smaller by an order of magnitude than was predicted by early 1980's photoionization models. This finding led to a revision of the old models to fit the new observational results (Peterson 1993).

2. Different emission-lines of the same object have different time lags. This observation led to the conclusion that the BLR is stratified. Also, as the higher ionization lines have shorter time lags, they are thought to be emitted closer to the central source (Peterson 1993).

3. Different monitoring epochs are sometimes resulting with different time-lags. This

was found in several objects (e.g., NGC 4151) and it is most prominent in NGC 5548 where it was found that the time lags from different observing seasons correlate with the seasonal optical luminosity of the object (Peterson et al. 1999). This hints on a possible physical change of the BLR in time.

4. There is growing evidence that BLR motions are predominantly gravitational. There are also indications of Keplerian motion of the BLR gas (e.g., Koratkar & Gaskell 1989, 1991; Crenshaw & Blackwell 1990; Peterson & Wandel 1999)

5. The size—luminosity relation in Seyfert 1s shows a large scatter. However, this relation is found to be consistent with the size scaling as the square root of the luminosity (which is expected under the simplifying assumptions that all AGNs are characterized by the same ionization parameter and BLR density, and have the same shape of the ionizing continuum, independent of luminosity).

6. Non-linearities in line responses to continuum variations (for example in NGC 5548) are consistent with the idea of optically-thin regions in parts of the BLR (e.g., Shields, Ferland & Peterson 1995).

7. The UV and optical continua were found to vary together, with no detectable phase difference, in almost all campaigns. However, recent studies have found time lags between different UV/optical continuum bands which offer a unique way to probe the innermost regions of AGNs, namely the accretion disk (Collier et al. 1998; Peterson et al. 1998b). Moreover, Nandra et al. (1998) found the X-ray and the UV continuum emission in NGC 7469 not to be strongly correlated at zero lag, with some X-ray emission peaking later than the UV emission, by $\sim$4 days. This observation is unexpected and may require a significant change of view about the X-ray production mechanism in AGNs.

High-Luminosity AGNs

While many Seyfert 1 galaxies were studied in this way, very little has been done on the more luminous AGNs — the quasars. Although quasars are more energetic than Seyferts, they are fainter because of their large distances. This make reverberation studies more difficult and demanding.

The long-term *continuum* variability of quasars (years time-scale) has been known for many years. Few examples are:

[1] Usher (1978) compared 820 objects on photometric plates taken 10 years earlier with new observations, and found that the luminosity of about 170 objects have changed. 70% of those objects were found by him to be quasars.

[2] Zamorani et al. (1984) presented results of monitoring the continuum X-ray flux of quasars with the Einstein Observatory and found no variations on time-scales of hours. Few quasars varied on time scales of days, and in time scales of months 9 out of 12 have varied by factors of two or less.

[3] The UV continuum of 81 quasars, observed with the *IUE*, was reviewed by O'Brien, Gondhalekar, and Wilson (1988). They found continuum variations on time scales of weeks and months. Most of the objects varied by one or less magnitude. These authors noted a tendency for the varying amplitude to become smaller for more luminous objects.

[4] Hook et al. (1994) studied $\sim$300 optically selected quasars in the B band in 12 epochs over 16 years. They found high luminosity quasars to show significantly less variability than low luminosity quasars.

[5] Netzer et al. (1996) studied 44 radio-loud quasars for 6 years in the B and R bands. They did not find the amplitude of the variability to depend on the luminosity or the redshift. The rest-frame variability time scale seems to be anticorrelated with the source luminosity but this conclusion might be strongly influenced by observational effects such as sampling period and frequency.

Those studies and others show that the continuum flux in quasars is variable. There are some evidences that the amplitude of the variability is luminosity dependent. Also, the variability of the continuum is wavelength dependent: at longer wavelengths the variability time scale is longer and the relative changes are smaller. Although the continuum behavior of quasars is well studied, the emission-lines variability is not well known. Only a few studies were made, and the correlation between the continuum and the emission-lines variability is not really known.

The most studied quasar is 3C 273, which is very bright. The multi-wavelength review of its properties is given in Courvoisier et al. (1990). There are many observation with *IUE* from 1978 to 1989, which are summarized by O'Brien and Harries (1991), who also reported on a monitoring program with a good time resolution (every two weeks) for about 950 days. Together with all the previous years results they found a time lag of 74 days between the Lyα emission line and the UV continuum. However, Ulrich, Courvoisier, & Wamsteker (1993) argued that the line variations were only marginally significant. Hence, even in this best studied case the results are controversial.

There have been several more attempts to monitor quasars spectrophotometrically, but they all suffer from inadequate temporal sampling or poor flux calibration, which result in insufficient data for determining the BLR size. Zheng & Burbidge (1986), Zheng et al. (1987), and Zheng (1988), reported a monitoring program of about 30 quasars with the Lick Observatory 3 m telescope for a few years, with about one observation a year of each quasar. They found that the emission-line flux changed with response to the continuum changes, but because of the poor time resolution only an upper limit of about 1 light-year for the BLR size was deduced. Gondhalekar et al. (1986), Gondhalekar (1990), O'Brien & Gondhalekar (1991), and Koratkar et al. (1998) reviewed observations done on quasars with IUE. They found that the continuum and line fluxes changed and deduced a BLR size of 0.01–2 light-years. These findings are controversial since the absolute flux calibrations of those observations is very poor. Observations by Sitko (1990), who monitored the quasar GQ Coma with IUE, found a BLR size of 50–100 light-days with the DCF method. However, the data suffer from poor flux calibration and many spectra with low S/N. Pérez, Penston, and Moles (1989), Jackson et al. (1992), Korista (1991), and Erkens et al. (1995) have reported monitoring of quasars. They were all only for a period of about a year, with sampling every few months. The change in the broad lines was checked by comparing their flux to the flux of $[OIII]$ lines which are narrow and not supposed to vary. These authors reported line variations on time scales of a few months, but because of the short monitoring epoch the results are not sufficient for more specific conclusions. Wisotzki et al. (1998) reported a five years spectrophotometric monitoring of the double quasar and gravitational lens HE 1104$-$1805. However, while the quasar has varied considerably the emission line fluxes appear to remain constant.

Thus, prior to the results of the monitoring program which will be presented in this thesis, there were almost no observational results from reverberation mapping of quasars.

1.4 Objectives of This Work

As shown in the previous section, there is a definite need to provide new data on the time dependent line and continuum luminosity of quasars. Some of the difficulties in monitoring high luminosity AGNs, as opposed to low luminosity objects, are related to their brightness. This causes the monitoring program to be very demanding: large telescopes or long integration times are required, the time sampling is a few weeks (the variability time scales are of order of few months) and the monitoring period is several years (the expected BLR size is of order of light-months to light-years). Another difficulty is the absence of strong narrow emission lines that are useful flux calibrators.

The main questions regarding the variability of luminous AGNs are: Do quasar emission lines respond to continuum changes in a way similar to what is observed in Seyfert galaxies? What is the relative amplitude of the line response? What is the line-to-continuum lag? Do quasar BLR sizes scale with luminosity, and how is this related to BLR sizes in Seyfert galaxies? The answers to these questions could provide valuable clues for understanding the nature and evolution of AGNs.

The body of this thesis contains several major chapters, all based on work carried out at the Wise Observatory. Chapter 2 describes the optical monitoring campaign of the Seyfert 1 galaxy NGC 4151, which is one of the best-studied AGNs due to its brightness and variability properties. This is part of an intensive spectroscopic multiwavelength monitoring campaign organized by the IAW, and is a good example of a state-of-the-art Seyfert 1 monitoring.

In chapter 3 we present results from a large scale program to monitor quasars at the Wise and Steward observatories. Our program deals with the difficulties of quasar monitoring in a number of novel ways. We monitor a large and well-defined sample of UV-excess objects covering a range of luminosities. We use a relative flux calibration method that is highly accurate, even during non-photometric weather conditions, without depending on the presence of narrow forbidden lines in the spectrum. The method also allows accurate measurement of the Hα emission line, which is difficult to calibrate (there are no strong forbidden lines in this spectral region), and which is usually redshifted into atmospheric absorption bands in low redshift quasars.

In chapter 4 we translate the observational results into several physical quantities such as size, mass, and luminosity. We analyze our new data, together with data for other AGNs with reliable time-lags determinations. We obtain, for the first time, reliable Size-Mass-Luminosity relations for 34 AGNs spanning 4 orders of magnitudes in continuum luminosity.

In chapter 5 we present a new scheme for modeling the BLR. It involves photoionization calculations applied to a number of variable emission lines at *all times*. We demonstrate how fitting all lines simultaneously provide strong constrains on several of the more important parameters, such as the density, the column density, and the radial distribution of the emission line clouds. When applying the model to the Seyfert 1 galaxy NGC 5548, we are able to reconstruct the light curves of four emission-lines, in time and in absolute flux.

Summary and suggestions for future work are given in chapter 6.

Chapter 2

The NGC 4151 Monitoring Campaign

2.1 Introduction

The Seyfert 1 galaxy NGC 4151 is one of the best-studied AGNs due to its brightness and variability properties. It has been studied at many wavelengths and its characteristics are well known (e.g., Peterson 1988). Several monitoring campaigns have shown variability timescales from a few hours in the hard X-rays (Yaqoob et al. 1993), to a few days in the ultraviolet (e.g., Clavel et al. 1990) and the optical (e.g., Maoz et al. 1991), and several months in the IR (Prestwich, Wright, & Joseph 1992).

NGC 4151 was selected by the AGN Watch consortium as a prime target for an intensive spectroscopic multiwavelength monitoring campaign. The campaign took place for two weeks in 1993 December using the *CGRO*, *ASCA*, *ROSAT*, and *IUE* satellites, and many ground-based telescopes. This chapter describes the observations and results of the ground-based optical campaign. Crenshaw et al. (1996) describes the UV results from *IUE*. The high-energy results (*GRO*, *ASCA*, *ROSAT*) are described by Warwick et al. (1996), and a multiwavelength comparison is given by Edelson et al. (1996).

A primary goal of AGN monitoring has been to determine the size of the broad-line region (BLR). Of the many ground-based variability studies of NGC 4151, the most intensive have been those of Antonucci & Cohen (1983) and Maoz et al. (1991). Antonucci & Cohen monitored NGC 4151 at approximately monthly intervals for over a year. They found that the continuum and broad lines varied on timescales shorter than their temporal resolution, and deduced a BLR radius of less than ~30 lt-days. For these data Gaskell

& Sparke (1986) reported an Hβ lag of $0-7$ days and Hγ lag of $5-9$ days. These observations were also analyzed by Peterson & Cota (1988) who combined them with their own data and arrived at a BLR size of 6$\pm$4 lt-days. The Maoz et al. (1991) monitoring campaign lasted for a period of 8 months with a mean sampling interval of 4 days. Cross correlation, deconvolution, and modeling applied to the data indicated a BLR size of 9$\pm$2 lt-days. The *IUE* monitoring campaign described by Clavel et al. (1990) yielded a characteristic timescale of 4 ± 3 days from the response of the C IV λ1549 and Mg II λ2798 emission lines to the UV continuum.

In this chapter we present results of two months of monitoring of NGC 4151 with a time resolution of about one day. In § 2.2 we describe the ground-based observations together with their reduction and calibration, and present light curves for the continuum and the Hα and Hβ emission lines. In § 2.3 we carry out a time-series analysis of the data and briefly discuss the results. A summary is given in § 2.4. A paper describing these results has been published in *The Astrophysical Journal* (Kaspi et al. 1996a).

2.2 Observations

2.2.1 Data and Reduction

The main effort of the ground-based monitoring campaign was carried out at the Wise Observatory in Israel, using the 1m telescope. The last two hours of each night, for a period of over two months starting on 1993 November 14, were dedicated to the monitoring of NGC 4151. Spectroscopic observations were performed with the Faint Object Spectrographic Camera (Kaspi et al. 1995), using a 10″-wide slit and a 600 line/mm grism, giving a dispersion of 2 Å per pixel. The spectral resolution was determined by the seeing, which was 2 to 3 arcsec, and combined with the instrument spatial scale of 0.9 arcsec/pixel the spectral resolution was $\sim$5 Å. Two different slits were used every night, each located at a different position in the telescope's focal plane. One slit produced spectra in the range $\sim$ 4150$-$6050 Å (hereafter the "B-side") and the other covered the range $\sim$ 5060$-$6990 Å (the "R-side"). With this setup we were able to monitor both the Hα and the Hβ emission lines, while a large part of the AGN continuum between them was observed through both slits. This produced two independent measurements of the 5100$-$6000 Å continuum, since the object was centered in each slit separately.

The spectrograph was rotated to include, together with the nucleus of NGC 4151, a field star ("star 1" of Penston, Penston, & Sandage 1971, P.A. = 156.3°) that served as a local standard. This technique, of using a local comparison star, is described in detail by Maoz et al. (1990) and Maoz et al. (1994), and produces high relative spectrophotometric accuracy.

For each of the B-side and R-side setups, we tried to obtain two or more consecutive exposures per night, with typical integration times of 15 min per exposure. The data were reduced using standard IRAF routines with an extraction window of $\sim$ 13″. The NGC 4151/star ratios of consecutive exposures were compared to test for systematic errors. The ratios almost always reproduced to 0.2%−1.2% at all wavelengths. The few nights where the ratios between exposures differed by more than 3.5% were discarded. (Only three nights were with ratios between 1.2% and 3.5%.) The NGC 4151 and the star spectra from the consecutive exposures were co-added to improve the signal-to-noise ratio, and the resultant NGC 4151 spectrum was divided by an absorption-line-free, interpolated and smoothed version of the co-added stellar spectrum. This removes atmospheric absorption from the Seyfert spectrum and provides the relative flux calibration. This procedure resulted in one spectrum per setup per night. Absolute photometric calibration was achieved by multiplying the NGC 4151/star ratio by a smoothed flux-calibrated spectrum of the comparison star, obtained on photometric nights using known spectrophotometric standards.

The second data set was obtained by the Ohio State University (OSU) group with the Perkins 1.8m telescope at the Lowell Observatory. NGC 4151 was observed for 10 nights between 1993 December 2 and 11, UT, with the Boller & Chivens spectrograph through a 5 arcsec slit at P.A.=90°. Many exposures were taken each night with integration times of $2-3$ min each, with a total integration time of several hours (in order to study the variations on timescales of minutes). The spectra covered the wavelength range $\sim$ 4480−5660 Å. The data were reduced using standard IRAF routines. The individual spectra were co-added to produce three spectra for each night, which, after checking for agreement of 1% or less, were added into one spectrum per night.

The third data set that will be presented here was obtained with the Kast double spectrograph (Miller & Stone 1993) on the Shane 3 m reflector at Lick Observatory, using a 4 arcsec slit which was aligned along the parallactic angle. This set consists of 3 epochs. Seven other data sets were obtained by other AGN watch members covering anywhere between 1 and 8 nights. These will be discussed in the following section.

2.2.2 Calibration

A project of this scope requires the intercalibration of the various data sets into a single consistent set. The method used for this intercalibration is based on the [O III] $\lambda\lambda$4959, 5007 narrow emission lines, by requiring all spectra to have the same flux in these lines. There are various ways of achieving this objective. The one adopted here is based on Peterson et al. (1994).

The Wise data set, being the largest one, was chosen as the reference data set. The [O III] $\lambda\lambda$4959, 5007 emission lines fluxes were measured between the observed wavelengths of 4952−5051 Å, by summing the measured flux above a straight line passing between the average flux in the 6 Å interval on each side of this wavelength range. This kind of measurement was determined by Baribaud & Alloin (1990) to be optimal for the [O III] emission lines.

A second scaling method used is described by van Groningen & Wanders (1992). The method finds the optimum scaling factor, wavelength shift, and convolution factor of one spectrum with respect to a reference spectrum, by slowly varying these parameters until the residuals of one or more non-variable narrow lines in the difference between the two spectra are minimized. This resulted in spectra and light curves which confirmed but did not improve (in terms of the internal scatter within one data set) the results of the former method.

The mean flux of the two [O III] emission lines through the Wise apertures was found to be $\mathcal{F}_{[O\ III]} = 1.575 \times 10^{-11}$ ergs s^{-1} cm^{-2}, with a scatter of 1.1%. (This is consistent with the Antonucci & Cohen (1983) result of $(1.19 \pm 0.06) \times 10^{-11}$ ergs s^{-1} cm^{-2} for the [O III] λ5007 flux.) We consider this to be the accuracy of the comparison-star method. As a test, all B-side spectra were scaled so that their measured $\mathcal{F}_{[O\ III]}$ agree with the above flux. No obvious differences appear in the Wise light curves before and after the [O III] scaling, demonstrating the reliability of the comparison-star method. An attempt to scale all R-side spectra to the same [S II] $\lambda\lambda$6716, 6731 emission line fluxes gave similar results. A comparison of the overlapping continuum bands between the R-side and the B-side spectra shows an agreement of about 1% for almost all epochs.

All other data sets were scaled to match their [O III] line fluxes to the Wise $\mathcal{F}_{[O\ III]}$ by multiplying each spectrum by a factor $\frac{\mathcal{F}_{[O\ III]}}{F([O\ III])_{obs}}$, where $F([O\ III])_{obs}$ is the measured [O III] line flux of the spectrum. Light curves were then measured for the Hβ line and the 5100−5150 Å continuum. These two light curves, which were obtained for each data set, were then intercalibrated with the Wise data set.

The intercalibration method (Peterson et al. 1994) is as follows. First, a point-source correction factor φ was defined by the equation

$$F(H\beta) = \varphi F(H\beta)_{obs}\ , \tag{2.1}$$

where $F(H\beta)_{obs}$ is the Hβ line flux measured for each spectrum after scaling its [O III] line flux to agree with the Wise $\mathcal{F}_{[O\ III]}$, and $F(H\beta)$ is the Wise Hβ flux from an observation that is close in time (see below). The φ factor accounts for the fact that different apertures resulted in different amounts of light loss for the given point-spread function (which describes the surface-brightness distribution of both the broad lines and the AGN continuum source) and the partially extended narrow-line region.

An additive correction was applied to allow for the different amounts of starlight admitted by different apertures. This correction, G, was defined by the equation

$$F_\lambda(5100) = \varphi F_\lambda(5100)_{obs} - G\ , \tag{2.2}$$

where $F_\lambda(5100)_{obs}$ is the continuum measured in the observed wavelength range 5100–5150 Å after the spectrum was scaled to have the Wise [O III] line flux, and $F_\lambda(5100)$ is the contemporaneous Wise result.

A problem unique to this monitoring project is that NGC 4151 could be observed by ground-based telescopes for only about two hours at the end of each night. (Due to *ROSAT* constraints, the campaign on this object, which has a right ascension of ~ 12 hours, was executed in December.) Thus, no pairs of nearly simultaneous observations from different observatories (to determine the values of φ and G) could be found. This limits our ability to intercalibrate the various data sets and is different from previous monitoring campaigns (e.g., NGC 5548) where objects could be observed all night, and the time resolution was a few days.

Given the above difficulty, we have taken the alternative approach of interpolation. The reference Wise light curves of Hβ and $F_\lambda(5100)$ were interpolated linearly, and for every spectrum in the other data sets the values of $F(H\beta)$ and $F_\lambda(5100)$ at their precise date and time were found, and used for defining φ and G (from eqs. 2.1 and 2.2). The φ and G of each data set were then determined by averaging the values that were obtained for each spectrum of a data set. Finally, each spectrum of the given data set was multiplied by the average φ and subtracted by G, producing the final calibrated set.

The intercalibration constants, φ and G, for each data set are given in Table 2.1. The φ for the OSU data set is in good agreement with its value given by Peterson et al. (1995), who calculated it from the [O III] λ5007 surface-brightness distribution of NGC4151 through different apertures.

The intercalibration method can only be used for data sets with more than two epochs. Based on this criterion, several data sets had to be discarded. Also, all data sets with an internal accuracy worse than 3% (i.e., with spectra from the same night differing from each other, or from the Wise set, by more than 3%) were discarded. Given the small variation of the source during the period of intensive monitoring (1993 December 2–11), these data sets do not add useful information and increase the overall noise.

In view of all these limitations, only the two large data sets from Wise and OSU, as well as the smaller Lick data set, will be discussed in the following sections.

Table 2.1. Flux scale factors

Data Set	Point-Source Scale Factor φ	Extended Source Correction G^a
OSU	0.9558 ± 0.0027	-0.758 ± 0.018
Lick	0.9349 ± 0.0043	-1.103 ± 0.023
Wise	1	0

[a]In units of 10^{-14} ergs s^{-1} cm^{-2} Å^{-1}

2.2.3 Line and Continuum Light Curves

Fig. 2.1a and Table 2.2 give mean continuum light curves for four spectral bands: (a) 4560− 4640 Å (hereafter 4600 Å), (b) 5100−5150 Å (average of the Wise B-side and R-side, and several points from the OSU and Lick sets, hereafter 5125 Å), (c) 6170−6230 Å (hereafter 6200 Å), and (d) 6900−6950 Å (hereafter 6925 Å). All wavelengths are in the observed reference frame. All four continuum light curves show the same feature of small "bumps" superposed on a gradual rise of the flux throughout the whole monitoring period. Examination of these light curves shows that the optical continuum changed (from a minimum at JD=2449315.6 to a maximum at JD=2449357.6) by about 35% at 4600 Å and 17% at 6925 Å ($\frac{F_{max}}{F_{min}} - 1$). This can also be seen in Fig. 2.2 (bottom panel): the r.m.s. of the Wise light curves is $\sim$ 10% at 4600 Å whereas at 6925 Å it is $\sim$ 5%.

The Hβ flux was measured from each frame of the Wise B-side, OSU, and Lick sets, between the observed wavelengths 4780−4950 Å, by summing the measured flux above a straight line passing between the average flux in the intervals 4560−4640 Å and 5100−5150 Å. The Hα emission line was measured from the Wise R-side and Lick spectra between 6415− 6710 Å, and its underlying continuum was measured between the average flux of two wavelength ranges 6170−6230 Å and 6890−6970 Å. Fig. 2.1b and Table 2.2 show the Hβ light curve, and Fig. 2.1c and Table 2.2 show the Hα light curve. Both Hα and Hβ show a gradual rise in flux through the monitoring period, which amounts to $\sim$13% in Hα and to $\sim$ 30% in Hβ. While in the Hβ light curve there are several features which resemble the continuum light curve (Fig. 2.1a), such features are barely visible in the Hα light curve.

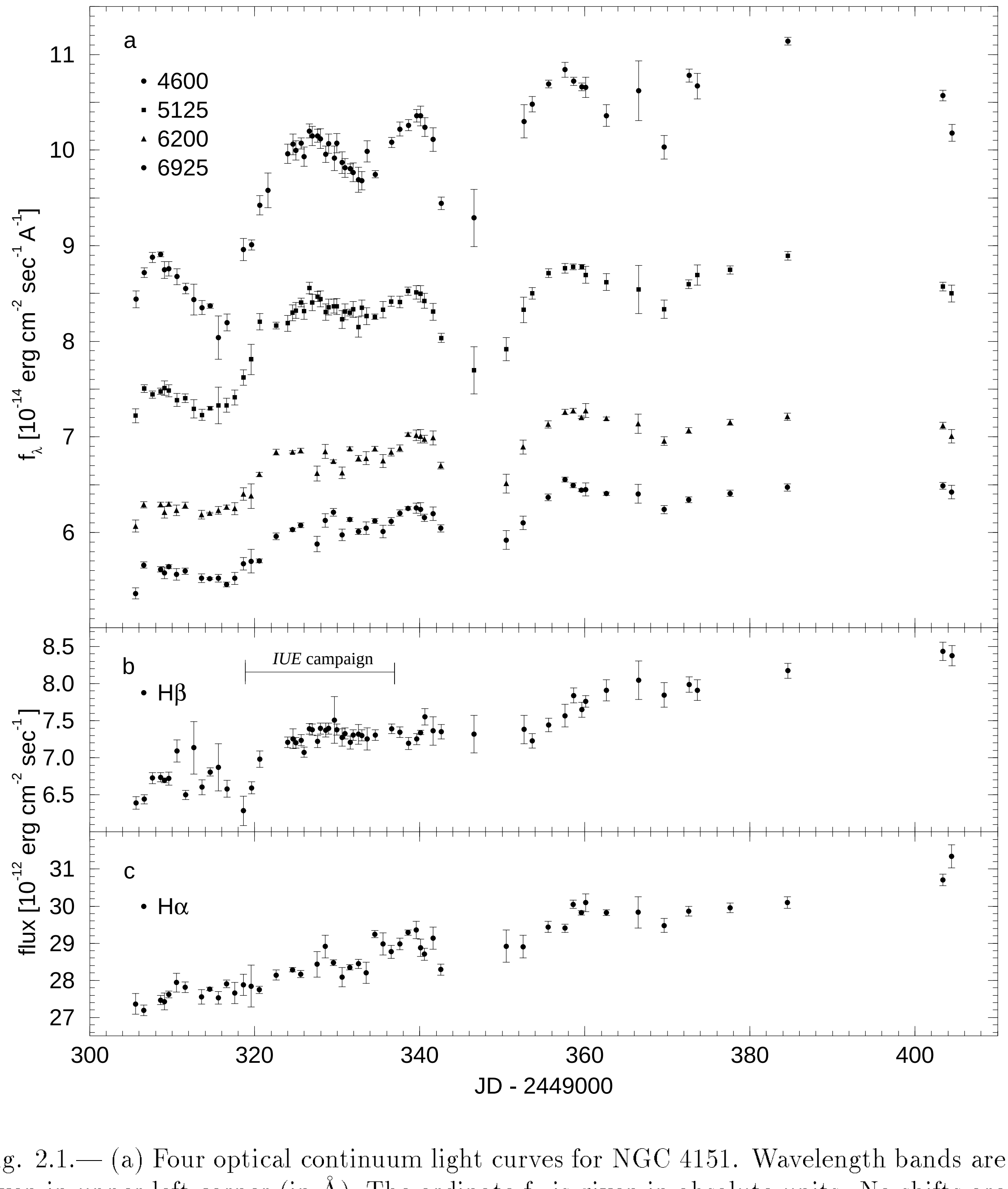

Fig. 2.1.— (a) Four optical continuum light curves for NGC 4151. Wavelength bands are given in upper left corner (in Å). The ordinate f_λ is given in absolute units. No shifts are applied to the top three light curves, and the 6925 Å light curve is shifted by -5×10^{-15} erg cm^{-2} s^{-1} Å^{-1}. (b) Hβ light curve. (c) Hα light curve.

Table 2.2. Light curves

JD	4600 Å	5125 Å	6200 Å	6925 Å	Hα	Hβ
305.6	8.44±0.09	7.22±0.07	6.07±0.06	5.86±0.06	27.36±0.28	6.39±0.09
306.6	8.72±0.05	7.51±0.04	6.29±0.03	6.16±0.03	27.20±0.14	6.44±0.06
307.6	8.88±0.05	7.44±0.04	···	···	···	6.73±0.07
308.6	8.91±0.03	7.48±0.03	6.29±0.03	6.11±0.03	27.47±0.12	6.74±0.06
309.1†	8.75±0.09	7.51±0.08	6.21±0.06	6.08±0.06	27.43±0.22	6.70±0.03
309.6	8.76±0.07	7.48±0.06	6.30±0.02	6.14±0.02	27.62±0.09	6.72±0.09
310.6	8.68±0.08	7.39±0.07	6.23±0.06	6.06±0.06	27.94±0.25	7.09±0.15
311.6	8.55±0.05	7.41±0.05	6.28±0.03	6.10±0.03	27.81±0.15	6.50±0.06
312.6	8.44±0.16	7.29±0.09	···	···	···	7.14±0.35
313.6	8.35±0.07	7.23±0.06	6.18±0.04	6.02±0.04	27.55±0.20	6.60±0.10
314.6	8.37±0.02	7.30±0.02	6.20±0.01	6.02±0.01	27.77±0.05	6.81±0.05
315.6	8.04±0.23	7.33±0.19	6.23±0.04	6.02±0.04	27.53±0.17	6.87±0.32
316.6	8.20±0.09	7.33±0.07	6.26±0.02	5.96±0.02	27.91±0.10	6.58±0.11
317.6	···	7.41±0.08	6.25±0.06	6.02±0.06	27.66±0.29	···
318.6	8.96±0.12	7.62±0.08	6.40±0.07	6.17±0.06	27.88±0.28	6.29±0.20
319.6	9.01±0.05	7.81±0.16	6.38±0.13	6.20±0.12	27.85±0.56	6.60±0.08
320.6	9.42±0.10	8.20±0.09	6.61±0.02	6.20±0.02	27.75±0.10	6.98±0.11
321.6	9.58±0.18	···	···	···	···	···
322.6	···	8.16±0.03	6.84±0.03	6.46±0.03	28.14±0.13	···
324.0*	9.96±0.10	8.19±0.08	···	···	···	7.21±0.07
324.6	10.06±0.11	8.30±0.09	6.84±0.01	6.53±0.02	28.28±0.06	7.26±0.13
325.0*	10.00±0.10	8.32±0.08	···	···	···	7.20±0.07
325.6	10.07±0.06	8.41±0.04	6.86±0.02	6.58±0.03	28.17±0.10	7.24±0.07
326.0*	9.93±0.10	8.31±0.08	···	···	···	7.08±0.07
326.6	10.20±0.07	8.56±0.06	···	···	···	7.39±0.07
326.9*	10.15±0.10	8.41±0.08	···	···	···	7.38±0.07
327.6	10.15±0.07	8.47±0.05	6.62±0.08	6.38±0.08	28.43±0.34	7.22±0.08
327.9*	10.12±0.10	8.44±0.08	···	···	···	7.40±0.07
328.6	9.96±0.08	8.30±0.09	6.85±0.07	6.63±0.07	28.91±0.30	7.37±0.10
328.9*	10.07±0.10	8.36±0.08	···	···	···	7.40±0.07
329.6	9.91±0.13	8.37±0.07	6.75±0.02	6.71±0.04	28.47±0.08	7.51±0.32
329.9*	10.07±0.10	8.36±0.08	···	···	···	7.38±0.07
330.6	9.87±0.11	8.23±0.09	6.62±0.06	6.47±0.06	28.09±0.26	7.27±0.11
331.0*	9.81±0.10	8.31±0.08	···	···	···	7.33±0.07
331.6	9.80±0.05	8.30±0.04	6.88±0.02	6.63±0.02	28.35±0.07	7.21±0.09
331.9*	9.77±0.10	8.33±0.08	···	···	···	7.31±0.07
332.6	9.69±0.13	8.15±0.11	6.77±0.03	6.51±0.03	28.45±0.12	7.32±0.13
333.0*	9.68±0.10	8.35±0.08	···	···	···	7.30±0.07
333.6	9.98±0.11	8.26±0.09	6.78±0.07	6.55±0.07	28.21±0.29	7.25±0.15
334.6	9.75±0.04	8.26±0.03	6.88±0.02	6.62±0.02	29.25±0.10	7.31±0.07
335.5	···	8.33±0.09	6.75±0.07	6.51±0.07	28.99±0.30	···
336.6	10.08±0.05	8.42±0.05	6.84±0.04	6.62±0.04	28.77±0.18	7.39±0.06
337.6	10.22±0.07	8.41±0.06	6.88±0.04	6.70±0.03	28.98±0.15	7.35±0.07

Table 2.2—Continued

JD	4600 Å	5125 Å	6200 Å	6925 Å	Hα	Hβ
338.6	10.26±0.06	8.52±0.04	7.02±0.02	6.75±0.02	29.29±0.07	7.20±0.08
339.6	10.36±0.07	8.51±0.07	7.02±0.06	6.75±0.05	29.36±0.24	7.25±0.07
340.1†	10.36±0.10	8.50±0.08	7.01±0.07	6.74±0.07	28.88±0.24	7.34±0.03
340.6	10.24±0.10	8.42±0.08	6.98±0.04	6.65±0.04	28.70±0.16	7.55±0.11
341.6	10.11±0.12	8.31±0.09	6.99±0.07	6.69±0.07	29.13±0.30	7.36±0.19
342.6	9.44±0.07	8.04±0.05	6.70±0.04	6.54±0.04	28.29±0.15	7.35±0.10
346.6	9.29±0.30	7.70±0.25	···	···	···	7.32±0.25
350.5	···	7.92±0.12	6.51±0.10	6.42±0.10	28.92±0.44	···
352.6	10.30±0.17	8.33±0.13	6.89±0.07	6.60±0.07	28.91±0.30	7.38±0.19
353.6	10.48±0.08	8.50±0.06	···	···	···	7.23±0.10
355.6	10.69±0.04	8.71±0.05	7.13±0.04	6.87±0.04	29.44±0.15	7.44±0.09
357.6	10.84±0.08	8.76±0.05	7.26±0.03	7.05±0.03	29.41±0.11	7.57±0.15
358.6	10.72±0.04	8.78±0.03	7.28±0.03	6.99±0.02	30.05±0.11	7.84±0.10
359.6	10.66±0.04	8.78±0.02	7.20±0.01	6.94±0.02	29.82±0.06	7.65±0.10
360.1†	10.66±0.11	8.70±0.09	7.28±0.07	6.95±0.07	30.09±0.24	7.76±0.08
362.6	10.36±0.11	8.62±0.09	7.19±0.02	6.91±0.02	29.83±0.08	7.91±0.14
366.5	10.62±0.31	8.54±0.25	7.14±0.10	6.90±0.10	29.83±0.42	8.05±0.26
369.6	10.03±0.12	8.34±0.10	6.96±0.04	6.74±0.04	29.48±0.19	7.85±0.17
372.6	10.78±0.07	8.60±0.05	7.07±0.03	6.84±0.03	29.87±0.13	7.99±0.11
373.6	10.67±0.13	8.69±0.10	···	···	···	7.91±0.14
377.6	···	8.75±0.04	7.15±0.03	6.91±0.03	29.96±0.13	···
384.6	11.14±0.04	8.89±0.05	7.21±0.04	6.97±0.04	30.10±0.16	8.17±0.10
403.4	10.57±0.06	8.57±0.04	7.12±0.04	6.99±0.04	30.71±0.16	8.43±0.12
404.4	10.18±0.09	8.50±0.09	7.00±0.07	6.92±0.07	31.34±0.32	8.38±0.14

* OSU data. † Lick data.

[1]Observation Julian Date − 2449000, rounded to a tenth of a day.

[2]Continuum flux in units of 10^{-14} erg cm^{-2} s^{-1} Å^{-1}.

[3]Emission line flux in units of 10^{-12} erg cm^{-2} s^{-1}.

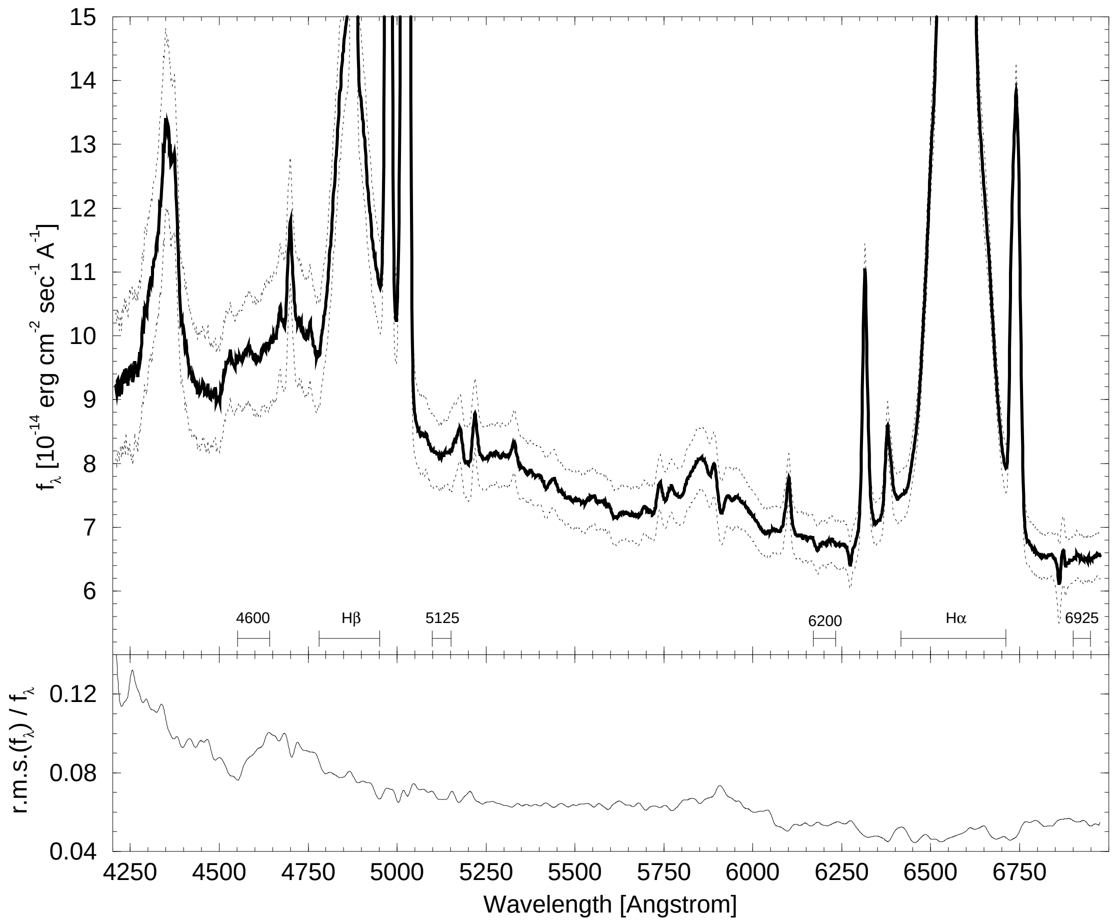

Fig. 2.2.— Top panel: Mean spectrum of NGC 4151 from the Wise data set. The dotted lines are the mean + and − the r.m.s. about the mean. Residual telluric features are visible at 6280 and 6860 Å. The continuum and line measuring bins are marked. Bottom panel: The smoothed ratio of the r.m.s. and the mean spectrum. The variation of the light curves's amplitude and its wavelength dependence can be seen from the larger variance at blue wavelengths.

2.3 Analysis

2.3.1 Cross Correlations

A main purpose of this and other monitoring campaigns is to measure the dimensions of the gas distribution in the BLR of Seyfert galaxies. This is done by cross correlating the line and continuum light curves and determining the time lag between them. Another goal is to study the variability properties of the sources.

We have used two methods to cross correlate the light curves (§ 1.3.2). The first method is the interpolated cross-correlation function (ICCF) of Gaskell & Sparke (1986) and Gaskell & Peterson (1987) as implemented by White & Peterson (1994; and see also a review by Gaskell 1994). In this study of NGC 4151 extrapolation was used to avoid introducing artificial data, and the two last observed points of each light curve were omitted because of the large separation between them and the rest of the light curve. Linear and spline interpolation gave similar results. The uncertainties of the ICCF peak position were calculated using the analytic estimate suggested by Gaskell & Peterson (1987).

The second method is the z-transformed discrete correlation function (ZDCF) of Alexander (1997) which is an improvement of the discrete correlation function (DCF; Edelson & Krolik 1988). The peak position of the ZDCF and its errors are estimated by a maximum likelihood method that takes into account the uncertainty in the ZDCF points. Discrete binning implicitly assumes that the spacing between the data points is uncorrelated with their observing times. The NGC 4151 data treated here pose a special problem in this respect. The galaxy's sky position during this project allowed it to be observed only at the end of the night. As a result, most of the JDs of the Wise set are at 0.6 of a day, whereas most JDs of the OSU set are at 0.0 day (Table 2.2). Since the OSU data only extend over one eighth of the monitoring period, time lags of $n + 0.6$ days (where n is an integer), which cross correlate OSU with Wise points, strongly depend on the behavior of the light curve during the OSU period, whereas time lags of n days, which cross correlate Wise with Wise points and OSU with OSU points, reflect the overall behavior of the light curve. This special sampling pattern resulted in spurious fluctuations between consecutive ZDCF points. Such fluctuations disappeared only when the ZDCF bin size was enlarged, or when the OSU data were omitted from the light curves. Since the first option significantly decreases the number of ZDCF points, we use only the Wise data in the subsequent ZDCF time series analysis. Below we present results from the ZDCF and the ICCF methods (where data points from all sets were used). Both methods yield very similar results.

Table 2.3 shows the properties of the various CCFs calculated for the different continuum spectral bands. In this table, every wavelength band listed in a column is cross correlated with every wavelength band listed in a row, such that if the wavelength band in the row lags behind the wavelength in the column the time lag is positive. For every two bands we calculated the ICCF using the linear interpolation and the ZDCF methods. For each CCF we give the time lag measured from the main peak, the error on the time lag (as described above), the full width at half maximum of the main peak (measured at half way between the peak's maximum and minimum), and the correlation coefficient of the peak. An example of a CCF of two continuum wavelength bands is given in Fig. 2.3. The diagonal in Table 2.3 gives the auto-correlation function (ACF) results for all four continuum wavelength bands. The ACFs are plotted in Fig. 2.4.

Table 2.4 lists the properties of the CCFs of the 5125 Å continuum light curve with the emission line (Hα and Hβ) light curves, as well as the CCF of the emission lines with each other. This continuum band (which was observed in both the B-side and the R-side of the Wise set) was chosen since it is the most reliable one.

The Hα light curve (Fig. 2.1c) shows a small gradual rise of $\sim 12\%$ throughout the entire campaign. No significant signal was found from cross correlating it with itself. In contrast, the Hβ light curve (Fig. 2.1b) shows, on top of the gradual rise of $\sim 30\%$, also some features that follow the continuum variations. The CCFs of Hα and Hβ with the continuum light curve are illustrated in Fig. 2.5.

Table 2.3. Continuum CCFs

	4600 Å lin	4600 Å ZDCF	5125 Å lin	5125 Å ZDCF	6200 Å lin	6200 Å ZDCF	6925 Å lin	6925 Å ZDCF
4600 Å								
Time lag	0.0	0.0						
Time lag error	...	...						
FWHM	11.0	10.0						
Peak correlation ...	1.00	1.00						
5125 Å								
Time lag	0.1	0.0	0.0	0.0				
Time lag error	$^{+0.9}_{-0.9}$	$^{+0.9}_{-0.8}$	...	...				
FWHM	11.5	12.5	13.6	14.4				
Peak correlation ...	0.97	0.96	1.00	1.00				
6200 Å								
Time lag	0.4	0.0	0.4	1.0	0.0	0.0		
Time lag error	$^{+1.0}_{-1.0}$	$^{+0.9}_{-0.6}$	$^{+0.9}_{-0.9}$	$^{+1.0}_{-1.6}$	...	...		
FWHM	11.7	10.5	11.9	11.3	11.4	12.3		
Peak correlation ...	0.96	0.95	0.97	0.97	1.00	1.00		
6925 Å								
Time lag	0.6	0.0	0.5	1.0	0.1	0.0	0.0	0.0
Time lag error	$^{+1.2}_{-1.2}$	$^{+1.4}_{-0.5}$	$^{+1.1}_{-1.1}$	$^{+1.7}_{-1.2}$	$^{+1.2}_{-1.2}$	$^{+0.9}_{-0.6}$	...	...
FWHM	12.9	12.6	12.4	13.1	11.5	11.5	11.0	13.0
Peak correlation ...	0.97	0.95	0.96	0.96	0.98	0.97	1.00	1.00

See explanation in text.

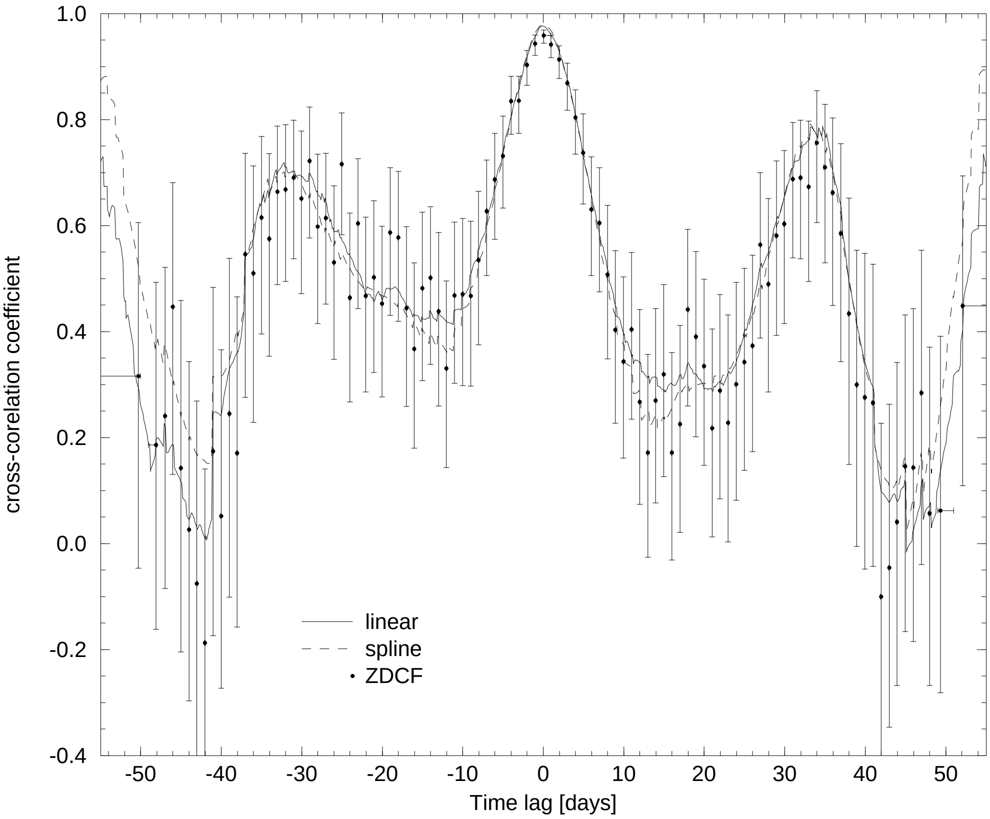

Fig. 2.3.— CCFs of two continuum wavelength bands: 4600 Å and 5125 Å, with linear interpolation (solid line), spline interpolation (dashed line), and ZDCF (error bars with filled circles). Note the good agreement between the three methods.

Table 2.4. Emission line CCFs

	5125 Å lin	5125 Å ZDCF	Hα lin	Hα ZDCF	Hβ lin	Hβ ZDCF
Hα						
Time lag	0.6	1.0	0.0	0.0		
Time lag error	$^{+1.7}_{-1.7}$	$^{+5.0}_{-1.9}$	...	...		
FWHM	11.4	7.4	...	...		
Peak correlation ...	0.87	0.89	1.00	1.00		
Hβ						
Time lag	2.7	1.0	0.6	0.1	0.0	0.0
Time lag error	$^{+1.3}_{-1.3}$	$^{+2.7}_{-1.2}$	$^{+5.2}_{-5.2}$	$^{+3.7}_{-11}$	...	...
FWHM	14.1	16.1	13.5	22.5	10.8	10.4
Peak correlation ...	0.88	0.83	0.90	0.83	1.00	1.00

See explanation in text.

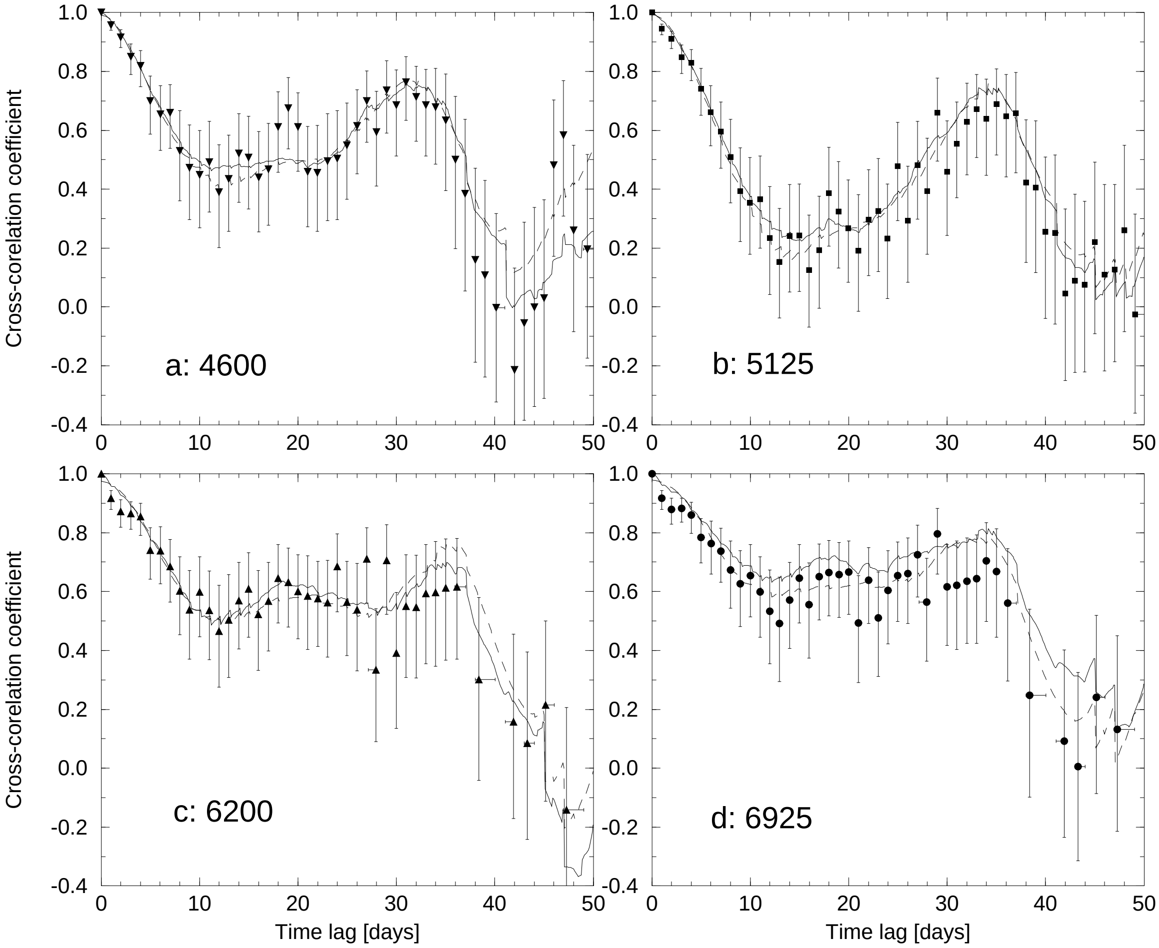

Fig. 2.4.— ACFs of the four continuum bands presented in Table 2.2. Notation is the same as in Fig. 2.3. (a) 4600 Å, (b) 5125 Å, (c) 6200 Å, and (d) 6925 Å.

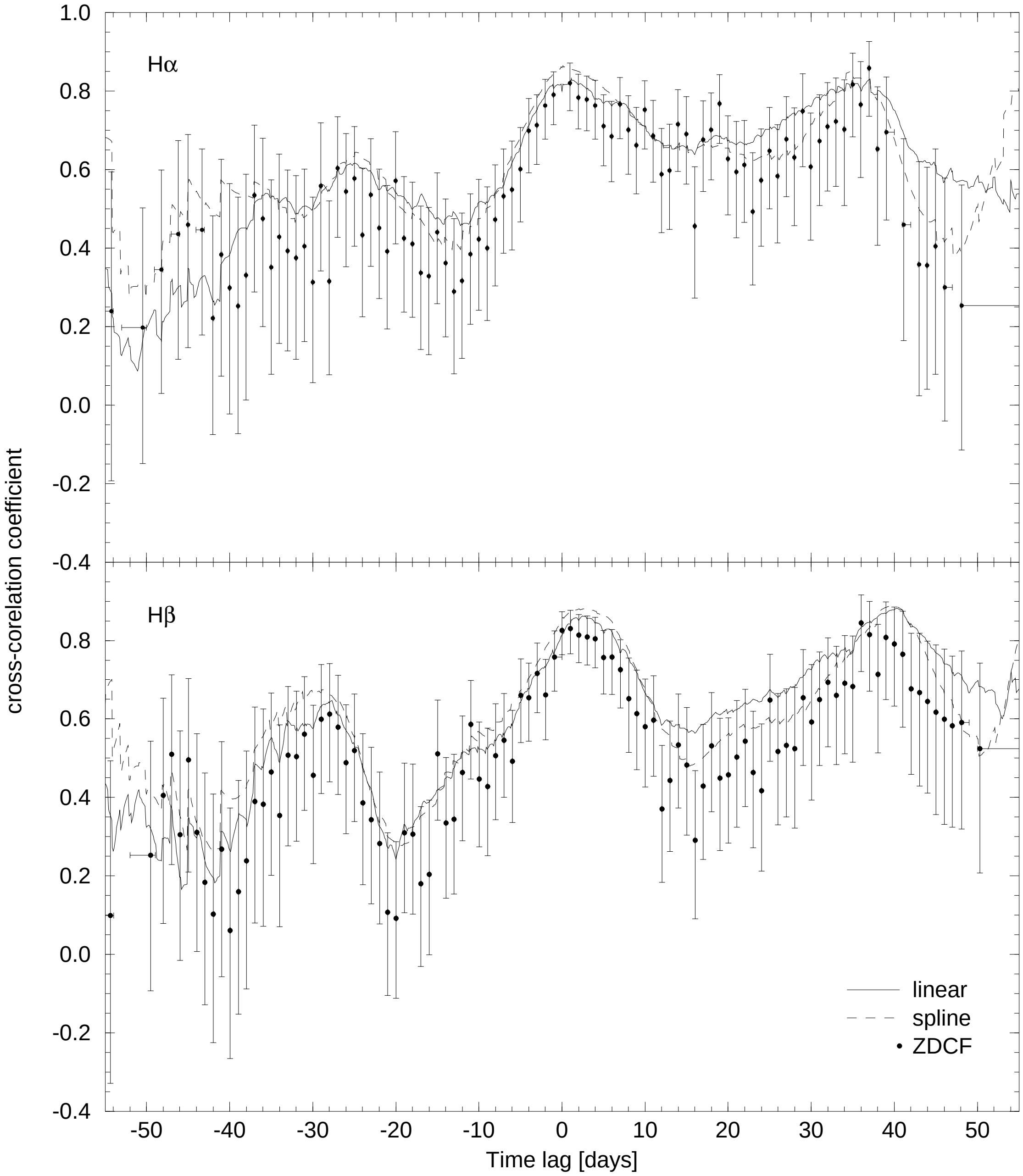

Fig. 2.5.— CCFs of the 5125 Å continuum band with Hα (top panel) and Hβ (bottom panel). Notation is the same as in Fig. 2.3. Note the time lag of $\sim 0 - 3$ days indicated by the main peak.

2.3.2 Continuum Variability

Our monitoring of NGC 4151 for over two months with a temporal resolution of 1 to 4 days resulted in light curves with errors of 1%, and can reveal variations as low as 3%. The variability timescale, defined as the FWHM of the main ACF peak (Table 2.3 and Fig. 2.4), is $\sim$ 13 days. The measured continuum variations are of 17% to 35%, with amplitude decreasing towards longer wavelengths (Fig. 2.1a). This trend extends to shorter wavelengths, as seen by comparing the variability at UV wavelengths (Crenshaw et al. 1996) with the optical light curves presented here (Fig. 2.6). Fig. 2.2, which shows the average and r.m.s. spectrum of NGC 4151 from the Wise data set, illustrates this variable amplitude (see the larger variance at blue wavelengths in the bottom panel). Fig. 2.7 presents this phenomenon in three dimensions: wavelength, JD, and flux. Here we have made use of some more continuum wavelength bands, and the surface was interpolated over missing data points and smoothed.

To quantify the variability amplitude, and its wavelength dependence, we calculated the power spectra of the four continuum light curves. Since the first 38 days of the monitoring period are evenly and almost regularly sampled by the Wise data set, it is reasonable to apply a discrete Fourier transform to these data. The power spectra are presented in Fig. 2.8. The decreasing power of the variability with increasing wavelength is clear. A power-law fit, of the form $PDS \propto f^{\alpha}$, to the first six points gives an index α of -1.5 ± 0.9 for the wavelength bands 4600 Å and 5125 Å, and -0.8 ± 0.6 for the wavelength bands 6200 Å and 6925 Å. The small variation amplitude, especially at the longer wavelengths, prevents us from determining a significant dependence of variation timescale on wavelength.

The dependence of the variability amplitude on wavelength can be explained by the varying relative contribution of starlight from the underlying galaxy. We show this by using template spectra of Sab galaxies from Coleman, Wu, & Weedman (1980) and Kinney et al. (1996). Based on previous observations of NGC 4151 (see Maoz et al. 1991) we estimate the galaxy contribution to the spectrum through the Wise aperture, in the continuum wavelength band of 4600 Å, to be in the range $(2-3.5)\times10^{-14}$ erg cm^{-2} s^{-1} Å^{-1}. These numbers are confirmed by Peterson et al. (1995) who find the starlight contribution through the Wise aperture to be 2.2×10^{-14} erg cm^{-2} s^{-1} Å^{-1}. We normalize the template

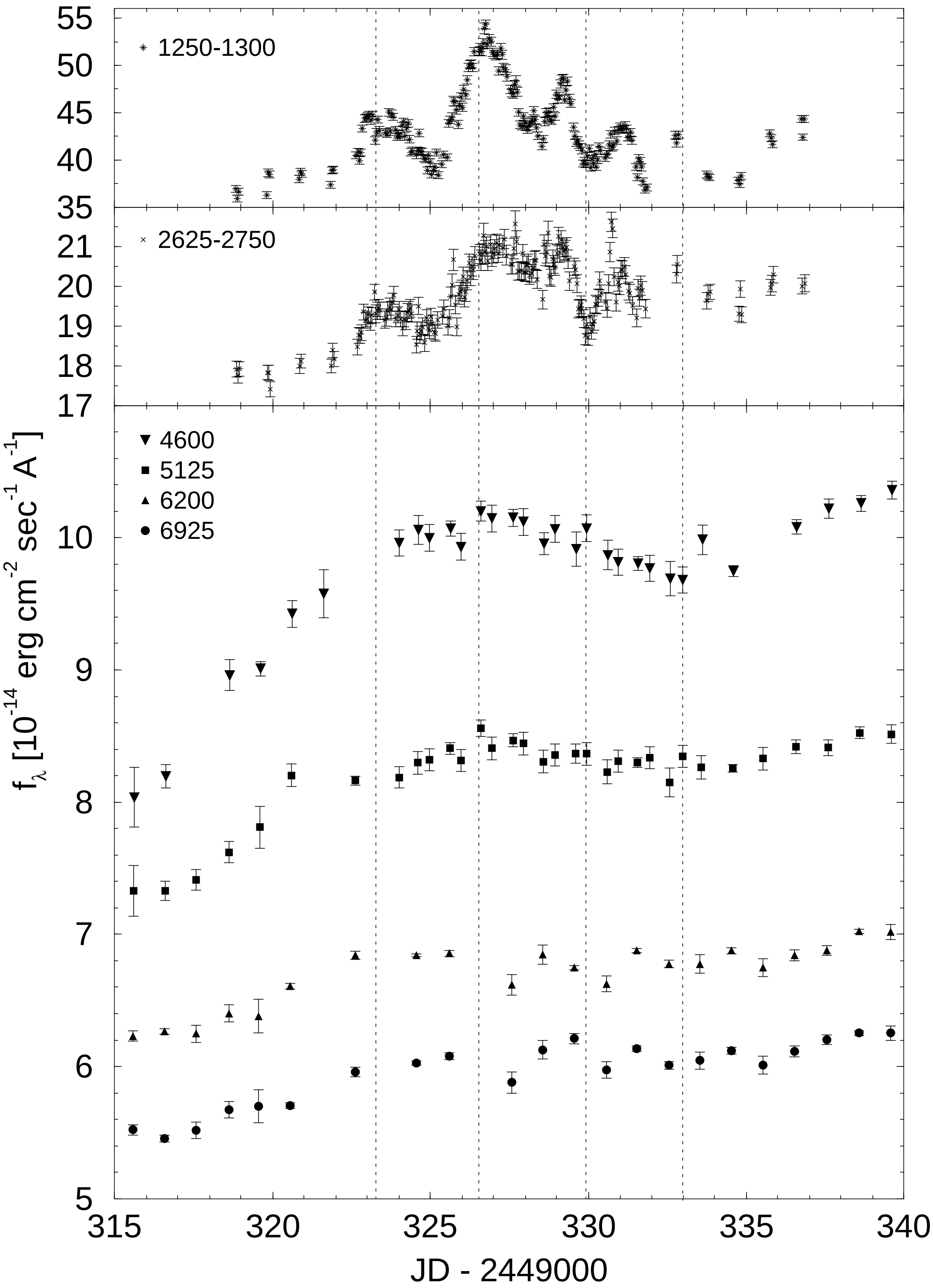

Fig. 2.6.— Same as in Fig. 2.1a for the period of the *IUE* campaign. Two UV continuum light curves are shown for comparison with the optical continuum light curves.

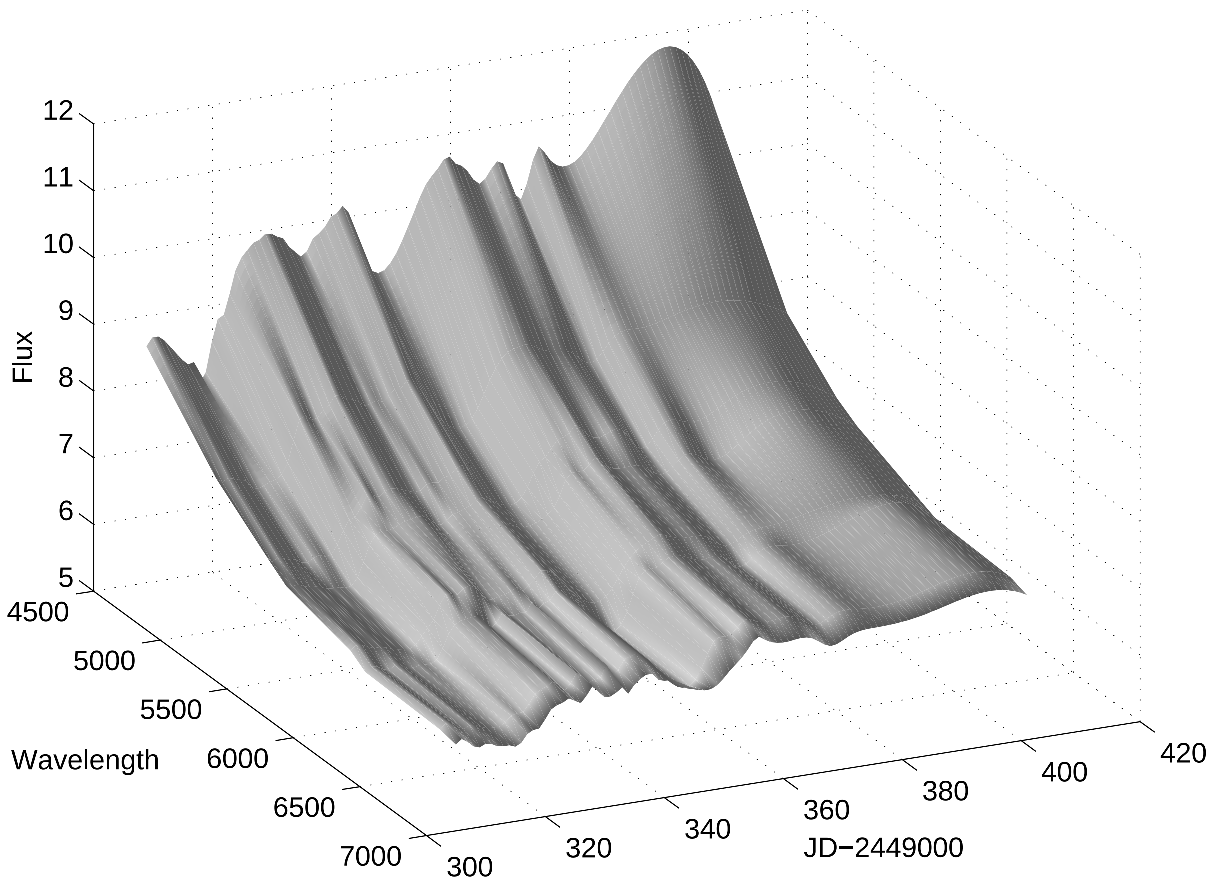

Fig. 2.7.— Continuum variability of NGC 4151. Wavelength in units of Å, flux in units of 10^{-14} erg cm^{-2} s^{-1} Å^{-1}

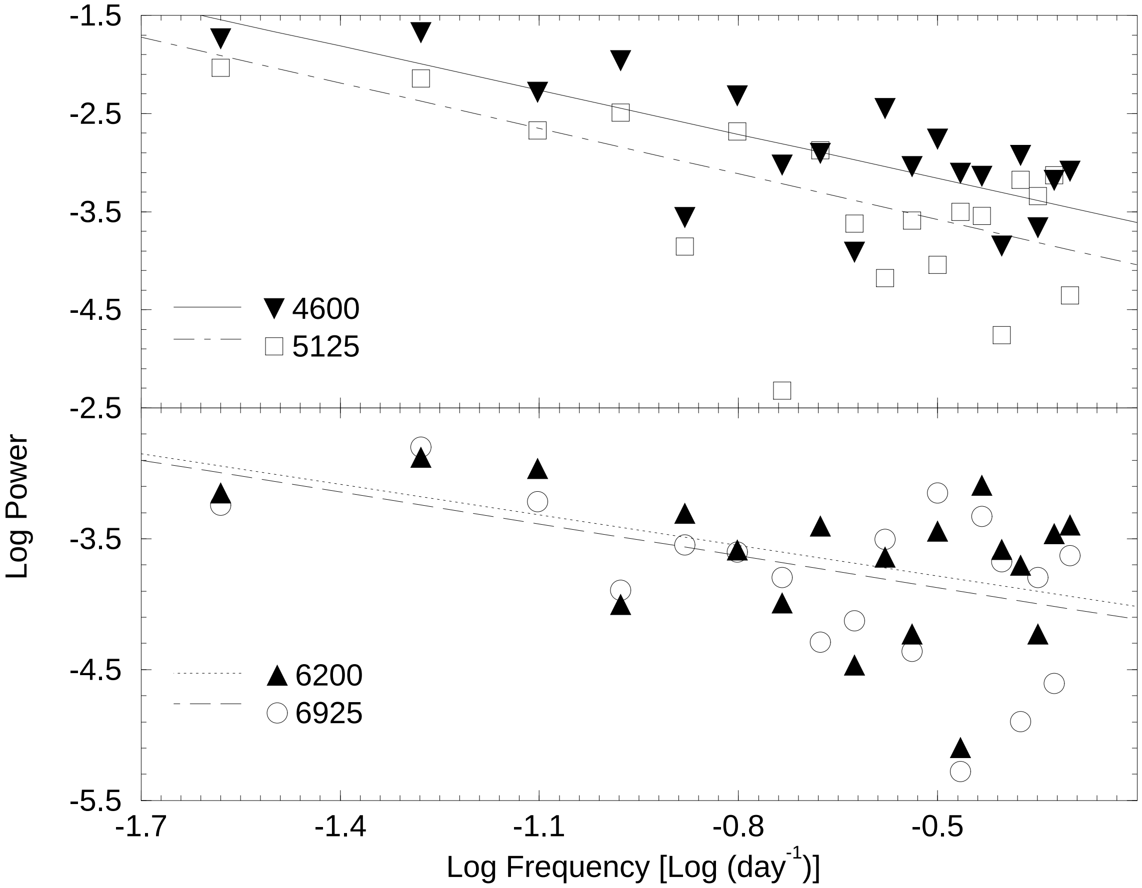

Fig. 2.8.— Power Density Spectra for the four continuum wavelength bands (calculated points and power-law fits). Note the decreasing power in variability with increasing wavelength.

spectra to these numbers and subtract the appropriate values from the four continuum light curves. When using the maximum value for the galaxy contribution at 4600 Å we find that the relative change in each light curve during the 14 days of intensive monitoring is about 20%, i.e., the differences in amplitude between the light curves presented in Fig. 2.6 disappear. The 20% variation amplitude is also similar to that of the UV continuum at 2625−2750 Å (hereafter 2688 Å) but is different from that of the 1250−1300 Å (hereafter 1275 Å) light curve where the relative variation is ∼35%.

We illustrate this result in Fig. 2.9, where we present a simulation of the continuum light curves based on the 2688 Å continuum light curve. From the normalized galaxy template we separated the total flux in this light curve into a galaxy contribution (∼ 2%) and AGN contribution (∼ 98%). The resulting AGN light curve was scaled by a

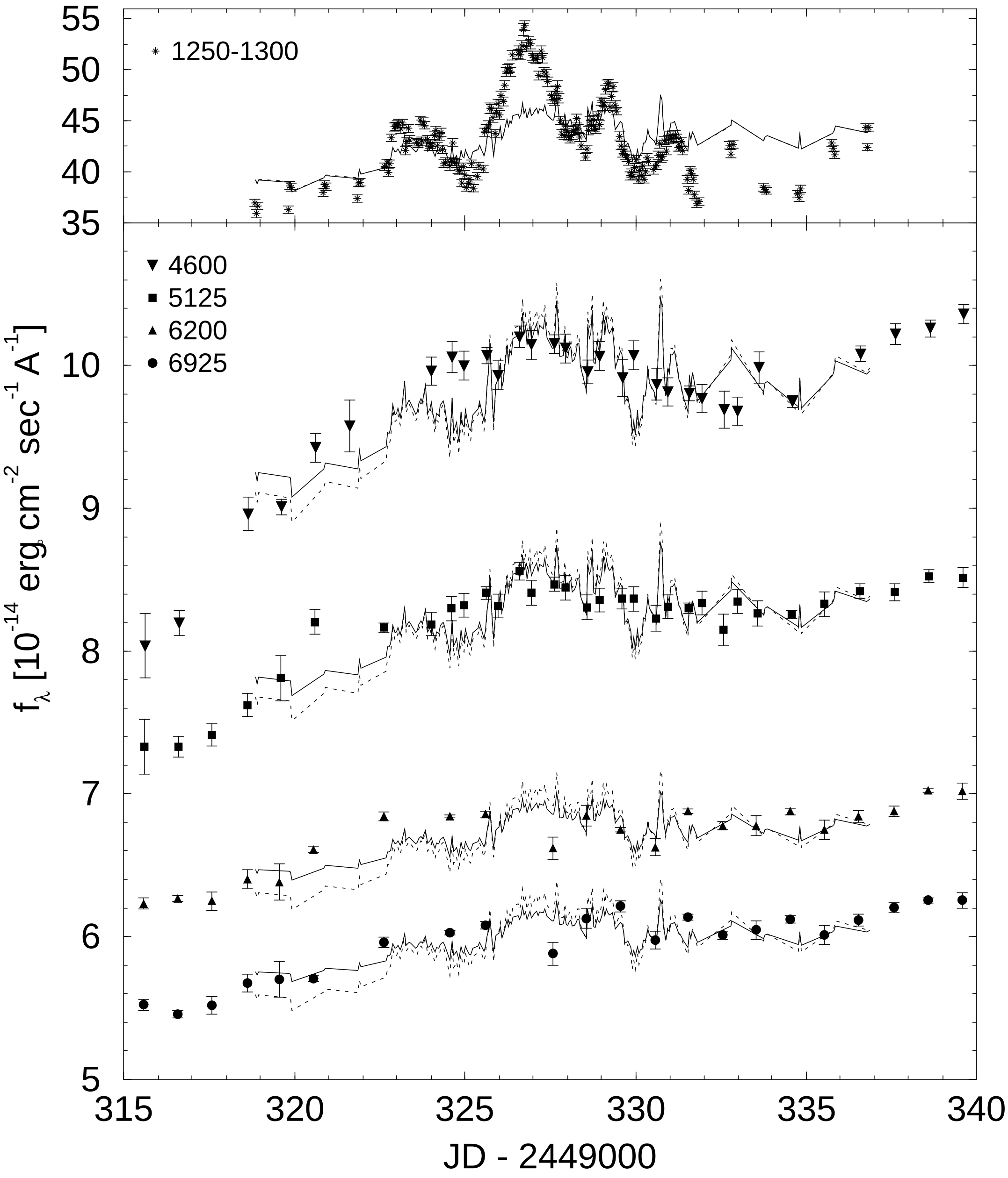

Fig. 2.9.— Light curves from Fig. 2.6 superposed on the linearly-interpolated 2688 Å continuum light curve, after it was scaled and diluted with a constant starlight flux according to the galaxy contribution to the different wavelength bands: solid lines correspond to a galaxy contribution at 4600 Å of 3.5×10^{-14} erg cm^{-2} s^{-1} Å^{-1}, and dotted lines correspond to a contribution of 2×10^{-14} erg cm^{-2} s^{-1} Å^{-1}. Note the agreement between the scaled UV light curve and the optically observed points (bottom panel), indicating that the decrease in variability amplitude at larger wavelengths is mainly the result of dilution by the constant galaxy light. The 1275 Å UV light curve (top panel) is qualitatively different from the scaled 2688 Å light curve.

factor according to its part in the other wavelength ranges and was added to the galaxy contribution at each wavelength range. (The upper limit of the galaxy contribution at 4600 Å, of 3.5×10^{-14} erg cm^{-2} s^{-1} Å^{-1}, gives the solid lines in Fig. 2.9, and the lower limit, of 2×10^{-14} erg cm^{-2} s^{-1} Å^{-1}, gives the dotted lines.) The observed data at all optical wavelengths show good agreement with the galaxy-diluted UV light curve. The wavelength dependence of the variability amplitude in the range 2700–7200 Å can thus be explained by the different starlight contribution at different wavelengths. The 1275 Å UV continuum light curve's amplitude cannot be explained using the starlight contribution alone, as illustrated in the top panel of Fig. 2.9.

From the CCFs of the different continuum wavelength bands with each other, no significant lags are detected, i.e., the continuum varies in phase at all optical wavelengths, to within 1 day. There is no apparent lag between the optical and UV light curves, as discussed in 2.3.3 and in Edelson et al. (1996).

No clear conclusions result from comparison of the optical light curves to the high-energy light curves (Warwick et al. 1996), since the high-energy monitoring period was brief compared to the optical variation timescale, and the number of data points is relatively small.

2.3.3 Emission Line Variability

The Hα light curve (Fig. 2.1c) shows a small gradual rise throughout the entire campaign, and its ACF peak has a width of the duration of the program. No variability timescale can be deduced from this ACF. Cross correlation of Hα with the 5125 Å continuum gives a time lag of $0-2$ days (Fig. 2.5 top panel). The Hβ ACF indicates a variability timescale similar to that of the continuum (Table 2.4). Its CCF with the 5125 Å continuum (Fig. 2.5 bottom panel) suggests a lag, with respect to the continuum light curve, of $0-3$ days. The CCF of the Hα and the Hβ light curves shows no lag, implying that both emission lines varied in phase.

We have performed cross correlations of the UV continuum light curves (presented in Fig. 2.6) with the Hα and Hβ emission-line light curves. No significant time lags were found from these CCFs' peaks. The strong variations in the UV continuum light curves are of order 1–2 days and such rapid variations were not detected in the optical emission-line light curves. This suggests a BLR size larger than 1−2 lt-days, in which light-travel-time effects smear out the rapid variations of the ionizing continuum. Since no large timescale variations (of order 10 days) took place during the UV monitoring period, no time lag between the UV light curves and the optical emission lines could be found.

Detailed analysis and cross correlation of the optical light curves with the UV light curves (Crenshaw et al. 1996), for the *IUE* monitoring period, are shown and discussed Edelson et al. (1996). Here we discuss only the correlation of the UV light curve with the entire optical period that include 14 days of monitoring at the Wise Observatory, prior to the beginning of the *IUE* campaign.

Cross correlation of the entire optical 5125 Å continuum light curve with the UV 1275 Å and 2688 Å continuum and the UV lines C IV λ1549 and He II λ1640 (Crenshaw et al. 1996) are shown in Fig. 2.10. All three CCFs, of 2688 Å, C IV, and He II, show the same feature of a broad maximum, ranging from 0 to 6 days. We believe that this apparent positive delay is an artifact due to the finite duration of the monitoring campaign. This broad feature is probably a result of the optical-continuum behavior prior to the UV monitoring: these three UV light curves show a gradual rise followed by period of constant flux and the optical-continuum light curve shows a gradual rise prior to the beginning of the UV monitoring. Those similar shapes result in high correlation (~ 0.8) over a period of a few days.

We have carried out two tests of this hypothesis. We have extrapolated the UV 2688 Å continuum to the period prior to the *IUE* monitoring based on the shape of the optical continuum. This was done by finding several 5125 Å continuum data points which coincide in time with several 2688 Å continuum data points. The fluxes of those pairs of points were fitted with a linear function which was then used to scale the 5125 Å light curve prior to the *IUE* campaign to the 2688 Å level. This extrapolated UV light curve was cross correlated with the optical continuum and with the C IV line light curves, and gave a CCF peak at zero lag. The second test is cross correlation of the optical and UV light curves using only the part of the optical light curve which overlaps the *IUE* campaign. As shown and discussed in Edelson et al. (1996) § 3.4, the results are narrower peaks CCFs consistent with a zero time lag. Thus, both tests suggest that the time lags between the optical continuum and the UV line and continuum light curves are consistent with zero.

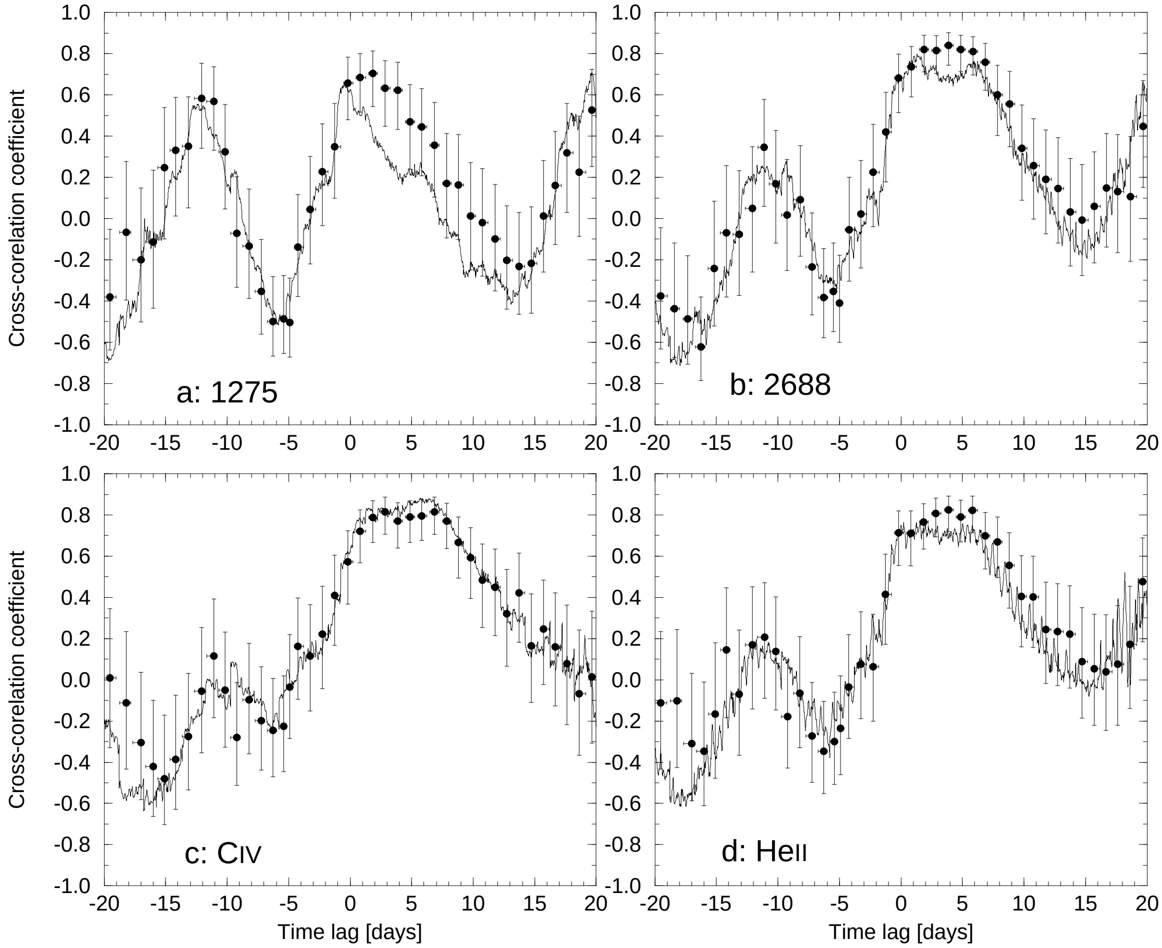

Fig. 2.10.— CCFs of the entire optical continuum 5125 Å band with the (a) 1275 Å UV continuum, (b) 2688 Å UV continuum, (c) C IV λ1549 line, and (d) He II λ1640 line. Notations are the same as in Fig. 2.3. The spline ICCF is not shown.

The last conclusion explains the narrow peak (0-2 days) CCF of the 5125 Å continuum with the 1275 Å continuum shown in Fig. 2.10a. The zero time lag is, indeed the lag and the difference between this CCF and others shown in Fig 2.10 are due to the fact that the 1275 Å continuum has more features in its light curve than the other UV light curves.

2.3.4 Comparison with Past Results

Maoz et al. (1991) monitored NGC 4151 in 1988 for a period of 8 months with an average sampling frequency of once every 4 days. They found continuum variations of $\sim$20%, similar to the 1993 amplitude, with a typical timescale of $\sim$28 days, about twice what is found in the present campaign ($\sim$13 days). They also found that both Hα and Hβ followed the continuum variations and were able to determine time lags of 9 ± 2 days with respect to the optical continuum, for the two emission-line light curves. In this work we find that the Hα and Hβ variations lag behind the optical continuum variations by $0 - 3$ days. In both campaigns the Hβ response to the continuum variations is larger than the Hα response.

To investigate whether these discrepancies in emission-line lags are the result of the different continuum variability timescales or of different analysis methods, we have applied the auto-correlation methods described above to the Maoz et al. (1991) data. We confirm that when using the interpolation methods (linear and spline) the variation timescale is $\sim$28 days. However, using the ZDCF we find a variation timescale of $\sim$15 days. This difference can be explained by the fact that the 1988 monitoring program had several large gaps which, when interpolated, increased the correlation between the continuum and line light curves at larger times. Using the data from the last 96 days of the 1988 campaign, which are more regularly sampled and have only one large gap, we find that both the interpolation and the ZDCF methods yield the same variability timescale of $\sim$15 days. NGC 4151 therefore had similar optical continuum variability behavior in 1988 and in 1993.

We have also performed cross correlation of the emission lines and the continuum of the 1988 data. All cross-correlation methods yield the same results for the time lag, ~ 8 days, consistent with the lag found by Maoz et al. (1991). The lag remains the same when only the last 96 points of the 1988 data are used. We conclude that the differences in Hα and Hβ lags behind the continuum between 1988 and 1993 are not the results of different methods of analysis.

Finally we have checked by way of simulations whether the small lag we measure for the emission lines in 1993 could be the result of the particular form of the continuum variation in 1993, which consisted mainly of a monotonic rise. Assuming a spherical BLR shell of inner radius 2 lt-days and outer radius 30 lt-days (found by Maoz et al. to best fit their results), we calculated the emission-line light curve produced by such a geometry when driven by the spline-interpolated 4600 Å continuum light curve from the present campaign. We then sampled these two light curves at the same epochs of our actual observations, and added to the sampled points a noise similar to the errors in our light curves. We applied to these light curves the various cross-correlation techniques discussed above, and found the CCFs to have broad peaks at lags of ~ 10 days. Thus the above thick shell geometry, with an assumed ionizing continuum similar to the 4600 Å light curve of 1993, gives a lag which is much larger than that which we measure. The small time lags found in the 1993 data are probably not an artifact of the particular continuum behavior we observed.

If the above differences in emission-line lag are real, they may be related to the different state of NGC 4151 which, at the time of the 1993 campaign, was in an "active" state, in contrast to its lower flux level during the Maoz et al. monitoring campaign of 1988. (The optical continuum and line fluxes in the present monitoring campaign are about a factor of two higher than in 1988; see also Oknyanskij, Lyutyi, & Chuvaev 1994.) Evidence for a changing lag has been shown by Peterson et al. (1994) in the one other Seyfert galaxy that has been intensively monitored for several years, NGC 5548. A possible physical explanation for the change in the lag is a real change in the BLR gas distribution between 1988 and 1993. Such a change is, in principle, possible considering the scales and velocities present in the nucleus of NGC 4151 which yield a dynamical time scale of ~ 3 years (see also Wanders 1994). An alternative explanation is that during the present campaign, the optical continuum did not properly represent the behavior of the ionizing continuum. In particular, if the variability timescale of the *ionizing* continuum driving the lines is different between the two campaigns, the resulting time lags for the same BLR geometry can be very different (Netzer & Maoz 1990; Netzer 1990). Some evidence for this is seen in the differently-shaped light curves of the 1275 Å and the 2688 Å continua (Fig. 2.9). Edelson et al. (1996) show that the normalized variability amplitude, which measure the fractional (as opposed to absolute) variations, is 24% in the X-ray, 9% in the 1275 Å band, 4% in the 2688 Å band and only 1% in the 5100 Å band. According to the models presented in Edelson et al. (1996) this indicates that at most 4% of the emission at 5100 Å could be due to reprocessing with the rest coming from a component with different (slower) variability. Hence, the optical light curve might be poorly representing the ionizing continuum.

2.4 Summary

In this chapter we have presented optical-band results of an intensive two-month spectrophotometric monitoring campaign of the Seyfert galaxy NGC 4151, with a typical temporal resolution of one day. The main results of this campaign are as follows:

1. The continuum variations are between 17% and 35%, with decreasing amplitude towards longer wavelengths. The broad Hα line flux varied by $\sim$ 12% and the broad Hβ flux by $\sim$ 30%.

2. The decreasing continuum variability found at longer wavelengths can be explained by the varying contribution of starlight from the underlying galaxy. The exception to this is the far-UV 1275 Å continuum where the variations must be intrinsically larger.

3. The various optical continuum bands vary in phase, with a lag of < 1 day. The typical continuum variability timescale is $\sim$ 13 days and is similar at all optical wavelength bands. The variability amplitude and timescale are similar to those observed in the past in this object.

4. No evidence for a time lag between the optical continuum and the UV continuum and emission lines was found. This may be partially the result of the short duration of the *IUE* campaign. Edelson et al. (1996) give details on interband phase lags derived from the CCFs.

5. The Hα and Hβ light curves follow roughly the continuum variations and lag them by $0 - 3$ days, in contrast to past results where a time lag of 9$\pm$2 days was found. This may be related to a different variability timescale of the *ionizing* continuum, or to a real change in the BLR gas distribution in the 5.5 years interval between the two campaigns.

Chapter 3

The Palomar-Green Quasars Monitoring Campaign

3.1 Introduction

In order to obtain definite results on the BLR size in quasars, in 1991 March we began monitoring a well-defined sub-sample of 28 quasars from the Palomar-Green (PG) sample (Schmidt & Green 1983) at the Wise and Steward Observatories. Results from the first 1.5 years were presented in Maoz et al. (1994) where it was shown that most quasars underwent continuum variations with amplitudes of 10% – 70%. Balmer-line variability, correlated with the continuum variations, was detected in several objects. The preliminary data showed that the typical response time of the emission lines is $\lesssim 6$ months. Reverberation mapping of such objects therefore requires several years, with sampling intervals of less than a few months. Further results, based on four years of monitoring two quasars from our sample, PG 0804+761 and PG 0953+414, were presented in Kaspi et al. (1996). The measured time lags between the Balmer lines and the continuum variations of the quasars suggested that the BLR size grows roughly as the square root of the nucleus luminosity. Wandel et al. (1999) confirmed this result for a somewhat larger sample of AGNs.

During the period of our spectrophotometric project we also monitored several quasar samples photometrically in the B and R bands. The broad-band results for radio- and optically-selected samples were presented in Netzer et al. (1996) and Giveon et al. (1999), respectively. The optical sample in Giveon et al. (1999) consists of 42 PG quasars, including all 28 objects discussed in the present study.

The present chapter presents final results from 7.5 years of spectroscopic monitoring of our sample. In § 3.2 we describe the sample, observations, data reduction, and present the light curves and in § 3.3 we perform a time a series analysis to determine the response time of the emission-line flux to continuum variations. A paper describing these results has been submitted to *The Astrophysical Journal.*

3.2 The Sample

The Palomar-Green (PG) sample of quasars (Schmidt and Green 1983) is well-suited for quasar emission-line monitoring. The brightness of the PG quasars ($B < 16$) enables spectra to be obtained for about 4–10 quasars a night on a small to medium-sized telescope. The low redshift of most of the PG quasars keeps the Balmer series in the optical range, and cosmological time dilation does not significantly lengthen the various timescales. The PG quasars form a complete $U - B$ color-selected sample whose spectral properties have been well studied (Neugebauer et al. 1987; Kellermann et al. 1989; Berriman et al. 1990; Boroson and Green 1992). Variability characteristics can therefore be tested for correlations with the other properties of the quasars. Another advantage is that the continuum variability properties of the PG sample have been studied (Keel and Allan 1991), allowing an estimate of the number of quasars that needed to be monitored in order to detect moderate variations in some of the objects. Keel and Allan found from broad-band monitoring of most of the PG quasars over a period of 3.5 years that 30% of them varied by 0.2 to 1 mag in the B and V bands. We therefore expected that by monitoring about 30 quasars for 1-2 years we would detect continuum variations potentially large enough to drive emission-line variations in 5-10 objects. This expectation has been borne out by our results, as published in Maoz et al (1994) and as described below.

To cull the PG quasar sample to about 30 objects, we made cuts in declination, redshift, apparent magnitude, and absolute magnitude. We included only quasars with northern declination so as to be able to monitor them for longer intervals from northern hemisphere telescopes. We accepted only quasars with redshifts less than 0.4, keeping the $H\beta$ line within our observable spectral range ($4000 - 8000$Å). Based on the original B magnitudes of Schmidt and Green (1983), we required $B < 16$, to provide adequate S/N in brief exposures, and $M_B < -23$, which is a commonly-used defining border between

Seyfert galaxies and quasars. One quasar (PG 1151+117) was dropped from the sample when the first observations in 1991 May showed that it was considerably fainter than expected. A final criterion was the presence of a suitably bright field star within 3.5 arcminutes of the quasar, which served as a comparison star for the quasar (see below). Our sample consists of 28 quasars satisfying these criteria, listed in Table 3.1. Throughout this work we will use only the first four numbers in the PG object name to identify individual objects.

3.3 Observations, and Reduction

The observations were carried out using the Steward Observatory (SO) 2.3m telescope and the Wise Observatory (WO) 1m telescope. Throughout the years different detectors were used. At SO we used the Boller & Chivens spectrograph with a 300 l/mm grating, a $4.5''$-wide slit and a TI CCD. In 1992, September, the CCD was replaced with a 1200×800 Loral CCD. At the WO the Faint Object Spectroscopic Camera (FOSC; Kaspi et al. 1995) was used with a $15''$-wide slit and a front-illuminated 1024×1024 TI CCD as a detector. In 1994 February the slit was replaced by a $10''$-wide slit and the detector was replaced by a 1024×1024 back-illuminated Tektronix CCD. The typical wavelength coverage was $\sim$4000–8000 Å, with a dispersion of $\sim$3.8 Å, and a spectral resolution of $\sim$10 Å.

For every quasar, the spectrograph was rotated to the appropriate position angle to simultaneously include a nearby (<4 arcminute) field star within the slit, which served as a standard. This technique was shown by Maoz et al. (1989) to yield a 1σ photometric error of 3% when used for Seyfert galaxies on the Wise 1m telescope. The high photometric accuracy obtainable with this technique is especially important in quasar monitoring since, as shown by Keel and Allan (1991) and confirmed by our results below, typical quasar variation amplitudes can be only a few tenths of a magnitude. As we shall see, the emission line variations are even smaller. Apart from the high photometric accuracy that is obtained, this calibration method has several important advantages over other methods used in AGN monitoring. Spectrophotometric data can be obtained even during relatively poor weather, thus decreasing the likelihood of gaps in the sampling. The narrow forbidden lines which are often used for flux calibration in Seyfert monitoring programs are frequently weak, absent, or blended in quasars, and could therefore not be used. The

Table 3.1. Sample Properties

Object (1)	RA (1950.0) (2)	Dec (3)	z (4)	m_B (5)	M_B (6)	A_B (7)	N_{phot} (8)	N_{spec} (9)	f_λ(5100Å) (10)	R_{comp} (11)	PA$_{comp}$ (12)
PG 0026+129	00 26 38.1	+12 59 30	0.142	15.3	-23.7	0.13	38	56	26.9 ± 4.0	95	42.0
PG 0052+251	00 52 11.1	+25 09 24	0.155	14.7	-24.1	0.12	41	56	20.7 ± 3.7	92	153.4
PG 0804+761	08 04 35.4	+76 11 32	0.100	14.5	-23.7	0.11	38	70	54.8 ± 10.0	182[a]	315.6[a]
PG 0844+349	08 44 33.9	+34 56 09	0.064	15.1	-22.1	0.08	31	49	37.1 ± 3.8	124	36.8
PG 0953+414	09 53 48.3	+41 29 58	0.239	15.4	-24.5	0.00	38	36	15.6 ± 2.1	104	31.7
PG 1048+342	10 48 56.1	+34 15 23	0.167	17.7	-21.9	0.00	30	1	5.51 ± 0.28	186	94.7
PG 1100+772	11 00 27.4	+77 15 09	0.313	15.9	-24.7	0.06	46	9	7.72 ± 0.23	68	84.1
PG 1202+281	12 02 08.9	+28 10 54	0.165	16.2	-23.0	0.03	37	9	7.2 ± 2.0	73	219.8
PG 1211+143	12 11 44.8	+14 19 53	0.085	14.4	-23.4	0.13	52	38	56.6 ± 9.2	162	352.2
PG 1226+023	12 26 33.4	+02 19 42	0.158	12.8	-26.3	0.00	26	39	213 ± 26	171	171.2
PG 1229+204	12 29 33.1	+20 26 03	0.064	15.5	-21.7	0.00	32	33	21.5 ± 2.3	75	291.5
PG 1307+085	13 07 16.2	+08 35 47	0.155	15.6	-23.5	0.02	35	23	17.9 ± 1.8	138	186.5
PG 1309+355	13 09 58.5	+35 31 15	0.184	15.5	-24.0	0.00	30	9	23.6 ± 1.4	167	74.2
PG 1322+659	13 22 08.5	+65 57 25	0.168	16.0	-23.3	0.05	27	8	11.60 ± 0.74	104	277.5
PG 1351+640	13 51 46.3	+64 00 28	0.087	14.7	-23.2	0.03	40	30	51.4 ± 5.1	109	196.5
PG 1354+213	13 54 11.5	+21 18 30	0.300	17.3	-23.2	0.04	25	3	11.14 ± 0.25	125	133.4
PG 1402+261	14 02 59.2	+26 09 51	0.164	15.6	-23.6	0.00	27	6	18.73 ± 0.87	171	334.8
PG 1404+226	14 04 02.5	+22 38 03	0.098	16.5	-21.8	0.01	27	8	11.40 ± 0.91	77	223.0
PG 1411+442	14 11 50.1	+44 14 12	0.089	15.0	-22.9	0.00	34	24	37.1 ± 3.2	128	347.0
PG 1415+451	14 15 04.3	+45 09 57	0.114	16.3	-22.3	0.00	29	3	15.2 ± 1.8	189	95.2
PG 1426+015	14 26 33.8	+01 30 27	0.086	15.7	-22.2	0.12	33	20	46.2 ± 7.1	106	341.4
PG 1444+407	14 44 50.2	+40 47 37	0.267	17.4	-23.0	0.00	27	5	9.98 ± 0.39	158	155.4
PG 1512+370	15 12 46.9	+37 01 56	0.371	16.4	-24.5	0.05	35	10	4.82 ± 0.76	63	284.9
PG 1613+658	16 13 36.3	+65 50 38	0.129	14.9	-23.8	0.04	42	48	34.9 ± 4.3	101	164.2
PG 1617+175	16 17 56.2	+17 31 34	0.114	15.5	-22.8	0.15	39	35	14.4 ± 2.5	147	253.0
PG 1700+518	17 00 13.4	+51 53 37	0.292	15.4	-25.2	0.02	41	39	22.0 ± 1.5	104	183.5
PG 1704+608	17 04 03.5	+60 48 31	0.371	15.6	-25.5	0.00	39	25	16.6 ± 2.4	114	188.2
PG 2130+099	21 30 01.2	+09 55 01	0.061	14.7	-22.4	0.17	47	64	48.4 ± 4.5	86	68.2

Notes—
(1) Object name, as it appears in Schmidt & Green (1983).
(2)–(3) Right Ascension and Declination (1950).
(4) Redshift.
(5)–(6) Median (over all epochs) apparent and absolute B magnitudes from Giveon et al. (1999).
(7) Galactic B-band extinction, A_B, from NED (The NASA/IPAC Extragalactic Database is operated by the Jet Propulsion Laboratory, California Institute of Technology, under contract with the National Aeronautics and Space Administration). See § 4.3.
(8)–(9) Number of photometric and spectrophotometric observing epochs.
(10) Average flux and its rms at rest wavelength ∼5100 Å in units of 10^{-16} erg s^{-1} cm^{-2} Å^{-1}(see Table 3.2 column (7) for exact wavelength intervals) .
(11)–(12) The angular separation and position angle of the comparison star (see § 3.3), in arcseconds and degrees, respectively.

[a] Comparison star at SO: $R_{comp} = 119$, PA$_{comp} = 64.3$.

$H\alpha$ line (usually the second strongest emission line in AGNs, after Lyα) is, except for the lowest redshift Seyferts, always redshifted into the complex atmospheric absorption bands beginning at 6900Å. The simultaneously obtained spectrum of the comparison star under exactly the same conditions allows a near-perfect correction of this absorption and hence an accurate measurement of the $H\alpha$ line.

Two consecutive exposures of every accessible quasar/star pair were usually obtained in every run. Exposure times were typically 15 min per exposure at Steward and 1hr at Wise. The spectroscopic data were reduced using standard IRAF[1] routines. Lamp flats taken adjacent to every exposure were used to correct for pixel-to-pixel variations in sensitivity (and also sharp wavelength-dependent sensitivity changes in the Wise FOSC). Dome or twilight flats were used to correct the images for changes in the illumination along the slit (important mainly in the Steward spectra). The spectra of each quasar and its comparison star were extracted in a standard way and were wavelength-calibrated by using He-Ar arc spectra extracted from arc exposures taken adjacent to every object exposure.

The quasar/star flux ratios between consecutive exposures were compared to test for any systematic errors in the observation (e.g. slit angle errors, guiding or positioning errors, loss of light due to differential atmospheric refraction). The ratios almost always reproduced to 0.5-2.5% at all wavelengths. The few epochs where the ratios between exposures differed by more than 5% were discarded. We also verified, by means of the differential photometry of each field (Giveon et al. 1999), that none of our comparison stars are variable, to within ~2%. The quasar and star spectra from the consecutive exposures were co-added to improve S/N, and the resultant quasar spectrum divided by an absorption-line-interpolated and smoothed version of the co-added star spectrum. (The spectral region of the star with atmospheric absorption bands was *not* smoothed, in order for the division to properly remove these absorptions from the quasar spectrum.) The wide slits used to ensure accurate photometry caused some degradation of the wavelength calibration. Small shifts in wavelength were made in the quasar/star ratios to bring all epochs of a quasar to a common wavelength scale, judging by the prominent emission

[1]IRAF (Image Reduction and Analysis Facility) is distributed by the National Optical Astronomy Observatories, which are operated by AURA, Inc., under cooperative agreement with the National Science Foundation.

features (usually the [OIII]λ5007 line and the $H\alpha$ peak). The quasar/star ratios for all epochs were multiplied by a smoothed flux-calibrated spectrum of the comparison star, to obtain calibrated spectra of each quasar for all epochs. The calibrated spectra of the comparison stars were determined from measurements of spectrophotometric standards on nights that were photometric. The absolute calibration of a set of spectra for a given quasar is therefore accurate to $5-15\%$, depending on the number of spectrophotometric calibrations that were obtained for the comparison. The differential spectrophotometric accuracy relative to the comparison star, which is our main concern in this program, is much better. From comparison of the different-epoch spectra of the least variable quasars, we estimate the relative flux calibration error to be $\sim 2\%$. We also find excellent agreement between spectra taken at WO and at SO when the observations are of non-variable objects or are close in time. An independent check of the continuum variations of the quasars measured from the spectrophotometry, and of the the assumption that the comparison stars do not vary, comes from contemporaneous CCD photometry of the sample (see below).

For each quasar we used all the spectra to produce an average spectrum and a root-mean-square (rms) spectrum, defined as:

$$\sigma(\lambda) = \left\{ \frac{1}{(N-1)} \sum_{i=1}^{N} \left[f_i(\lambda) - \bar{f}(\lambda) \right]^2 \right\}^{1/2}, \tag{3.1}$$

where the sum is taken over the N spectra, and $\bar{f}(\lambda)$ is the average spectrum (Peterson et al. 1998a). Examples of a typical mean and rms spectra are shown in Fig. 3.1 for PG 0844. We used the average and rms spectra to choose line-free spectral bands suitable for setting the continuum underlying the emission lines, and the wavelength limits for integrating the line fluxes. The spectral regions for the Balmer lines and the continuum bands on both sides of each line are given in Table 3.2. The line and continuum fluxes were measured automatically for all epochs by calculating the mean flux in the continuum bands and summing the flux above a straight line in f_λ that connects continuum bands straddling the emission line. This process measures the total emission in each line, i.e., the flux of the broad component of the line together with its narrow component. The error in the line flux was calculated by propagating the error in the setting of the continuum levels, determined from the standard deviation of the mean in the continuum bands. To

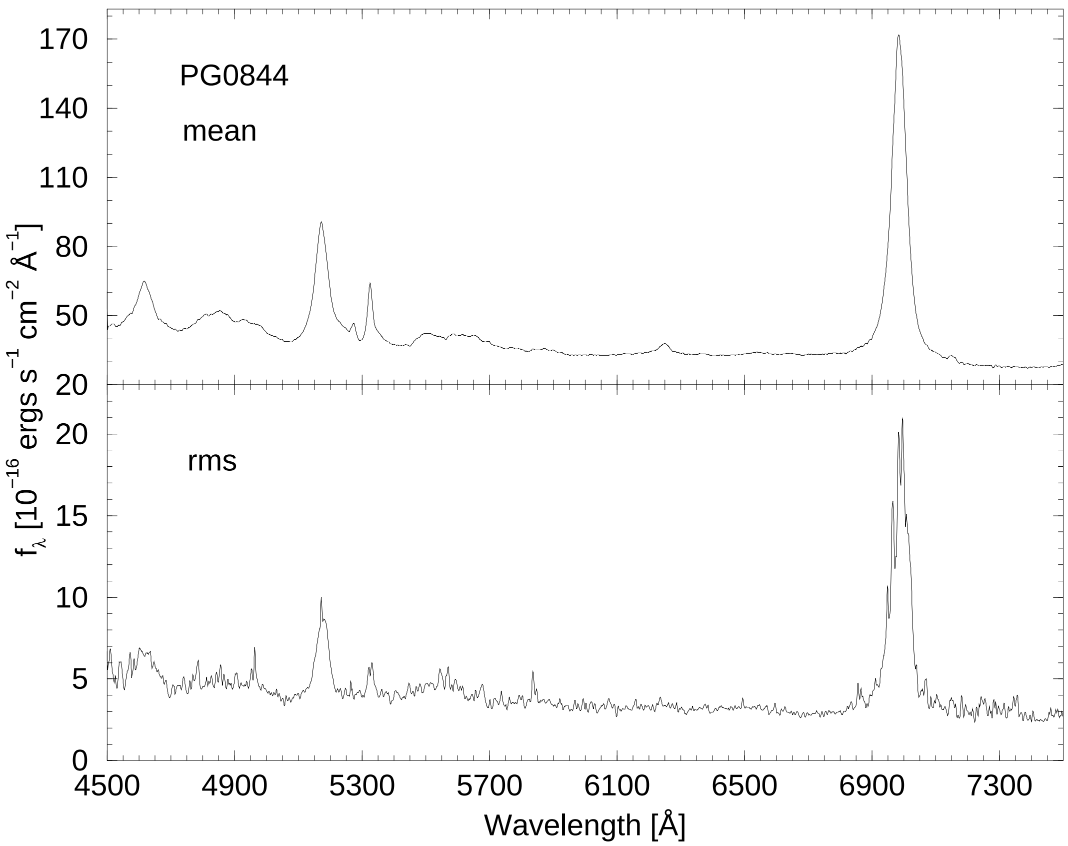

Fig. 3.1.— PG 0844 mean spectrum (*top*) and rms spectrum (*bottom*).

the errors in the line and continuum measurements, we added in quadrature an error corresponding to our estimate for the differential uncertainty of an individual spectrum.

For time series analysis purposes, we generally used the continuum on the blue side of Hβ. In several cases where the blue side of Hβ has an inferior light curve (due to, e.g., atmospheric absorption bands and/or superposed emission line blends) we chose continuum bands around Hγ. Table 3.2 lists in bold font the continuum band chosen for each object. Both the continuum bands and the emission lines can be affected by the contribution of variable Fe II lines However, correcting for this effect is beyond the scope of the present study. Similarly, our Balmer line measurements might be contaminated by narrow forbidden emission-lines. Though we measure Hβ without the [O III] $\lambda\lambda$4995, 5007 lines (since there is a clear separation between them) we cannot do so for the [N II] $\lambda\lambda$6548, 6583 lines blended with the Hα line. However, we note that contamination from narrow lines should not affect our time series analysis since this analysis relies on the variable parts of the lines, and the narrow lines clearly do not vary in AGNs.

The AGN continuum is the dominant contributor to the flux in the broad band photometry. To improve the sampling of the continuum light curves, we therefore merged the photometric B band light curves of Giveon et al. (1999) into the spectrophotometric continuum light curves (see also Maoz et al. 1994). The photometric campaign lasted 7 years and we extended the observations of the present 28 objects for six more months to overlap with the spectrophotometric campaign. Those last photometric observations were reduced and added to the light curves as explained in Giveon et al. (1999).

In order to intercalibrate the photometric and spectrophotometric light curves of each object, we examined all pairs of spectrophotometric and photometric observations separated in time by less than a few days (typically $\sim$5 days, and in some cases up to $\sim$10 days). This produced 10 to 15 pairs of points per object. A linear least-squares fit between the spectrophotometric continuum fluxes and the photometric fluxes (the magnitudes of Giveon et al. (1999) translated to fluxes) was used to merge the two light curves.

For each object the total number of photometric and spectrophotometric observations is given in Table 3.1, columns (8) & (9) (the sum of the two columns give the total number of points in the continuum light curve). The number of points in each emission-line light curve is given in Table 3.4, column (6). Note that for particular emission-lines in some objects, some data points are missing due to cosmic-rays contaminations, insufficient wavelength coverage, or low S/N in some spectra. Light curves for the 17 objects which have more than 20 spectrophotometric data points are presented in Fig. 3.2[2]. The absolute calibration uncertainties are not shown in the error bars in our light curves. The error bars reflect only the measurement and differential uncertainties, which are of order 1%–2%. Each of the remaining 11 objects in our sample had less than 10 spectrophotometric observations over the 7.5 year period. Such sampling is insufficient to determine the line-to-continuum lag and these objects will not be discussed further in this thesis.

3.4 Time Series Analysis

The continuum variability properties of our quasar sample are extensively discussed in Giveon et al. (1999). All 17 objects presented here underwent optical continuum variability (at 5100 Å rest wavelength) of order of 25% to 150%, measured from minimum to

[2] A machine-readable version of these data is available upon request from the author

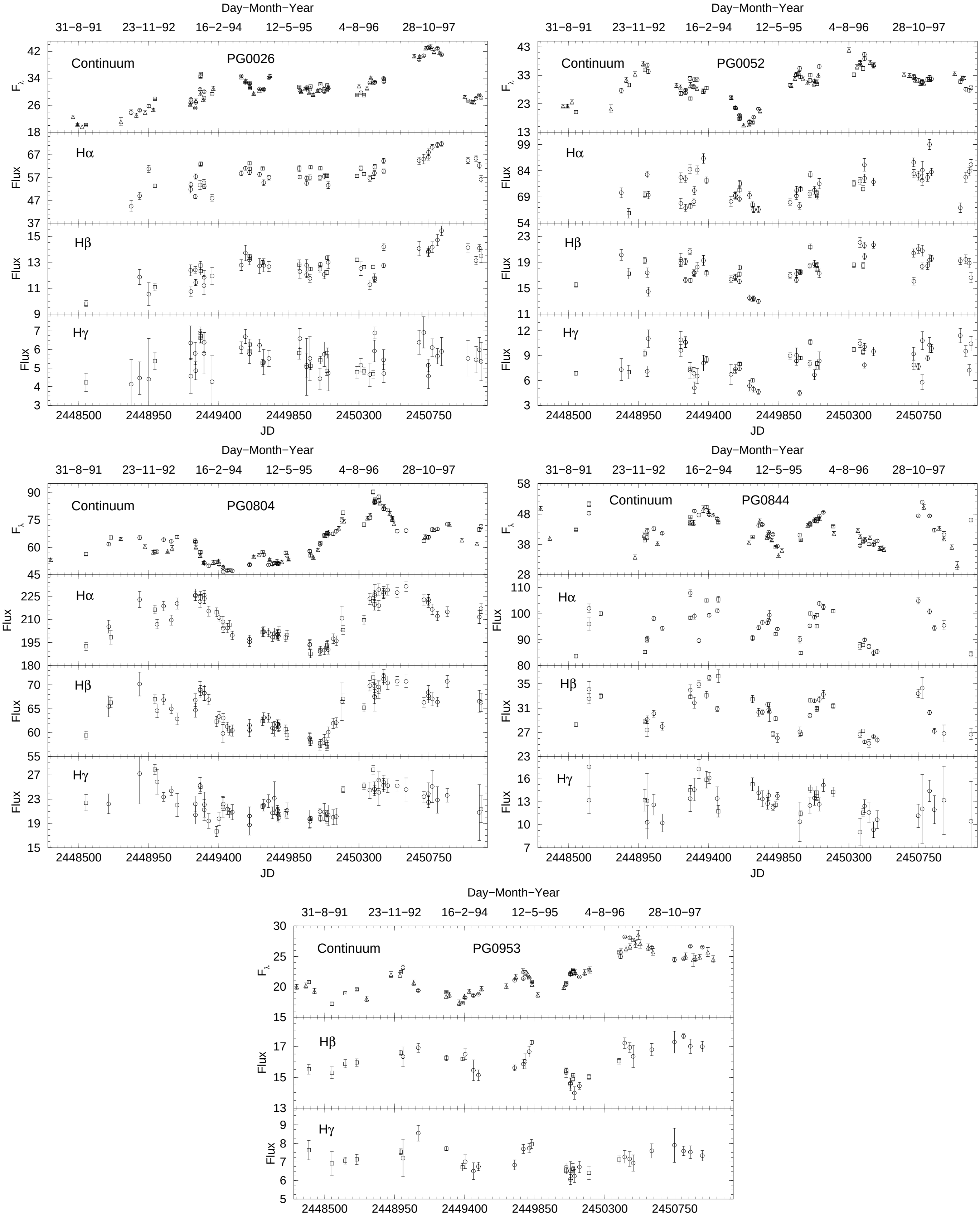

Fig. 3.2.— Light curves for 17 PG quasars. Circles are spectrophotometric data from WO, squares are spectrophotometric data from SO, triangles are photometric data from Wise. Continuum bands shown, f_λ, are the bands listed in bold-font in Table 3.2, and are given in units of $10^{-16}\,\mathrm{erg\,s^{-1}\,cm^{-2}\,\AA^{-1}}$. Emission line fluxes are in units of $10^{-14}\,\mathrm{erg\,s^{-1}\,cm^{-2}}$. Horizontal axis given in Julian Day (bottom) and date (top).

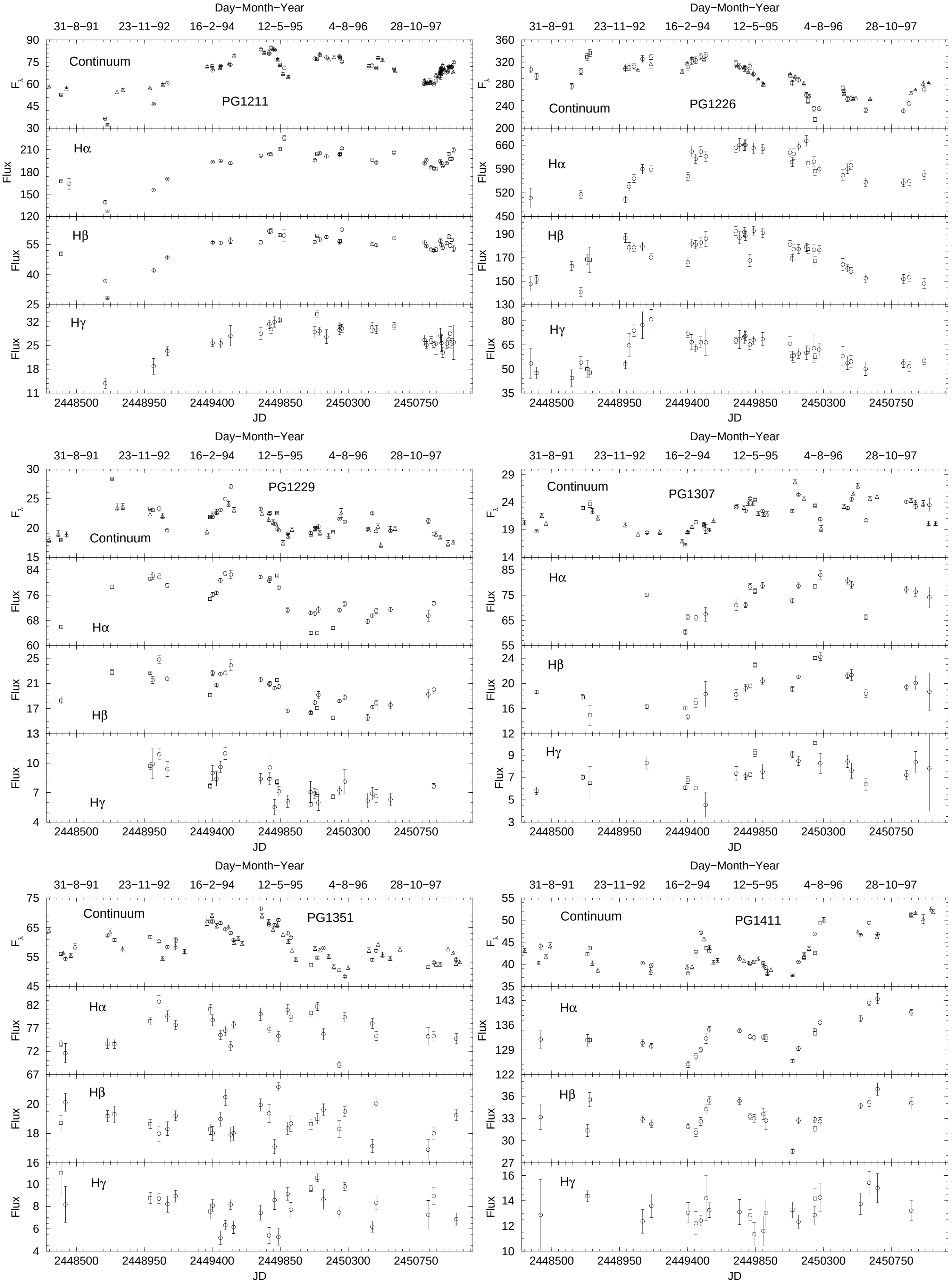

Fig. 3.2.— *Continued*

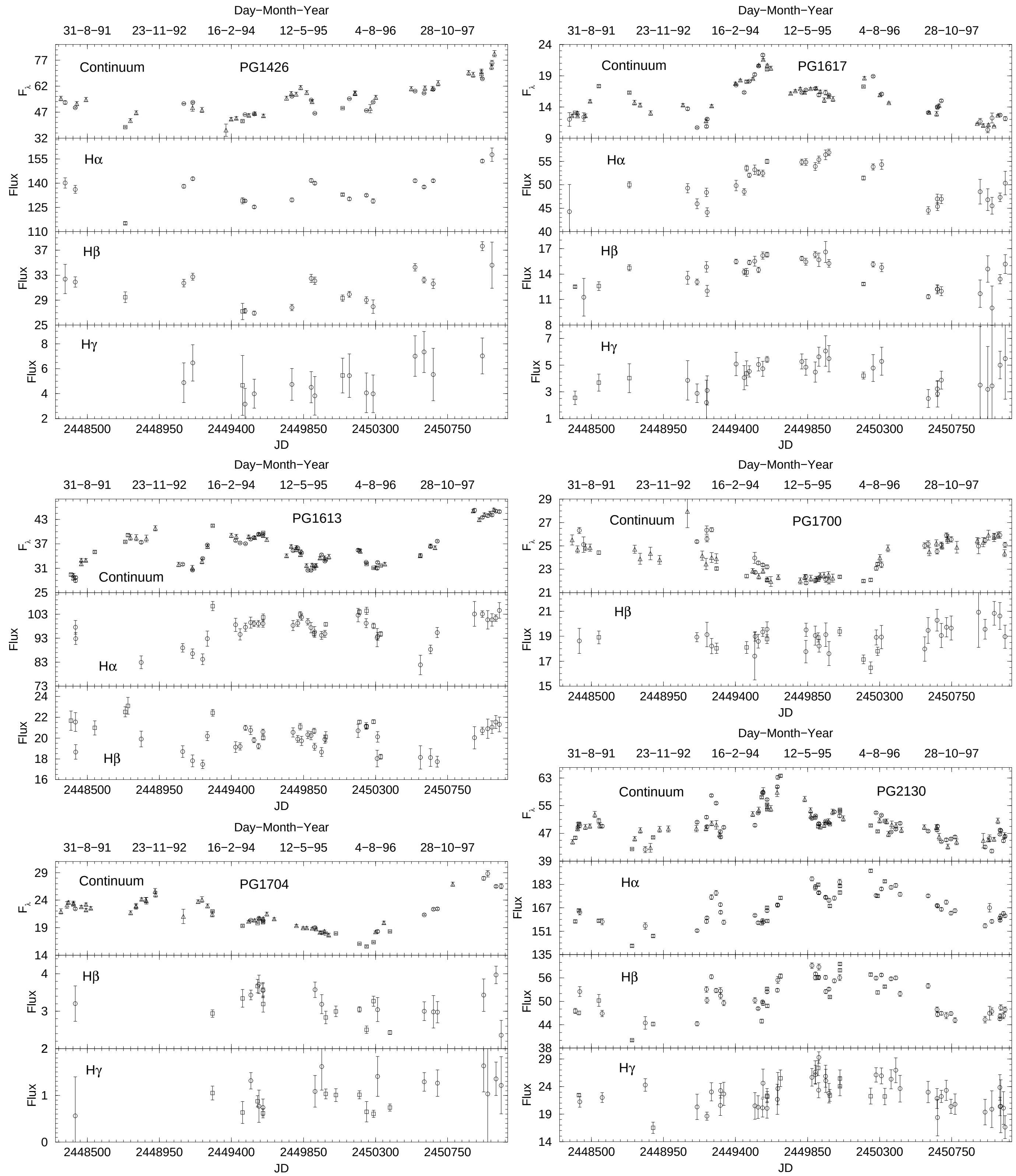

Fig. 3.2.— *Continued*

maximum flux. In order to compare the line variability to the continuum variability in each quasar, we define an intrinsic normalized variability measure, $\sigma_N = 100\sqrt{\sigma^2 - \delta^2}/\bar{f}$, where $\bar{f}$ and σ are the average and the rms of the flux in a given light curve, respectively, and δ is the mean error of all data points in that light curve. This measure is less sensitive to noise and outliers, than the minimum to maximum ratio. The few cases where $\sigma^2 - \delta^2$ of a light curve is slightly below zero are consistent with no variability. Table 3.3 summarizes σ_N for the 5100 Å continua and all the available emission-lines light curves. In general we find that all of the Balmer emission lines in a specific object have about the same level of variability. In all objects the variability of the emission lines is smaller than the continuum variability. In the few cases where those trends do not hold, it appears that they are masked by noise (e.g., most cases in which the emission line varies with a larger amplitude than the continuum involve Hγ, which has worse S/N than Hα and Hβ).

The main goal of this project has been the determination of the time lag between the continuum and the Balmer-line flux variations in high luminosity AGNs. To quantify this lag, we use two methods for correlating the line and continuum light curves. The first method is the interpolated cross-correlation function (ICCF) of Gaskell & Sparke (1986) and Gaskell & Peterson (1987), as implemented by White & Peterson (1994; and see also a review by Gaskell 1994). The second method is the z-transformed discrete correlation function (ZDCF) of Alexander (1997) which is an improvement of the discrete correlation function (DCF; Edelson & Krolik 1988). The ZDCF applies Fisher's z transformation to the correlation coefficients, and uses equal population bins rather than the equal time bins used in the DCF. For the data presented below the two independent methods are in excellent agreement. Hence, in the following analysis we will use only the ICCF.

The uncertainties in the cross correlation lag determination can be estimated using the model-independent FR/RSS Monte Carlo method described by Peterson et al. (1998b). In this method, each Monte Carlo simulation is composed of two parts: The first is a "random subset selection" (RSS) procedure which consists of randomly drawing, with replacement, from a light curve of N points a new sample of N points. After the N points are selected, the redundant selections are removed from the sample such that the temporal order of the remaining points is preserved. This procedure reduces the number of points in each light curve by a factor of $\sim 1/e$ and accounts for the effect that individual data points

Table 3.2. Integration limits for continuum bands and emission lines

Object (1)	Continuum (2)	Hγ (3)	Continuum (4)	Continuum (5)	Hβ (6)	Continuum (7)	Continuum (8)	Hα (9)	Continuum (10)
PG 0026	4790–4830	4920–5045	5070–5100	**5408–5468**	5508–5654	5818–5868	6998–7138	7304–7728	7730–7790
PG 0052	**4864–4914**	4926–5118	5418–5488	5418–5488	5518–5698	5908–5978	7028–7108	7398–7724	7725–7800
PG 0804	4680–4705	4710–4850	4880–4905	**5224–5264**	5266–5474	5598–5630	6746–6814	6940–7412	7472–7520
PG 0844	4503–4535	4536–4690	**4710–4750**	5048–5078	5098–5248	5414–5440	6708–6764	6848–7120	7248–7348
PG 0953	**5238–5278**	5284–5450	5472–5506	5846–5892	5906–6086	6288–6320	···	···	···
PG 1211	4525–4560	4625–4755	4780–4810	**5120–5160**	5180–5340	5490–5530	6670–6720	6900–7310	7480–7540
PG 1226	4925–4945	4946–5130	**5135–5165**	5494–5522	5530–5756	5888–5928	7034–7085	7250–7788	7789–7808
PG 1229	4500–4560	4560–4690	4694–4758	5052–5088	5094–5244	**5412–5456**	6562–6654	6838–7148	7244–7320
PG 1307	4870–4915	4938–5088	5104–5154	**5458–5488**	5508–5698	5864–5914	7050–7100	7400–7740	7750–7800
PG 1351	4585–4645	4646–4781	4815–4850	**5048–5128**	5196–5352	5545–5605	6638–6770	6898–7322	7362–7432
PG 1411	4570–4600	4650–4790	4805–4835	**5155–5185**	5201–5382	5520–5555	6700–6760	6870–7360	7490–7560
PG 1426	4565–4605	4605–4775	4730–4796	**5105–5145**	5170–5360	5515–5555	6680–6730	6930–7270	7490–7550
PG 1613	···	···	···	**5300–5350**	5360–5566	5740–5790	7000–7050	7013–7742	7743–7803
PG 1617	4650–4700	4745–4950	4930–4960	**5250–5295**	5310–5550	5672–5722	6898–6968	7118–7498	7540–7580
PG 1700	···	···	···	**6030–6080**	6120–6410	6520–6570	7760–8015	8245–8689	8690–8730
PG 1704	5800–5865	5900–6025	**6040–6100**	6460–6520	6575–6735	7020–7100	···	···	···
PG 2130	4460–4490	4533–4710	4710–4735	**5048–5084**	5094–5240	5394–5440	6498–6598	6798–7118	7246–7318

Note—Wavelengths in units of Å at the observer's frame. The bold-font ranges are the continuum bands shown in Fig. 3.2.

Table 3.3. Variability Measure σ_N

Object	Cont[a]	Hα	Hβ	Hγ
PG 0026	14.7	9.3	8.0	8.4
PG 0052	17.6	10.1	11.4	20.2
PG 0804	18.2	5.8	6.2	8.7
PG 0844	10.1	6.7	9.7	10.0
PG 0953	13.3	···	5.5	6.2
PG 1211	16.2	10.3	12.2	12.8
PG 1226	11.9	7.7	7.8	12.3
PG 1229	10.9	8.1	12.5	17.9
PG 1307	9.8	7.9	12.8	14.3
PG 1351	9.8	4.0	4.7	···
PG 1411	8.5	3.4	5.1	2.8
PG 1426	15.3	7.0	8.8	···
PG 1613	12.4	5.6	6.1	···
PG 1617	17.3	7.4	11.5	···
PG 1700	6.8	···	3.2	···
PG 1704	14.5	···	10.7	18.0
PG 2130	9.3	6.2	8.9	8.9

[a]Continuum at rest wavelength ~5100 Å (see Table 3.2 column (7) for exact wavelength intervals).

have on the cross-correlation. The second part is "flux randomization" (FR) in which the observed fluxes are altered by random Gaussian deviates scaled to the uncertainty ascribed to each point. This procedure simulates the effect of measurement uncertainties. Peterson et al. (1998b) demonstrate that under a wide variety of realistic conditions, the combined FR/RSS procedure yields conservative errors, and real uncertainties may, in fact, be somewhat smaller.

All emission-line light curves presented in Fig. 3.2 were cross correlated with their corresponding continuum light curves. The results of the cross-correlation analysis are presented in Table 3.4. The object name is given in Column (1), and the Balmer line in question is given in column (2). For the ICCF we list the centroid time-lag, τ_{cent}, (computed from all points within 80% of the peak value, r_{max}) in column (3), the peak position, τ_{peak}, in column (4), and the peak value, r_{max}, in column (5). In column (6) we list the total number of points in the emission-line light curve (the total number of points in the continuum light curve is given in Table 3.1 columns [8] & [9]). The uncertainties given for τ_{cent} and τ_{peak} were computed with the FR/RSS method using $\sim 10,000$ Monte Carlo realizations which were used to build up a cross-correlation peak distribution (CCPD; Maoz & Netzer 1989). The range of uncertainties contains 68% of the Monte Carlo realizations in the CCPD and thus would correspond to 1σ uncertainties for a normal distribution. In addition to the cross-correlation results, we also list in Table 3.4 velocity measurements for each line. Column (7) lists the mean full-width at half maximum (FWHM) of the emission-line, and column (8) lists the line FWHM measured from the rms spectrum (see § 4.4 below).

Table 3.4. Cross-Correlation Results and Velocity Measurements

Object	line	τ_{cent} (days)	τ_{peak} (days)	r_{max}	Number Obs.	v_{FWHM}(mean) $\mathrm{km\,s^{-1}}$	v_{FWHM}(rms) $\mathrm{km\,s^{-1}}$
(1)	(2)	(3)	(4)	(5)	(6)	(7)	(8)
PG 0026	Hα	132^{+29}_{-31}	108^{+63}_{-47}	0.81	55	1527 ± 99	1179 ± 76
PG 0026	Hβ	125^{+29}_{-36}	85^{+36}_{-28}	0.84	53	2100 ± 140	1358 ± 91
PG 0052	Hα	211^{+66}_{-44}	193^{+85}_{-93}	0.68	53	2690 ± 510	3280 ± 630
PG 0052	Hβ	99^{+30}_{-31}	75^{+22}_{-15}	0.75	56	3990 ± 240	4550 ± 270
PG 0052	Hγ	90^{+27}_{-20}	69^{+19}_{-9}	0.74	56	4050 ± 300	5120 ± 380
PG 0804	Hα	193^{+20}_{-17}	187^{+29}_{-37}	0.83	70	2757 ± 55	2909 ± 58
PG 0804	Hβ	151^{+26}_{-24}	118^{+34}_{-30}	0.85	70	2984 ± 51	2430 ± 42
PG 0804	Hγ	108^{+39}_{-38}	82^{+67}_{-46}	0.74	67	3120 ± 150	2470 ± 120
PG 0844	Hα	39^{+16}_{-16}	37^{+19}_{-24}	0.74	46	2210 ± 100	2700 ± 120
PG 0844	Hβ	13^{+14}_{-11} [a]	10^{+20}_{-19}	0.79	48	2730 ± 120	2830 ± 120
PG 0844	Hγ	31^{+77}_{-49}	28^{+89}_{-43}	0.58	45	3210 ± 360	4770 ± 530
PG 0953	Hβ	187^{+27}_{-33}	207^{+22}_{-26}	0.72	35	2885 ± 65	2723 ± 62
PG 0953	Hγ	203^{+36}_{-59}	213^{+24}_{-73}	0.54	34	3110 ± 130	3860 ± 160
PG 1211	Hα	116^{+38}_{-46}	69^{+123}_{-33}	0.87	37	1479 ± 74	1051 ± 53
PG 1211	Hβ	103^{+32}_{-44}	28^{+142}_{-26}	0.87	36	1832 ± 81	1479 ± 66
PG 1211	Hγ	145^{+66}_{-47}	117^{+120}_{-68}	0.86	34	2380 ± 150	2200 ± 140
PG 1226	Hα	514^{+65}_{-64}	447^{+191}_{-65}	0.71	34	2810 ± 190	1330 ± 88
PG 1226	Hβ	382^{+117}_{-96}	342^{+145}_{-89}	0.78	39	3416 ± 72	2742 ± 58
PG 1226	Hγ	307^{+57}_{-86}	306^{+52}_{-61}	0.79	39	3760 ± 170	3440 ± 160
PG 1229	Hα	71^{+39}_{-46}	48^{+85}_{-10}	0.78	32	2960 ± 110	3350 ± 130
PG 1229	Hβ	36^{+32}_{-18}	20^{+10}_{-20}	0.80	33	3440 ± 120	3490 ± 120
PG 1229	Hγ	16^{+27}_{-39}	7^{+36}_{-49}	0.81	29	3400 ± 330	3000 ± 290
PG 1307	Hα	179^{+94}_{-145}	228^{+97}_{-169}	0.67	20	3690 ± 140	3280 ± 120
PG 1307	Hβ [b]	108^{+46}_{-115}	32^{+49}_{-96}	0.59	23	4190 ± 210	5260 ± 270
PG 1307	Hγ	201^{+72}_{-168}	252^{+105}_{-426}	0.64	23	4030 ± 240	3400 ± 200
PG 1351	Hα	247^{+162}_{-78}	258^{+286}_{-76}	0.49	29	1170 ± 160	950 ± 130

Table 3.4—Continued

Object (1)	line (2)	τ_{cent} (days) (3)	τ_{peak} (days) (4)	r_{max} (5)	Number Obs. (6)	v_{FWHM}(mean) km s^{-1} (7)	v_{FWHM}(rms) km s^{-1} (8)
PG 1411	Hα	103^{+40}_{-37}	71^{+17}_{-18}	0.87	24	2172 ± 57	2135 ± 56
PG 1411	Hβ	118^{+72}_{-71}	67^{+157}_{-31}	0.64	24	2456 ± 96	2740 ± 110
PG 1426	Hα	90^{+46}_{-52}	66^{+56}_{-59}	0.87	20	5450 ± 150	4850 ± 130
PG 1426	Hβ	115^{+49}_{-68}	61^{+81}_{-66}	0.83	20	6250 ± 390	5520 ± 340
PG 1613	Hα	43^{+40}_{-22}	35^{+185}_{-26}	0.43	44	6060 ± 210	1598 ± 56
PG 1613	Hβ	44^{+20}_{-23}	29^{+36}_{-31}	0.43	48	7000 ± 380	2500 ± 140
PG 1617	Hα	111^{+31}_{-37}	83^{+45}_{-32}	0.80	32	4270 ± 410	3160 ± 300
PG 1617	Hβ	78^{+30}_{-41}	83^{+32}_{-55}	0.75	34	5120 ± 850	3880 ± 650
PG 1617	Hγ	43^{+117}_{-58}	50^{+148}_{-49}	0.67	32	3100 ± 750	3110 ± 750
PG 1700	Hβ	$114^{+246\ \mathrm{a}}_{-235}$	14^{+296}_{-177}	0.54	37	2180 ± 170	1970 ± 150
PG 1704	Hβ	437^{+252}_{-391}	527^{+263}_{-407}	0.43	24	890 ± 280	400 ± 120
PG 2130	Hα	237^{+53}_{-28}	194^{+252}_{-33}	0.59	64	2022 ± 88	2236 ± 97
PG 2130	Hβ	188^{+136}_{-27}	186^{+144}_{-103}	0.66	64	2410 ± 150	3010 ± 180
PG 2130	Hγ	196^{+130}_{-46}	218^{+104}_{-102}	0.72	54	2850 ± 190	3050 ± 210

[a]Computed from all points within 60% of the peak value, r_{max}, due to noisiness of the data.

[b]The peak of the ICCF measured is the one consistent with the ZDCF results and with the Hα and Hγ results.

Fig. 3.3 presents the cross-correlation functions (CCFs) for the 40 out of 46 emission-line–continua pairs having peak correlation coefficients above 0.4 . All 40 CCFs, for 17 objects with several emission lines each, indicate a positive time lag of the Balmer lines with respect to the optical continuum. The time lags are of order a few weeks to a few months, and the CCF peaks are highly significant for most lines. In a few cases, τ_{cent} and τ_{peak} are consistent with a zero time lag, given the uncertainties. However, we attribute this to the fact that these few emission-line light curves are noisy, and to the conservative error estimate of the FR/RSS method. Choosing our best lag determination (see below), i.e., avoiding noisy results obtained from weak lines (generally Hγ), we conclude that in all 17 quasars, a time lag has been detected in one or more of the Balmer lines.

When comparing the Hβ time-lags for PG 0804 and PG 0953 obtained in Kaspi et al. (1996) to the ones deduced here, we find an increase of about 65% for both objects although the results are consistent at the 2σ level. The luminosities of both objects have also increased during the second half of the monitoring period, compared to the first half which was presented in Kaspi et al. (1996). Such a change of the time lag between different observing seasons is seen in lower-luminosity AGNs (e.g., NGC 4151 and NGC 5548) and is thought to reflect a real effect, rather than a measurement error. It may involve a change in the BLR, which becomes larger when the object gets brighter.

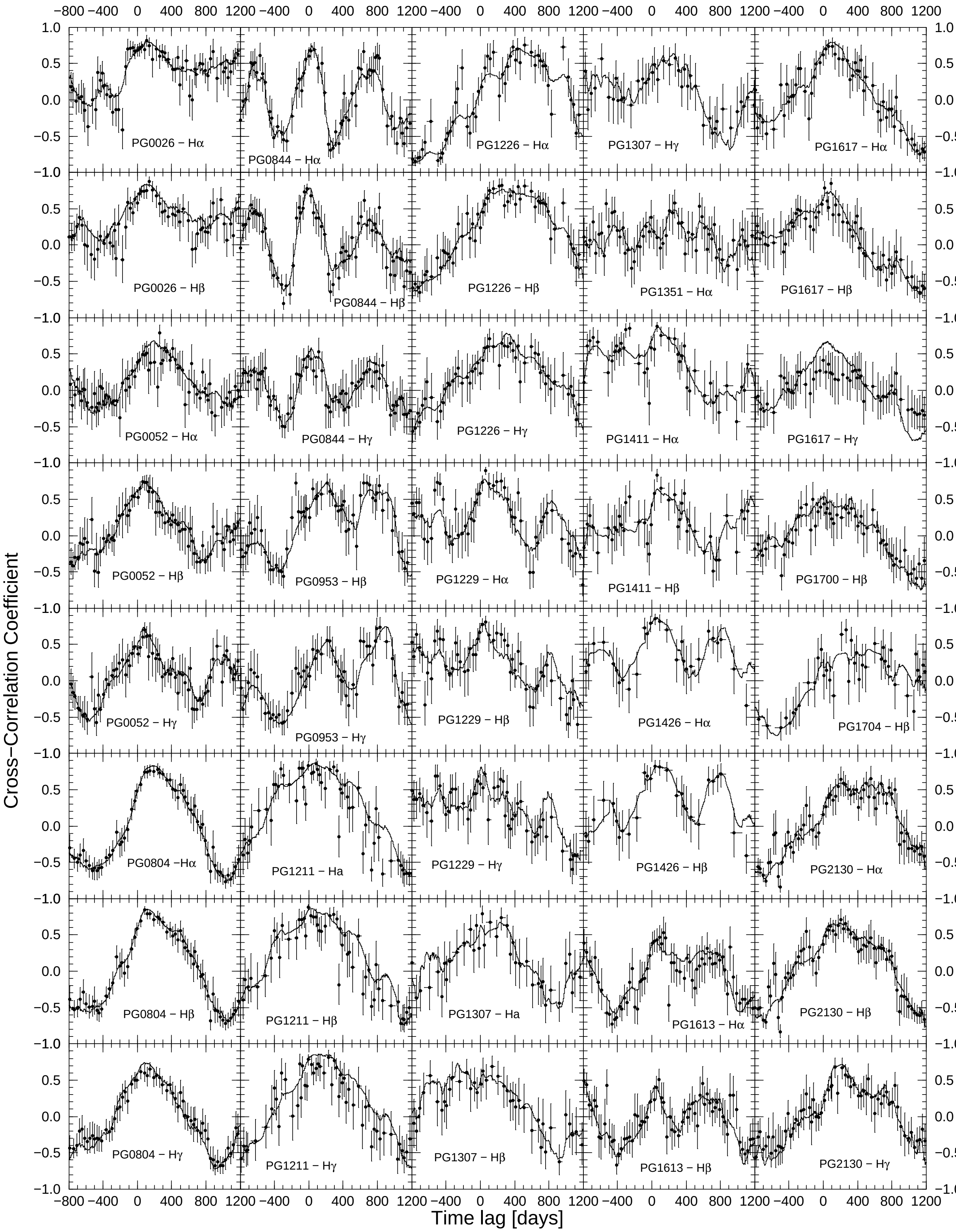

Fig. 3.3.— Cross correlation functions: ICCF *(solid line)* and ZDCF *(circles with error bars)* for all emission lines with peak correlation coefficients > 0.4. See text and Table 3.4 for details.

Chapter 4

The Size-Mass-Luminosity Relationships

4.1 Introduction

Converting the observable Balmer emission-line time lags, line widths, and continuum fluxes into interesting physical parameters, namely, BLR sizes, and AGNs central masses and luminosities, is not straightforward. We therefore discuss each in some detail below. We analyze our new data together with data for other AGNs, monitored over the past decade, that have reliable estimates of emission-line time lags. Wandel et al. (1999) have uniformly analyzed the reverberation mapping data of 17 Seyfert 1s, and deduced time lags using the same techniques described in the previous section. Combining their results with the present ones, we obtain, for the first time, reliable Size-Mass-Luminosity relations for 34 AGNs spanning over 4 orders of magnitudes in continuum luminosity. Our analysis is similar to that of Wandel et al. (1999), and the few significant differences are noted below. A paper describing these results has been submitted to *The Astrophysical Journal*.

We apply below linear regression analysis to the data. Unless otherwise noted, the method is the one described by Press et al. (1992), which is based on an iterative process to minimize χ^2, taking into account the uncertainties in both coordinates. In some of our data, the uncertainties are asymmetric (e.g., as a result of the FR/RSS method and the use of the CCPD), and since the fitting method does not account for this, we use the mean of the positive and negative uncertainty estimates in a given coordinate for each data point. We find that similar results are obtained when using the Pearson linear correlation and the Spearman rank-order correlation. We present below only Pearson coefficients.

4.2 The Size of the BLR

Caution must be exercised when using time lags to estimate BLR sizes because there are various assumptions and complications involved:

1. The CCF is sensitive to the characteristics of the continuum variation, since it is a convolution of the transfer function and the continuum autocorrelation function (Penston 1991; Peterson 1993). Hence, there is a dependence of the peak/centroid of the CCF on the nature of the continuum variability. An illustration of this dependence is given by Netzer & Maoz (1990).

2. A real change in BLR size and geometry, over the 7 year period, is not out of the question. Using the time-lags measured here, and the observed FWHMs, we deduce a dynamical (crossing) time of the order of 30 years for the more luminous objects and about a year for the lowest luminosity Seyfert galaxies.

3. The measured time lag can be affected by the nonlinear response of some emission-line intensities to continuum variations. Nonlinear responses were suggested by various studies (O'Brien, Goad, & Gondhalekar, 1995; Shields, Ferland, & Peterson, 1995) and also discussed in chapter 5.

4. The ionizing continuum variations may behave differently from the observed optical continuum. Most studies show the continuum varies in phase with little or no time delay (albeit, with smaller amplitude at longer wavelengths) over a wide wavelength range. There are, however, some exceptions (e.g., Peterson et al. 1998b) and it is clear that a full understanding of the continuum emission processes is yet to be obtained. An extreme example is shown by Nandra et al. (1998) who found that the X-ray and UV continuum are not strongly correlated at zero time lag in NGC 7469; with some X-ray emission peaks lagging behind the UV peaks by $\sim$4 days.

5. For a given object, different lines from different ions have different time lags. Thus, considering the entire sample, the same emission lines should be used in all objects.

Balmer lines are useful since their lag has been measured in most AGNs where reverberation mapping has been attempted. However, as argued in chapter 5, the theoretical modeling of these lines is very uncertain and they are useful mostly because they provide a uniform base for comparing low luminosity Seyferts with high luminosity quasars.

6. There might be a contribution of other emission lines, blended with the emission lines in question but still undetectable. These emission lines might have a different time lag, hence affecting the time lag measured for the lines in question. An example is the variable Fe II emission-lines near Hβ, as discussed earlier.

A possible manifestation of some of these difficulties is the fact that, in some objects, different monitoring campaigns result in different time lags. The effect was first noted in the Hβ time lags found by Peterson et al. (1991; $\sim$7 days) and Netzer et al. (1990; $\sim$20 days) for the Seyfert galaxy NGC 5548. Other examples are the larger time lag deduced for PG 0804 and PG 0953 in this chapter, compared with Kaspi et al. (1996; see above), and the different time lags in each observing season for NGC 5548 (Peterson et al. 1999).

Bearing in mind the above points, we convert the time lags (deduced from the ICCF centroid) of the Balmer emission lines directly into BLR sizes (hereafter R_{BLR}) after applying a cosmological $(1+z)^{-1}$ factor. Time lags derived from multiple Balmer lines are consistent with each other for individual quasars. The derived linear relations are:

$$R_{BLR}(H\alpha) = (1.19 \pm 0.23) R_{BLR}(H\beta) + (13 \pm 19) \quad , \tag{4.1}$$

and

$$R_{BLR}(H\gamma) = (0.96 \pm 0.30) R_{BLR}(H\beta) - (3 \pm 33) \quad , \tag{4.2}$$

i.e., both consistent with a slope of 1.0 and a zero intercept. In view of this, we adopt the mean time lag measured for Hα and Hβ as the best estimate of R_{BLR}. The relatively low equivalent width makes Hγ harder to measure and we do not include it in the estimate of BLR size. In several objects only one of Hα or Hβ is available and we thus use a single line. For the Seyfert 1s we use the Hβ time lags from Wandel et al. (1999) and correct it by the $(1+z)^{-1}$ factor. Values for R_{BLR} for all objects are listed in Table 4.1, column (2).

4.3 Luminosity Determination

The exact shape of the spectral energy distribution (SED) of most objects in our sample is unknown. Furthermore, much of this luminosity is emitted in the unobservable far UV and there are still fundamental, unsolved, issues concerning the shape of the continuum (e.g., Zheng et al. 1997, Laor et al. 1997, and references therein). Even in those cases where multiwavelength data exist, they are generally obtained at different epochs, and variability may render a simple integration over the wide range inappropriate. (See also a discussion by Dumont, Collin-Souffrin, & Nazarova; 1998, which demonstrates how poor the determination of the SED is even for one of the best studied AGNs, NGC 5548.) Another problem is intrinsic reddening, which varies from object to object. It is thus unclear what fraction of the total luminosity we are sampling.

An additional complication is the contribution of the host galaxy to the luminosity of the nucleus. While in high-luminosity AGNs this contribution is negligible, this is not the case in low-luminosity objects. Determining the host galaxy flux within a given spectrograph aperture is a complicated task, attempted only in a few cases (e.g., Peterson et al. 1995). The implementation of such corrections is beyond the scope of this work.

Following Wandel et al. (1999), we use λL_λ at 5100 Å as our luminosity measure. This luminosity is calculated assuming zero cosmological constant, deceleration parameter $q_0 = 0.5$, and Hubble constant $H_0 = 75\,\mathrm{km\,s^{-1}\,Mpc^{-1}}$ (note that these values are different from the ones used by Wandel et al. 1999). This monochromatic luminosity can be translated into an integrated 0.1—1 μm luminosity, assuming a power-law continuum of the form $f_\nu \propto \nu^{-0.5}$, as in Maoz et al. (1994) and Kaspi et al. (1996), by applying a correction factor of 3.1. For the 5100 Å point, we use the continuum measurement on the red side of Hβ (see wavelength ranges in column (7) of Table 3.2). The uncertainty in this value is taken to be only due to the variation range of each object, and is represented by the rms of the light curve. The observed flux has been corrected for Galactic extinction using the A_B values in the NED database (see Table 3.1 column (7)) and a standard extinction curve (Savage & Mathis 1979). Monochromatic luminosities, λL_λ(5100 Å), are listed in Table 4.1, column (3).

We have also tried an alternative process to determine the optical luminosity. Using line-free bands in the optical spectra, we have fitted a continuum to the mean and rms

Table 4.1. Radii, Luminosities, & Masses

Object (1)	R_{BLR} (lt-days) (2)	$\lambda L_\lambda(5100\text{Å})$ 10^{44} ergs s^{-1} (3)	M (mean) $10^7 M_\odot$ (4)	M (rms) $10^7 M_\odot$ (5)
3C 120	42^{+27}_{-20}	0.73 ± 0.13	$2.3^{+1.5}_{-1.1}$	$3.0^{+1.9}_{-1.4}$
3C 390.3	$22.9^{+6.3}_{-8.0}$	0.64 ± 0.11	34^{+11}_{-13}	37^{+12}_{-14}
Akn 120	$37.4^{+5.1}_{-6.3}$	1.39 ± 0.26	$18.4^{+3.9}_{-4.3}$	$18.7^{+4.0}_{-4.4}$
F 9	$16.3^{+3.3}_{-7.6}$	1.37 ± 0.15	$8.0^{+2.4}_{-4.1}$	$8.3^{+2.5}_{-4.3}$
IC 4329A	$1.4^{+3.3}_{-2.9}$	0.164 ± 0.021	$0.5^{+1.3}_{-1.1}$	$0.7^{+1.8}_{-1.6}$
Mrk 79	$17.7^{+4.8}_{-8.4}$	0.423 ± 0.056	$5.2^{+2.0}_{-2.8}$	$10.2^{+3.9}_{-5.6}$
Mrk 110	$18.8^{+6.3}_{-6.6}$	0.38 ± 0.13	$0.56^{+0.20}_{-0.21}$	$0.77^{+0.28}_{-0.29}$
Mrk 335	$16.4^{+5.1}_{-3.2}$	0.622 ± 0.057	$0.63^{+0.23}_{-0.17}$	$0.38^{+0.14}_{-0.10}$
Mrk 509	$76.7^{+6.3}_{-6.0}$	1.47 ± 0.25	$5.78^{+0.68}_{-0.66}$	$9.2^{+1.1}_{-1.1}$
Mrk 590	$20.0^{+4.4}_{-2.9}$	0.510 ± 0.096	$1.78^{+0.44}_{-0.33}$	$1.38^{+0.34}_{-0.25}$
Mrk 817	$15.0^{+4.2}_{-3.4}$	0.526 ± 0.077	$4.4^{+1.3}_{-1.1}$	$3.54^{+1.03}_{-0.86}$
NGC 3227	$10.9^{+5.6}_{-10.9}$	0.0202 ± 0.0011	$3.9^{+2.1}_{-3.9}$	$4.9^{+2.6}_{-4.9}$
NGC 3783	$4.5^{+3.6}_{-3.1}$	0.177 ± 0.015	$0.94^{+0.92}_{-0.84}$	$1.10^{+1.07}_{-0.98}$
NGC 4051	$6.5^{+6.6}_{-4.1}$	0.00525 ± 0.00030	$0.13^{+0.13}_{-0.08}$	$0.14^{+0.15}_{-0.09}$
NGC 4151	$3.0^{+1.8}_{-1.4}$	0.0720 ± 0.0042	$1.53^{+1.06}_{-0.89}$	$1.20^{+0.83}_{-0.70}$
NGC 5548	$21.2^{+2.4}_{-0.7}$	0.270 ± 0.053	$12.3^{+2.3}_{-1.8}$	$9.4^{+1.7}_{-1.4}$
NGC 7469	$4.9^{+0.6}_{-1.1}$	0.553 ± 0.016	$0.65^{+0.64}_{-0.65}$	$0.75^{+0.74}_{-0.75}$
PG 0026	113^{+18}_{-21}	7.0 ± 1.0	$5.4^{+1.0}_{-1.1}$	$2.66^{+0.49}_{-0.55}$
PG 0052	134^{+31}_{-23}	6.5 ± 1.1	$22.0^{+6.3}_{-5.3}$	$30.2^{+8.8}_{-7.4}$
PG 0804	156^{+15}_{-13}	6.6 ± 1.2	$18.9^{+1.9}_{-1.7}$	$16.3^{+1.6}_{-1.5}$
PG 0844	$24.2^{+10.0}_{-9.1}$	1.72 ± 0.17	$2.16^{+0.90}_{-0.83}$	$2.7^{+1.1}_{-1.0}$
PG 0953	151^{+22}_{-27}	11.9 ± 1.6	$18.4^{+2.8}_{-3.4}$	$16.4^{+2.5}_{-3.0}$
PG 1211	101^{+23}_{-29}	4.93 ± 0.80	$4.05^{+0.96}_{-1.21}$	$2.36^{+0.56}_{-0.70}$
PG 1226	387^{+58}_{-50}	64.4 ± 7.7	$55.0^{+8.9}_{-7.9}$	$23.5^{+3.7}_{-3.3}$
PG 1229	50^{+24}_{-23}	0.94 ± 0.10	$7.5^{+3.6}_{-3.5}$	$8.6^{+4.1}_{-4.0}$
PG 1307	124^{+45}_{-80}	5.27 ± 0.52	28^{+11}_{-18}	33^{+12}_{-22}
PG 1351	227^{+149}_{-72}	4.38 ± 0.43	$4.6^{+3.2}_{-1.9}$	$3.0^{+2.1}_{-1.3}$
PG 1411	102^{+38}_{-37}	3.25 ± 0.28	$8.0^{+3.0}_{-2.9}$	$8.8^{+3.3}_{-3.2}$
PG 1426	95^{+31}_{-39}	4.09 ± 0.63	47^{+16}_{-20}	37^{+13}_{-16}
PG 1613	39^{+20}_{-14}	6.96 ± 0.87	$24.1^{+12.5}_{-8.9}$	$2.37^{+1.23}_{-0.88}$
PG 1617	85^{+19}_{-25}	2.37 ± 0.41	$27.3^{+8.3}_{-9.7}$	$15.4^{+4.7}_{-5.5}$
PG 1700	88^{+190}_{-182}	27.1 ± 1.9	6^{+13}_{-13}	5.0^{+11}_{-10}
PG 1704	319^{+184}_{-285}	35.6 ± 5.2	$3.7^{+3.1}_{-4.0}$	$0.75^{+0.63}_{-0.81}$
PG 2130	200^{+67}_{-18}	2.16 ± 0.20	$14.4^{+5.1}_{-1.7}$	$20.2^{+7.1}_{-2.4}$

spectra of all objects. We integrated those continua over the rest frame wavelength of 4500—6000 Å to obtain the mean luminosity and its range. We have found the results to be very similar to those obtained by using the monochromatic luminosity. Below, we use only $\lambda L_\lambda(5100$ Å$)$ as our luminosity measure.

4.4 Mass Determination

To estimate the central masses of the quasars we need to assume gravitationally dominated motions of the BLR clouds ($M \approx G^{-1}v^2r$). This assumption is discussed and justified by Wandel et al. (1999) and Peterson & Wandel (1999) for the Seyfert 1 galaxy NGC 5548. There are, however, several complications regarding the velocity field. Although it is generally believed that the line widths represent a Keplerian velocity, it is not exactly clear how to convert the observed profile into a velocity measure, since the observed profiles are different from the ones expected from simple Keplerian orbits of arbitrary inclinations. In the absence of such information, it is common to use the rest-frame FWHM of the emission line. As AGNs broad emission lines are composed of a narrow component superposed on a broader components, a unique FWHM determination is not straightforward. In particular, deblending the components is complicated since the line profiles cannot be represented by simple analytical functions. Also, the line profiles and widths are variable too, as is evident, for example, from the spectra obtained in this study. These variations can be due to real change in the BLR velocity field, or other reasons, such as blending with weak lines, or observational effects.

We use two different methods to estimate a typical velocity. In the first method, for each quasar we measure the FWHM of each line in all the spectra and calculate the mean FWHM, v_{FWHM}(mean), and its uncertainty (rms). This empirical way of estimating the scatter, accounts for all the uncertainties involved, such as spectral resolution, pixelation of the line profile, and uncertainties in continuum determination. The values are listed in Table 3.4 column (7).

The second method, proposed by Peterson et al. (1998a), uses the rms spectrum to compute the FWHM of the lines. In this method, constant features in the mean spectrum, (such as narrow forbidden emission lines, narrow components of the permitted emission lines, galactic absorptions, and constant continuum and broad-line features) are

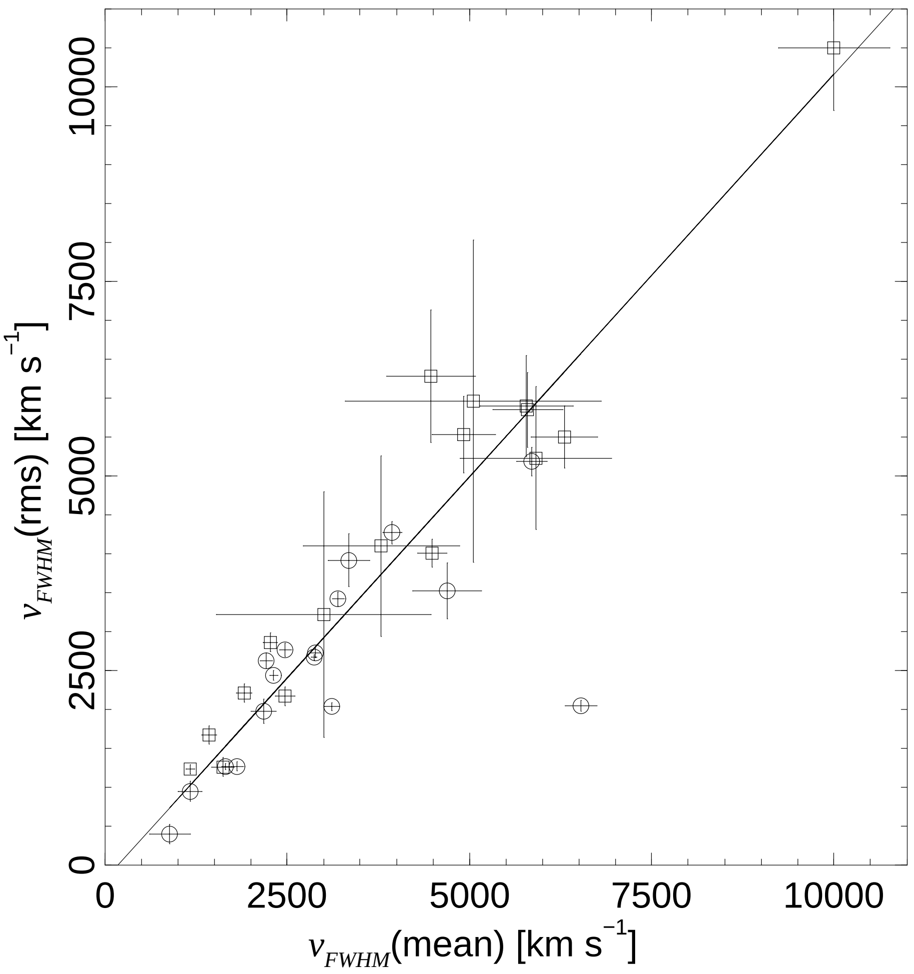

Fig. 4.1.— $v_{FWHM}(rms)$ vs. $v_{FWHM}(mean)$. PG quasars are marked with circles and Seyfert 1s are marked with squares. Solid line is the best fit to the data. The outlier is PG 1613, which apparently varies only in the core of its very broad lines. The object with the broadest lines is 3C 390.3 .

excluded, in principle. The FWHM measures only the part of the line which varied and thus corresponds to the R_{BLR} measured from the reverberation mapping[1]. In the rms spectrum of each object, we have measured the emission lines' FWHM, v_{FWHM}(rms) — listed in Table 3.4 column (8). There is no simple way to determine the uncertainty of v_{FWHM}(rms), and instead we have used the relative uncertainty in v_{FWHM}(mean).

Like the time lags derived using Hα and Hβ, the FWHM of all lines for a given object

[1]We note, however, that the rms spectra shown by Peterson et al. (1998a) often show narrow forbidden line residuals, probably due to variable seeing and small shifts in wavelength calibration. We see the same effect in our rms spectra as well. It is likely that the same effect operates on the narrow component of the Balmer lines, and therefore, in practice, the rms spectra are also not completely free of constant narrow components, and the degree of this contamination may vary from object to object.

are consistent with each other. Thus, for the PG quasars we use the average FWHM of Hα and Hβ. For the Seyfert 1 galaxies we have used the mean and rms FWHM quoted in Wandel et al. (1999). The FWHM from the rms spectrum versus the mean FWHM from all spectra is plotted in Fig. 4.1. We find the correlation to be highly significant with correlation coefficient of 0.888. A linear fit gives the relation

$$v_{FWHM}(rms) = (1.035 \pm 0.034) v_{FWHM}(mean) - (185 \pm 93) \quad , \tag{4.3}$$

which is plotted as the solid line in the diagram. The two velocity estimates are similar and Peterson et al.'s (1998a) preference for the FWHM determined from the rms spectra is not obviously empirically justified. However, in the subsequent analysis we will use both types of broad-line FWHM estimate for each object.

To determine v we correct v_{FWHM} by a factor of $\sqrt{3}/2$, to account for velocities in three dimensions and for using half of the FWHM. The virial "reverberation" mass is then:

$$M = 1.464 \times 10^5 \left(\frac{R_{BLR}}{lt\ days} \right) \left(\frac{v_{FWHM}}{10^3\ km\ s^{-1}} \right)^2 M_{\odot} \quad . \tag{4.4}$$

The results of this calculation are listed in columns (4) and (5) of Table 4.1 for v_{FWHM}(mean) and v_{FWHM}(rms), respectively.

4.5 Size—Luminosity Relation

The R_{BLR}-luminosity relation is presented in Fig. 4.2. The correlation coefficient is 0.827, and its significance level is 1.7×10^{-9}. A linear fit to the points gives

$$R_{BLR} = \left(32.9^{+2.0}_{-1.9} \right) \left(\frac{\lambda L_{\lambda}(5100 \mathring{A})}{10^{44}\ ergs\ s^{-1}} \right)^{0.700 \pm 0.033} \quad lt\ days \tag{4.5}$$

(solid line plotted on Fig. 4.2). Considering the Seyfert nuclei ($\log(\lambda L_{\lambda}(5100$ Å$) \lesssim 44.2$), or the PG quasars alone, we find only marginally significant correlations, probably because of the narrow luminosity ranges. A significant correlation emerges only when using the whole luminosity range.

The present result is remarkable for two reasons. First, earlier studies of this kind found a shallower slope, closer to 0.5 (Wandel et al. 1999). Second, under the assumptions that the shape of the ionizing continuum in AGNs is independent of L, and that all AGNs are

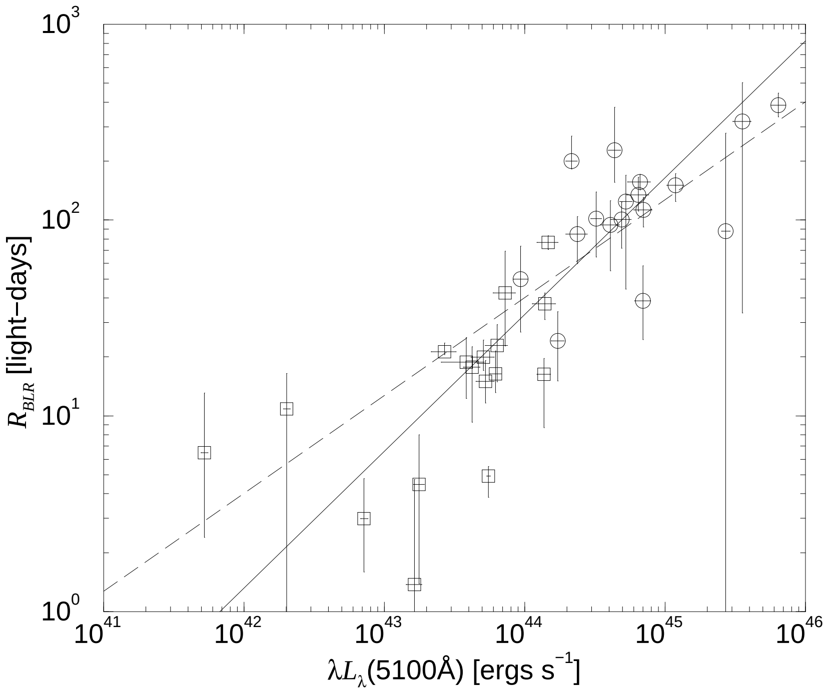

Fig. 4.2.— BLR size—luminosity relation. PG quasars are marked with circles and Seyfert 1s are marked with squares. The solid line is the best fit to the data. The dashed line is a fit with a 0.5 slope.

characterized by the same ionization parameter and BLR density (as suggested by the similar line ratios in low- and high-luminosity sources), one expects $R_{BLR} \propto L^{0.5}$ (a line with this slope was fit to the data and is shown as a dashed line in Fig. 4.2). Since the present analysis is based on a considerably larger sample than the one used by Wandel et al (1999), it is perhaps not surprising that the slope we found is different. As for the theoretical prediction, it is based on the assumption that the gas distribution, and hence also the mean BLR size, scales with the strength of the radiation field. Recent models (Kaspi and Netzer 1999 and references therein) show a wide distribution of properties across the BLR, and our present result suggests that the scaling with luminosity, and the uniformity of the mean ionization parameter inferred from AGNs spectra, should be re-examined. If an effective ionization parameter can be defined, our result suggests it may be a decreasing function of luminosity.

4.6 FWHM—Luminosity Relation

Our sample allows us to to address the issue of the velocity—luminosity relation in AGNs. Wandel & Yahil (1985) found a correlation coefficient of 0.5 between the Hβ full width at zero intensity (FW0I) and the 4000 Å continuum luminosity for a literature compilation of 94 AGNs. Joly et al. (1985; and references therein) also reported a weak correlation between the FW0I of Hβ and the optical luminosity in a similar collection of objects. Boroson & Green (1992) note the FW0I of Hβ is quite sensitive to noise and depends strongly on the quality of the Fe II subtraction. These authors found an anticorrelation coefficient of -0.275 between the Hβ FWHM and absolute V magnitude, significant at the 99% confidence level, in a sample of 87 PG quasars.

In addressing the issue of the velocity—luminosity relation we note that ours is *not* a complete sample, especially with the inclusion of the heterogeneous Seyfert sample. The results must therefore be treated with caution. As explained above, we have two estimates of the velocity field. The FWHMs from the mean spectrum are plotted against the luminosity in the bottom panel of Fig. 4.3. There is no significant correlation between the variables. However, if we omit the data point for the narrow line Seyfert 1, NGC 4051, which clearly deviates from the other points and highly influences the fit, we do obtain a marginally significant correlation. The correlation coefficient is -0.386, and its significance level is 2.7×10^{-2}. A linear fit gives

$$v_{FWHM}(mean) = \left(4108^{+66}_{-65}\right)\left(\frac{\lambda L_\lambda(5100\mathring{A})}{10^{44}\, ergs\, s^{-1}}\right)^{-0.271\pm0.012} \quad km\, s^{-1} \tag{4.6}$$

FWHMs from the rms spectrum versus luminosity are plotted in the top panel of Fig. 4.3. The correlation coefficient is -0.540, and the significance level is 1.2×10^{-3}. A linear fit is

$$v_{FWHM}(rms) = \left(3752^{+57}_{-56}\right)\left(\frac{\lambda L_\lambda(5100\mathring{A})}{10^{44}\, ergs\, s^{-1}}\right)^{-0.267\pm0.010} \quad km\, s^{-1} \tag{4.7}$$

Thus, we find significant anticorrelations, in our incomplete sample, between the FWHM of the Balmer lines and the luminosity of the objects such that $v_{FWHM} \propto L^{-0.27\pm0.01}$. Our result indicates a stronger anticorrelation coefficient when $v_{FWHM}(rms)$ is used. While the above studies used only one epoch for each quasar in their measurements, our study uses the means of the luminosities and velocities for each object over 7.5 years, and

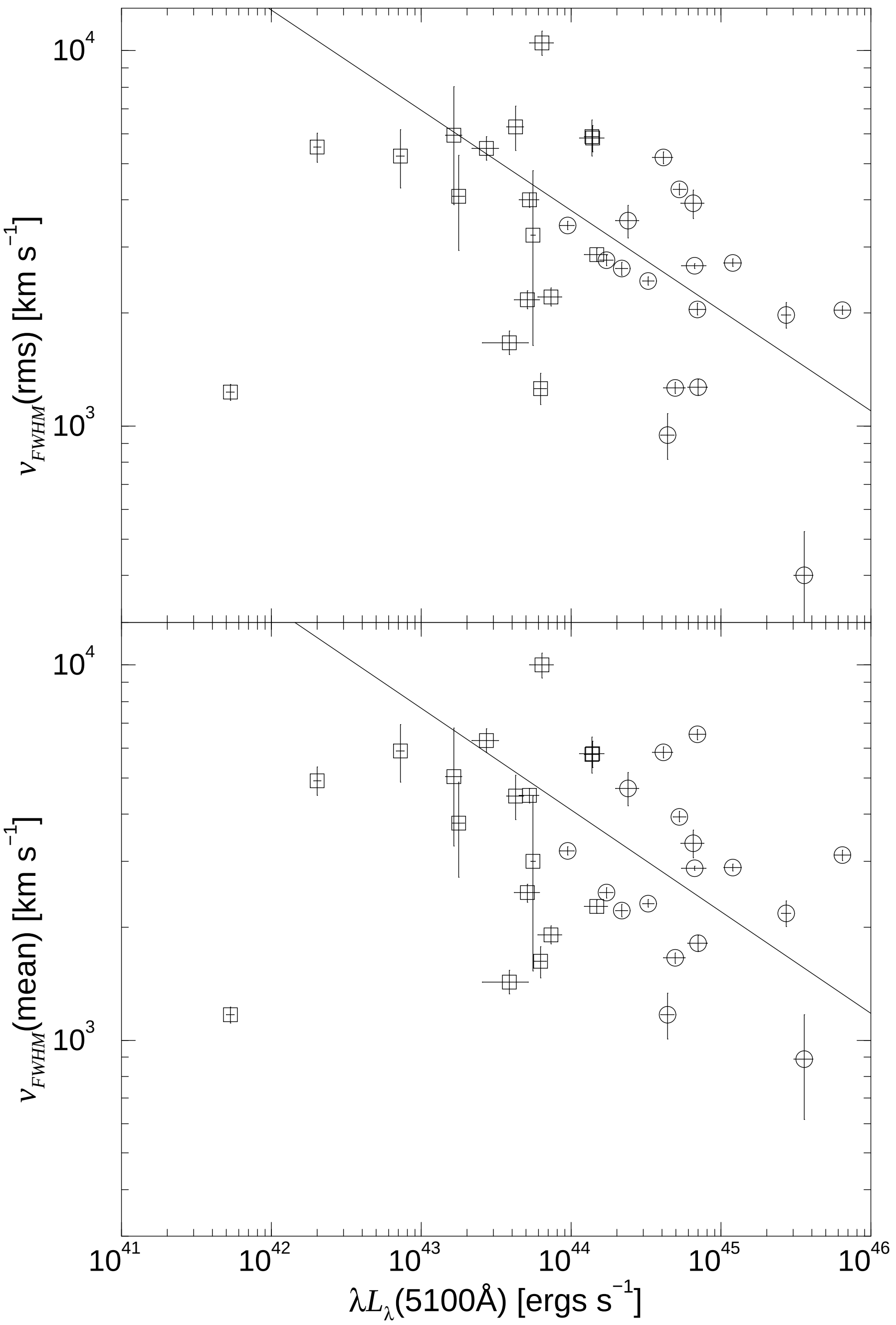

Fig. 4.3.— FWHM—luminosity relations. Top: FWHM derived from the rms spectrum of each object. Bottom: FWHM derived from averaging the FWHMs in all spectra for a given object. PG quasars are marked with circles and Seyfert 1s are marked with squares. Solid lines are the best fit to the data after excluding the outlier at the lowest luminosity (NGC 4051).

averages both Hα and Hβ. The PG quasars' v_{FWHM} found in this study agrees with the ones found by Boroson & Green's (1992) to within $\sim$10%, except for two objects (PG 1351 and PG 1704) for which we measure significantly narrower lines. If we exclude those two objects, the anticorrelation becomes weaker and its significance decreases. As the correlation we find is opposite to those found by previous studies, the issue of the velocity–luminosity relation needs further investigation, which is beyond the scope of this paper.

4.7 Mass—Luminosity Relation

Our two velocity estimates produce two mass estimates for each object (see Table 4.1 and § 4.4). The mass estimate based on the velocity from the FWHM in the mean spectrum is plotted, versus luminosity, in the bottom panel of Fig. 4.4. The correlation coefficient is 0.646, and the significance level is 3.7×10^{-5}. A linear fit gives

$$M(mean) = \left(5.71^{+0.46}_{-0.37}\right) \times 10^{7} \left(\frac{\lambda L_{\lambda}(5100\mathring{A})}{10^{44}\, ergs\, s^{-1}}\right)^{0.545\pm0.036} M_{\odot} \quad (4.8)$$

which is plotted as a solid line on the diagram.

The mass estimate based on the velocity from the FWHM measured from the rms spectrum is plotted in the top panel of Fig. 4.4. The correlation coefficient is 0.473, and the significance level is 4.7×10^{-3}. A linear fit to this relation gives

$$M(rms) = \left(5.75^{+0.39}_{-0.36}\right) \times 10^{7} \left(\frac{\lambda L_{\lambda}(5100\mathring{A})}{10^{44}\, ergs\, s^{-1}}\right)^{0.402\pm0.034} M_{\odot} \quad (4.9)$$

which is again plotted as a solid line.

The results of the above two methods are not consistent. Moreover, while it is arguable that using the rms spectra to determine v is a better method (see previous discussion), the mass–luminosity correlation based on this measure is less significant. This can perhaps be attributed to the fact that the line fluxes in the rms spectra are weaker and hence the uncertainty in the corresponding FWHM larger.

We have found both the size (§ 4.5) and the velocity (§ 4.6) to correlate with the luminosity with an intrinsic scatter in the correlations. The fact that the scatter in the mass–luminosity relation is larger than that of the size–luminosity and velocity–luminosity relations suggests that luminosity, rather than mass, is the variable that mainly determines

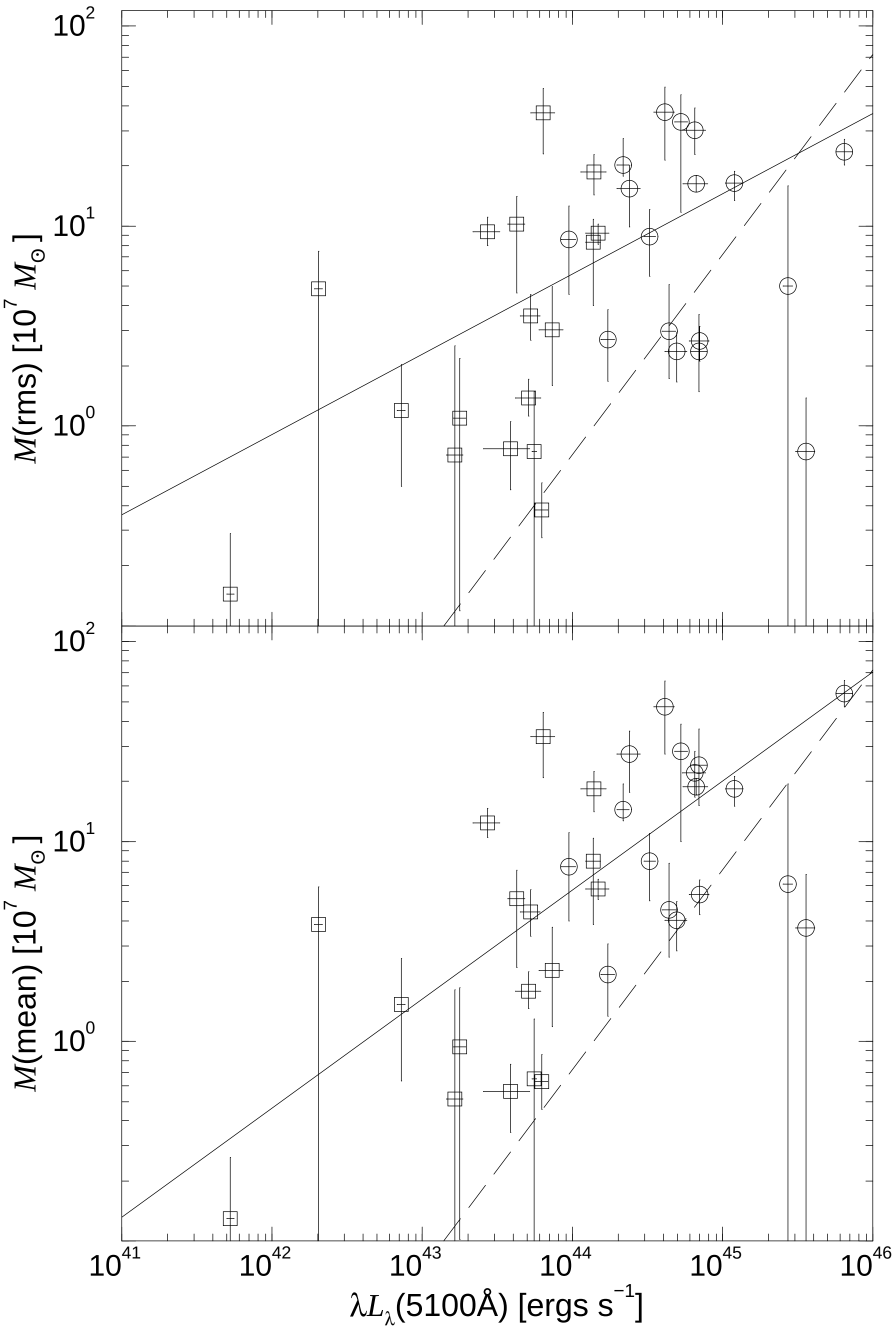

Fig. 4.4.— Mass—luminosity relations. Top: masses derived from v_{FWHM}(rms). Bottom: masses derived from v_{FWHM}(mean). PG quasars are marked with circles and Seyfert 1s are marked with squares. Solid lines are the best fit to the data. Dashed lines are the Eddington limit based on rough estimate for L_{bol} (see text).

the BLR size. In fact, from the individual size and velocity relations with respect to the luminosity we could expect: $M \propto v^2 R_{BLR} \propto (L^{-0.27})^2 L^{0.7} = L^{0.16}$, i.e., a very weak dependence of mass on luminosity, with all AGNs having similar masses. In practice, we have found a somewhat stronger dependence, $M \propto L^{0.5\pm0.1}$, but with a large scatter.

The relation we have found can be expressed in terms of the Eddington luminosity, L_{Edd}. Roughly estimating the bolometric luminosity as $L_{bol} \approx 9\lambda L_\lambda(5100\text{Å})$, we obtain

$$\frac{L_{bol}}{L_{Edd}} \approx 0.13 \left(\frac{\lambda L_\lambda(5100\mathring{A})}{10^{44}\, ergs\, s^{-1}}\right)^{0.5} \quad . \tag{4.10}$$

The Eddington limit, based on this rough estimate for L_{bol}, is plotted as a dashed line in Fig. 4.4. The most luminous quasars in our sample appear to be approximately at or beyond the Eddington limit.

In any case, the above mass–luminosity relation is not consistent with any model proposing that the bulk of the luminosity is due to energy release via a mechanism that radiates at a set fraction of the Eddington luminosity. One such model is a geometrically thin, optically thick, accretion disk, which requires $L/L_{Edd} \lesssim 0.3$ to be self-consistent (Laor & Netzer 1989). Our finding suggests that the mass accretion rate grows with luminosity much faster than the central mass, which would mean very different disk properties in low- and high-luminosity sources. We note, however, that our luminosity determination is based on the monochromatic flux at 5100 Å. In the thin disk model, this monochromatic flux may represents a different fraction of the object's bolometric luminosity in AGNs of different masses. Thus, the thin accretion disk model cannot be ruled out by the new results.

4.8 Summary

Spectrophotometric monitoring of a large, optically-selected, quasar sample has shown clear correlations and well defined time lags between the continuum and the Balmer-line light curves. While the Seyfert 1 galaxies that have been studied in this way in the past all have optical luminosities smaller than 1.5×10^{44} ergs s^{-1}, the new sample allows us to measure time lags in AGNs with luminosities up to 10^{46} ergs s^{-1}. Our work increases the available luminosity range for studying the size-mass-luminosity relations in AGNs by two orders of magnitude and doubles the number of objects suitable for such studies.

We have combined our results for 17 quasars with data for 17 Seyfert 1 galaxies having reliable time lag measurements, and produced a sample for which we uniformly estimated the sizes, masses, and luminosities.

Our main finding is that the BLR size scales with the 5100 Å luminosity as $L^{0.70\pm0.03}$. This is significantly different from Wandel et al.'s (1999) analysis and is also in contradiction with simple theoretical expectations, both suggesting $R_{BLR} \propto L^{0.5}$. We have also found that the velocity field of the BLR scales inversely with the luminosity, $v_{FWHM} \propto L^{-0.27\pm0.01}$. Combining the measured R_{BLR} with the observed FWHMs, we have obtained a mass-luminosity relation for AGNs, $M \propto L^{0.5\pm0.1}$, which, however, has a large intrinsic scatter.

The resulting M–L correlations based on two different methods of measuring the FWHM of the Balmer lines are not consistent with each other, despite the fact that the two measured values for the FWHM are generally consistent. Empirically, at least, it is not obvious which method of FWHM measurement is preferable.

Chapter 5

A New Approach to BLR Modeling

5.1 Introduction

In this chapter we investigate the physical conditions in the line emitting gas of a well studied AGN by incorporating modern photoionization calculations into a detailed geometrical model. Our new approach, that requires the simultaneous fit of several emission line light curves, enables us to constrain several important properties of the BLR, such as the gas density, column density and level of ionization. The model is rather complex and is, therefore, limited to a spherical BLR with no attempt to reconstruct the velocity field. In § 2 we present the model, in § 3 we apply it to the Seyfert 1 galaxy NGC 5548, and in § 4 we discuss the new results in view of past studies. A paper describing these results has been accepted for publication in *The Astrophysical Journal* (Kaspi & Netzer 1999).

5.2 The Model

5.2.1 Motivation, Choice of Target and Previous Work

Years of intensive AGN monitoring resulted in a wealth of information about the BLR response to continuum variations. Excellent data sets are now available for half a dozen sources and less complete sets on a dozen or so more. Unfortunately, theoretical understanding lags behind and there are few, if any, systematic attempts to produce complete models for the objects in questions. Most theoretical efforts have been limited to modeling of only one or two emission lines. They did not consider real limitations such as the gas density and column density. Our goal is to reconstruct *all the observed* light curves. This will enable us to set stringent limits on the physical parameters of the gas. More specifically, the aim is to deduce the run of density, column density and cloud distribution across the BLR. We will demonstrate that the time dependent relative and absolute line intensities, and their relationship to the continuum fluctuations, leave little freedom in such models. In particular, the density and column density are restricted to a rather limited range.

We wish to use as many observational constraints as possible and, therefore, limit ourselves to the best available data sets. We need both recombination lines, to constrain the covering factor, and collisionally excited lines to set limits on the run of density and temperature. Data sets including both high- and low-ionization lines are preferred since, in this way, we can set limits on the run of ionization parameter as a function of distance from the continuum source. Most importantly, we chose to rely as little as possible on Balmer line intensities since, as explained below, their calculated intensities are subjected to large theoretical uncertainties. Thus, the chosen data set must include a large enough number of UV lines and a well sampled, preferably large amplitude variable continuum. The only information that will not be used in this work is line profiles.

Given the above limitations, there are only 4 data sets that we consider suitable: 1. NGC 4151 - see Crenshaw et al. (1996) and references therein 2. NGC 5548 (Clavel et al. 1991) 3. NGC 3783 (Reichert et al. 1994) 4. NGC 7469 (Wanders et al. 1997). Out of those we chose to model the 1989 UV data of NGC 5548. This data set is unique in terms of its relatively large line and continuum variations, the *combination* of long duration with intensive regular 4-day sampling, and complete information on all strong UV lines (see however comments about Mg II λ2798 in § 5.4). Other advantages of this light curve are discussed below.

In modeling the gas distribution in the nucleus, we distinguish between direct and indirect methods. Direct methods are those where one guesses a gas distribution and calculates the resulting line light curves by putting, through this geometry, the observed (or deduced) continuum light curve. The result is compared with the observed emission-line light curves. Indirect methods attempt to obtain the gas distribution by computing transfer functions. This procedure is somewhat ill-defined since it produces responsivity maps, rather than mass-distribution maps. It therefore requires the additional confirmation that the so-obtained responsivity maps are consistent with photoionization calculations. There have been several attempts to produce transfer functions for various lines in NGC 5548, we are not aware of any successful mapping that is consistent with full photoionization calculations (see also Maoz 1994).

Several previous attempts to model the BLR in NGC 5548 differ from the present study in several important ways. The first systematic attempt to reconstruct the BLR is by Krolik et al. (1991). These authors used photoionization calculations to find the parameters that best fit the mean observed line ratios. In parallel, they have used the Maximum Entropy Method to reconstruct several transfer functions. Based on these transfer functions, they modeled a spherically symmetric BLR with locally isotropic line emitting clouds. The BLR is divided into two distinct zones: one emitting the high-ionization lines (column density of $\sim 10^{22}$ cm^{-2} and ionization parameter of 0.3) and the other emitting the low-ionization lines (column density of $\sim 10^{23}$ cm^{-2} and ionization parameter of 0.1).

O'Brien, Goad, & Gondhalekar (1994) have combined photoionization and reverberation-mapping calculations in a way similar to the present study (§ 5.2.2). Their work, and also the one by Pérez, Robinson & de la Funte (1992), focused on the shape of the transfer function and the line responsivity in a few generic models. They did not attempt a detailed reconstruction of a specific data set, and the comparison with the observations includes *only time lags*, and not the detailed shape of the light curves.

Shields, Ferland, & Peterson (1995) used photoionization calculations to examine the C IV λ1549/Lyα line ratio in NGC 5548 and other objects. They concluded that an optically thin non-variable component contributes to the BLR high ionization lines. Bottorff et al. (1997) presented a detailed kinematic model which they combined with photoionization calculations. They applied this model to *one emission line* (C IV λ1549) in the spectrum of NGC 5548.

Dumont, Collin-Souffrin, & Nazarova, (1998) modeled the BLR in NGC 5548 as a three-zone region in which the location of the various components were determined by the *mean* line-to-continuum lags. These authors assumed high column density ($\geq 10^{23}$ cm^{-2}) and photon density (the ionization parameter multiplied by the hydrogen density gives 10^9 to 10^{10} cm^{-3}). Much of their conclusion regarding the density and column density is based on the relative strength of the Balmer lines which we consider to be unreliable for reasons we describe below. Like most others, they did not compare the observed shape of the emission line light curves with the prediction of the model.

Finally, in a recent work, Goad and Koratkar (1998) re-examined the 1989 NGC 5548 data set and deduced a strong radial dependence for the gas density ($N \propto r^{-2}$, with density in the range of $10^{11.3} - 10^{10.0}$ cm^{-3}). Here again, the main assumption is of a two-zone model and there is no attempt to use the observed light curves, only the measured time lags.

Evidently, there is a definite lack of modeling complete data sets, i.e. the information provided by half a dozen emission line light curves. The published works focus on either detailed photoionization calculations or detailed geometrical modeling (i.e. using transfer functions) and no study has combined the two in a satisfactory way. Thus, no previous work has demonstrated that the assumed gas distribution, and the calculated physical conditions, are indeed compatible. Global consistency checks are certainly required.

Our work relies heavily on the direct approach. We prefer to avoid, as much as possible, ill-defined transfer functions and unreliable mass distributions. Instead we make a large number of initial assumptions ("guesses") and check them, one by one, against the complete data set of NGC 5548. This makes the numerical procedure more time-consuming but is more robust because of the direct relationship between the assumed geometry and the resulting light-curves. It also allows us to assess, in a more meaningful way, the statistical significance of our results.

5.2.2 Formalism

We follow the approach described by Netzer (1990) for a BLR consisting of numerous small clouds and a point-like ionizing source. The contribution of each cloud to the various emission lines is determined by the physical conditions within the cloud and its distance from the center. The main assumption is that the cloud pressure is controlled by an external medium (magnetic field, hot gas, etc.) whose pressure is a simple function of the radius, $P \propto r^{-s}$. For completeness, below we summarize the main ingredients of the model.

Consider a spherical system of clouds around a central radiation source and assume pure radial dependence of all properties. The hydrogen number density, $N(r)$, assumed to be constant within each cloud, is controlled by equilibrium with the external pressure. Neglecting the small electron temperature variation we take this to be

$$N(r) \propto r^{-s} \quad . \tag{5.1}$$

Next, we define the cloud column density, N_{col}, by considering spherical clouds, of radius $R_c(r)$. The mass of the individual clouds is conserved, as they move in or out, but it is not necessarily the same for all clouds, thus, $R_c^3(r)N(r) = const.$ The cloud mean (over the sphere) column density is thus

$$N_{col}(r) \propto R_c(r)N(r) \propto r^{-2/3s} \quad , \tag{5.2}$$

and the geometrical cross-section is

$$A_c(r) \propto R_c^2(r) \propto r^{2/3s} \quad . \tag{5.3}$$

(Note that the mass conservation assumption is only essential if we are to avoid an additional free parameter that specifies the run of N_{col} with distance). Finally, the number of clouds per unit volume is

$$n_c(r) \propto r^{-p} \quad . \tag{5.4}$$

In the numerical integration we consider only one type of clouds (i.e., same size at the same r for all clouds). Simple generalization of this scheme can involve a local population of clouds having some size distribution and the same p for all sub-classes. This requires extra normalization (see below) which we decided to avoid at this stage.

The clouds are illuminated by a central source whose ionizing luminosity, $L(t)$, varies in time. Designating $\epsilon_l(r, L)$ as the flux emitted by the cloud in a certain emission-line, l, per unit projected surface area ($erg\ s^{-1}\ cm^{-2}$), we get the following relation for the emission of a single cloud:

$$j_{c,l}(r, L) = A_c(r)\epsilon_l(r, L) \quad . \tag{5.5}$$

(where we note that in the actual calculations, we use a thin-slab geometry and hence the geometrical cross section is somewhat different from πR_c^2). Assuming that the system of clouds extends from r_{in} to r_{out} we obtain cumulative line fluxes

$$E_l \propto \int_{r_{in}}^{r_{out}} n_c(r) j_{c,l}(r, L) r^2 dr \quad . \tag{5.6}$$

Having determined the properties of the emission line clouds, and having assumed a spectral energy distribution (SED) for the ionizing source, we now calculate $\epsilon_l(r, L)$ using a photoionization code. We then follow the above formalism to obtain E_l. Since all parameters have been fixed, there is no need to independently specify the ionization parameter, $U(r)$ which, in our model, is given by

$$U(r) = \frac{Q}{4\pi r^2 N(r) c} \propto r^{s-2} \tag{5.7}$$

where Q is the number of hydrogen ionizing photons per second, and c is the speed of light.

AGN emission is variable, causing the local emission-line flux to be a function of time. We take this into account by calculating $\epsilon_l(r, L(t))$ for the entire range of continuum luminosity applicable to the source under discussion. The calculated *in situ* line fluxes are, therefore, the result of integrating Eq. 5.6, using, at each distance r the ionizing flux obtained with the ionizing luminosity $L(t - r/c)$. Observed fluxes further require the accounting for the light travel time between the cloud and the observer.

A model is specified by the source luminosity and SED, the radial parameter s, and the normalization of the various free parameters. These include r_{in}, r_{out} and the density and column density at a fiducial distance which we take to be 1 lt-day, i.e. outside the range of interest (in all the cases presented here $r_{in} > 1$ lt-day). The comparison with observations further requires the normalization of the total line fluxes and hence the integrated number of clouds. We prefer to use the total covering factor $C(r_{out})$ which is obtained by integrating

$$dC(r) = A_c(r) n_c(r) dr \propto r^{2/3s-p} dr \tag{5.8}$$

between r_{in} and r_{out}. The normalization of $C(r_{out})$ is achieved by comparing the observed and calculated flux of the emission lines. The numbers quoted below refer to the total covering factor as determined by taking the mean covering factor derived for the individual lines. We do not consider cloud obscuration and the calculations are limited to values of $C(r_{out})$ smaller than about 0.3. Considering all this, the total number of free parameters in the model is seven.

Computing a single model is not a trivial task. The reason is that, as explained, $\epsilon_l(r, L(t))$ is a function of both distance and time. We have accomplished this by calculating large grids of photoionization models covering the required range of density, column density, and incident flux. The calculations were performed using ION97, the 1997 version of the code ION (see Netzer 1996, and references therein). The code includes a large number of atomic transitions and solves for the level of ionization, and the gas temperature, at each location, taking into account all optical depth effects. The line and continuum transfer is calculated by using the local escape probability formalism. The cloud geometry assumed is of a thin shell. This is somewhat different from the spherical-cloud assumption made here, but the uncertainty introduced is well below the uncertainty of the escape probability method.

A serious problem in ION, and in similar codes like CLOUDY by G. Ferland (Ferland et al. 1998), is the treatment of the optically thick Balmer lines. The local escape probability approximation used in such codes is inadequate for these lines (Netzer 1990). Unfortunately, there is no known cure for this problem within that formalism and we have decided, therefore, not to consider Blamer lines in this work. The calculated intensity of other optically thick lines produced in the large, extended, low ionization zone of the cloud (e.g., Mg II λ2798 and many FeII lines) is also considered uncertain. A further limitation is the anisotropy of line emission which can be important when emission line light-curves are concerned (see Ferland et al. 1992 and references therein). We have decided not to include this effect since the local escape probability method cannot accurately take it into account and since it depends on the cloud shape, which is unknown. We caution that while codes like ION and CLOUDY calculate this anisotropy as part of their standard output, the fundamental limitation of the local escape probability method makes such numbers highly uncertain.

We have adopted a goodness of fit criteria to evaluate the model results. This is based on a simple χ^2 score which is evaluated by comparing the observed and theoretical light cures of *all* chosen emission lines, giving each line an equal weight. Thus, an acceptable model must reproduce the correct line variability as well as the observed line ratios. To the best of our knowledge, no previous AGN model have posed such stringent conditions on the goodness of fit.

5.3 Modeling the BLR in NGC 5548

The Seyfert 1 galaxy NGC 5548 is a subject of an intensive study for more then a decade now. This includes optical spectroscopic monitoring for 8 years (Peterson et al. 1999, and references therein), several satellite monitoring campaigns in different wavelengths — each with a duration of several months (e.g., Nandra et al. 1993, Korista et al. 1995, Tagliaferri et al. 1996, Marshal et al. 1997), and many complementary studies of those data sets (e.g., Clavel et al. 1992, Maoz et al. 1993, Wanders & Peterson 1996). This, together with the reasons mentioned in § 5.2.1, makes NGC 5548 the best object for testing our model. In this study we have concentrated on the 1989 *International Ultraviolet Explorer* (*IUE*) campaign (Clavel et al. 1991) and used the λ1337 continuum and five emission lines; Ly$\alpha\lambda$1216, C IV λ1549, C III] λ1909, He II λ1640, and Mg II λ2798.

On top of the general considerations described in the previous section, there are several constraints pertaining to NGC 5548:

1. The 1989 *IUE* spectra, and the following HST observations (Korista et al. 1995), clearly show that the C III] λ1909 line is blended with Si III] λ1895. Clavel et al. (1991) have measured the combined flux of both lines, without deblending (this is the flux listed in their tables under the C III] λ1909 header). This is also the case in the Korista et al. (1995) paper. The observed ratio of C III] λ1909 to Si III] λ1895 in the mean spectrum of NGC 5548, is about 3:1. The line ratio, which is density dependent, provides an important constraint on the density. We calculate the intensities of the silicon and carbon lines and restrict ourselves to those models producing a ratio consistent with the observations. The diagrams below gives the summed intensity under the title C III] λ1909.

2. Galactic and intrinsic reddening can affect the observed line ratios and the assumed ionizing continuum. We address this in § 5.3.4.

3. Another important consideration is the shape of the ionizing continuum. The observed SED of NGC 5548 is reviewed by Dumont et al. (1998) who discuss also various SEDs assumed in previous works. We have chosen a range of possible SEDs, all in agreement with observations of typical Seyfert 1 galaxies. Our optical-UV

continuum is combined with the observed ASCA continuum of the source assuming α_{ox}=1.06 (see George et al. 1998 for a discussion of the X-ray spectrum of NGC 5548). We have varied the assumed SED, as described in § 5.3.5, and tested the effect on the emission line spectrum. All chosen SEDs are rather similar to the ones discussed in Dumont et al. (1998). Our fiducial case is presented in Fig. 5.1 on the same scale as in Dumont et al. (1998).

4. Using the observed λ1337 continuum flux, a chosen cosmology (H_0=75 km s^{-1}Mpc^{-1} and $q_0 = 0.5$), and the assumed SED, we have estimated the time averaged ionizing luminosity of NGC 5548 to be $\sim 10^{44}$ erg s^{-1}. The continuum flux at λ1337 varied by a factor of ~ 4.5, during the *IUE* campaign. Hence we choose our grid to cover the ionizing luminosity range of $10^{43.6}$ to $10^{44.3}$ erg s^{-1}, with a step size corresponding to 0.1 in $\log L$. The observed λ1337 light curve was transformed into ionizing-luminosity light curve covering the entire range between these values - see Fig. 5.2. Considering the BLR geometry, we have defined our grid of distances to cover the range of 1 to 100 lt-days, with a step size of 0.02 in $\log r$.

5. We have adopted solar abundances for our standard model (see also § 5.3.2 below).

Model calculation proceed in two stages. First we produce two-dimensional grids of $\epsilon_l(r, L(t))$ by calculating, for each radial distance, all line emissivities for all ionizing luminosities. Each grid represents a particular choice of the density parameter s, and the density and column density at the fiducial distance. We consider three density laws: $s = 1$, 1.5, and 2, a density at 1 lt-day of $\sim 10^{11}$ to $\sim 10^{13}$ (varying by a factor of $\sim$2 from one grid to the next) and column densities at 1 lt-day of 10^{22}, 10^{23}, and 10^{24}. The choice of density, column density, s and the time-variable luminosity, completely specify the ionization parameter at each location.

In the second stage we calculate theoretical light curves by integrating Eq. 5.6. For this we need to define p, r_{in} and r_{out}. We have considered models with $p = 1$, 1.5 and 2. For each of these we have varied r_{in} and r_{out} in order to minimize the calculated χ^2.

An important consideration is the error bar size for the first few points. Obviously, we have no knowledge of the continuum behavior prior to the beginning of the campaign. We have therefore decided to extrapolated the continuum light curve, at a constant level,

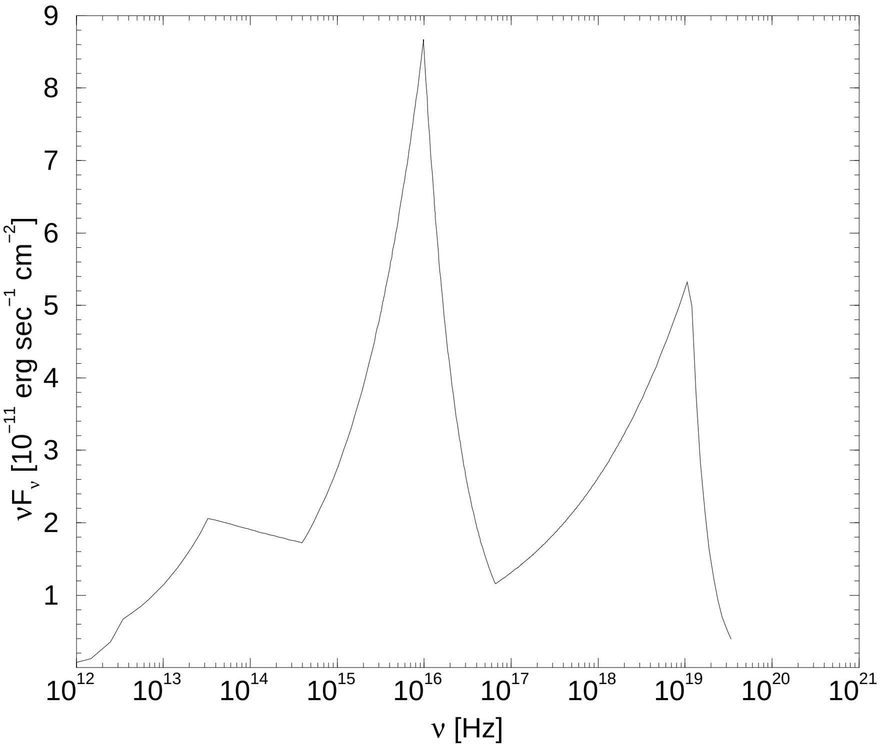

Fig. 5.1.— The spectral Energy Distribution of NGC 5548 used in this study. The continuum is normalized to agree with Dumont et al. (1998).

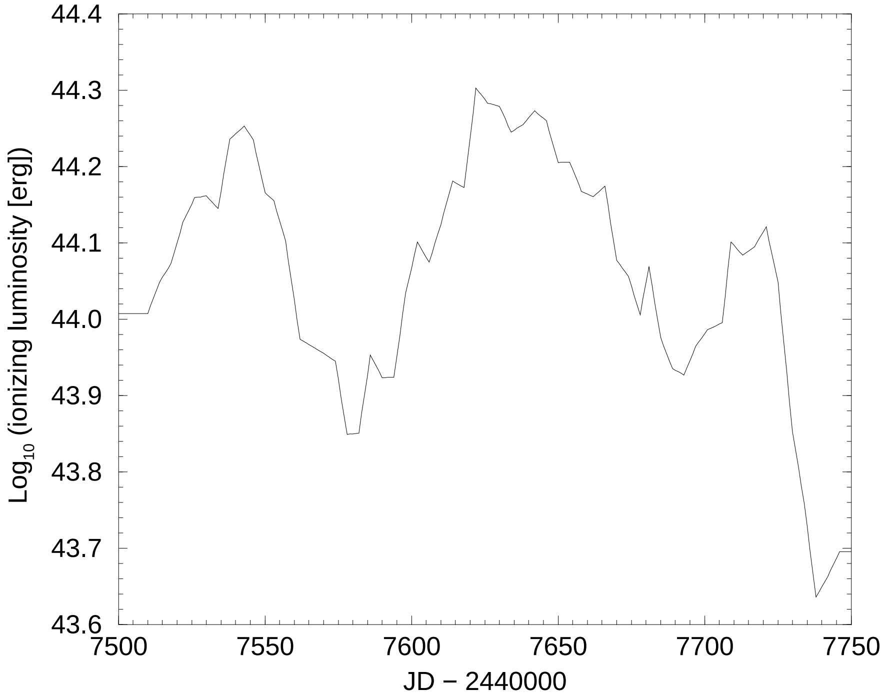

Fig. 5.2.— Interpolated ionizing continuum light curve based on the Clavel et al. (1991) continuum and our assumed SED.

for all JD $<$ 2447510. This lack of knowledge introduces a large uncertainty in the first part of the line light-curves which is likely to be much larger than the pure observational error. To partly cure this effect, we have artificially increased all experimental error bars during the first 100 days. We used a multiplication correction factor which is 3.0 for day 1 and decreases linearly with time, to 1.0, on day 100 (JD=2447600).

5.3.1 A Detailed Example, $s = 2$ Models

To illustrate our method, we present the results of a model with $s = 2$ (i.e. $N(r) \propto r^{-2}$ and $N_{col}(r) \propto r^{-4/3}$) , $p = 1.5$, $N_{col}(r = 1) = 10^{24}$ cm^{-2}, and various densities. We note, again, that what is referred to here as a *single model* covers, in fact, a large range of density and column density. Thus, choosing $N(r = 1) = 10^{12}$ cm^{-3} and $N_{col}(r = 1) = 10^{24}$ cm^{-2} we get at 10 lt-days, $N = 10^{10}$ cm^{-3} and $N_{col} = 10^{22.67}$ cm^{-2}, and at 100 lt-days, $N = 10^{8}$ cm^{-3} and $N_{col} = 10^{21.33}$ cm^{-2}.

Examining this case (Fig. 5.3) we note several obvious features. First, for $N(r = 1) \lesssim 10^{12.2}$ cm^{-3}, the emission line response is reversed, i.e., increasing continuum luminosity results in decreasing line luminosity. For example, while the ionizing luminosity is increasing from JD$\sim$2447600 to JD$\sim$2447650 (Fig. 5.2), the Lyα luminosity is decreasing (dotted line in Fig. 5.3), and the calculated light curve is a negative image of the observed one. Further demonstration of this effect is shown in Fig. 5.4: Here we plot the line emission per unit solid angle ($\epsilon_{Ly\alpha}(r, L)\times r^2$) versus r for four ionizing luminosities. For the lowest density $N(r = 1) = 10^{11.7}$ cm^{-3} (Fig. 5.4a) $\epsilon_{Ly\alpha}(r, L)\times r^2$ is larger for lower ionizing continuum for $r \gtrsim 5$ lt-days, i.e, the emitted Lyα is getting weaker when the ionizing luminosity is getting stronger. This effect is seen also in all other emission lines. The reason for this behavior is that for low density, the fast column density drop with distance causes the clouds to become optically thin a few lt-days away from the center. For lines other than Lyα, the increase in ionizing flux causes the gas to become too ionized to emit a significant amount in the line under question. The decrease in Lyα is of different origin. This line is mostly due to recombination and its intensity depends exponentially on the Lyman continuum optical depth (which, in this case, is of order unity) and linearly on the ionizing flux. Hence, the decrease in the optical depth affects the line more than the increase in ionizing flux. As evident from Figs. 5.3 and 5.4, the reversed response

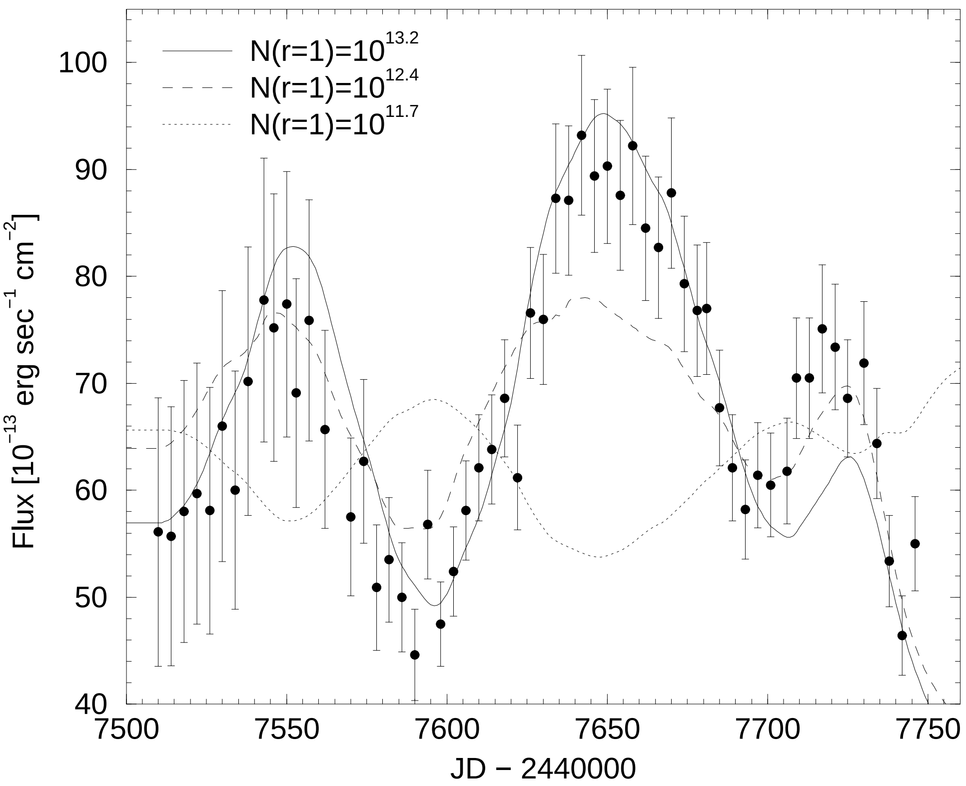

Fig. 5.3.— Calculated Lyα light curves for a model with $s = 2$, $r_{in} = 3$ lt-days, $r_{out} = 25$ lt-days $N_{col}(r = 1) = 10^{24}$, and various densities — $N(r = 1)$, as marked. Filled circles with error bars represent the observed light curve from Clavel et al. (1991).

disappears for $N(r = 1) \gtrsim 10^{12.2}$ cm^{-3}, resulting in a much better fit to the observations. This shows that careful analysis of a single light-curve is already enough to put limits on the BLR density.

While the simulated Lyα light curve, for the $s = 2$ grid, nicely fit the observed light curve with certain choice of density, r_{in} and r_{out}, this geometry seem to do a poorer job for the other emission lines. This is illustrated in Figs. 5.5 and 5.6 that show that while calculated light curves of Lyα, C IV and He II reasonably fit the observations, those for C III] and Mg II badly disagree with the data. Fig. 5.6 shows the reason for this discrepancy which is the positive response for Lyα, He II and C IV up to about a distance of 30 lt-days, and the negative response for Mg II and C III]. Furthermore, the apparent good fit shown by a solid line in Fig. 5.5 is misleading since it was obtained by allowing different normalizations of Eq. 5.6 for the different lines. When requiring the same covering factor for all lines, there is no satisfactory solution (see the dashed line in that diagram).

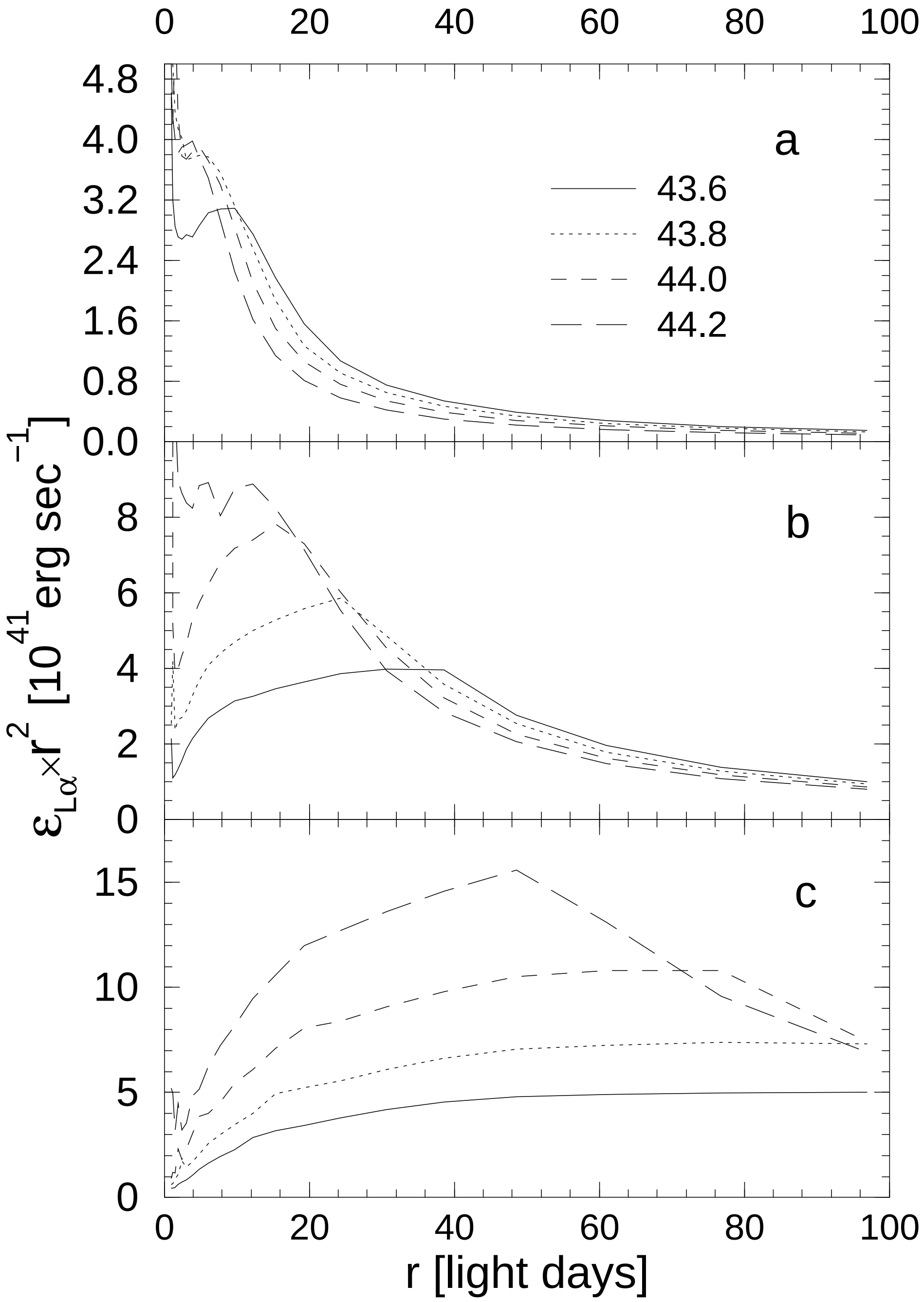

Fig. 5.4.— Lyα emission per unit solid angle versus r for the three densities shown in Fig. 5.3. a: $N(r=1) = 10^{11.7}$ cm^{-3}. b: $N(r=1) = 10^{12.4}$ cm^{-3}. c: $N(r=1) = 10^{13.2}$ cm^{-3}. For each model there are four different ionizing luminosities, as marked.

The disagreement amounts to a factor 1.4 for C III] and a factor 12(!) for Mg II. For that model (dashed line in Fig. 5.5) the reduced χ^2 score (for the 4 emission lines excluding the Mg II line as explained in § 5.3.2) is 9.8.

The above example demonstrates the difficulty in fitting, simultaneously, line responses and line ratios. Most previous work considered one line at a time and did not attempt full solution. Hence, their seemingly satisfactory solution does not represent realistic spectra. Our simulations show that no normalization or a choice of p can cure this problem in the $s = 2$ case. This is in contradiction to the result of Goad & Koratkar (1998) who favor an $s = 2$ BLR. (see further discussion of their model in § 5.4). The underlying reason for the failure of the $N \propto r^{-2}$ family of models is that, in such cases the ionization parameter is constant throughout the BLR. This is in contradiction to the observations that show different lags for lines representing different levels of ionization.

5.3.2 General Trends

We have made a careful investigation of a large number of models. We have considered cases with $s = 1$, 1.5, and 2, with $N(r = 1)$ in the range of 10^{11} to 10^{13} cm^{-3}, and three values of $N_{col}(r = 1)$, 10^{22}, 10^{23} and 10^{24} cm^{-2}. Below is a summary of the most important results.

We first note that as the column density increases from $N_{col}(r = 1) = 10^{22}$ to 10^{24} cm^{-2}, so does the agreement between the model and the data. Thus, models with $N_{col}(r = 1) = 10^{22}$ cm^{-2} give very poor fit (the line ratios are wrong and there is a reversed response in some lines) while models with $N_{col}(r = 1) \gtrsim 10^{23}$ cm^{-2} fit the data much better. Current photoionization codes are limited to Compton thin gas, i.e. they cannot reliably calculate cases with column densities larger than about 10^{25}. Thus we are unable to put upper limits on the column density of the gas.

While large column density clouds are not sensitive to the exact column, we have noted some changes that suggest that even the $N_{col}(r = 1) = 10^{23}$ cm^{-2} models are not thick enough. For example, in some models with this column there is a noticeable improvement in χ^2 when increasing the BLR size (i.e. r_{out}) which is not seen in the $N_{col}(r = 1) = 10^{24}$ cm^{-2} models. It indicates that the reversed response of optically thin cloud is present even in $N_{col}(r = 1) = 10^{23}$ cm^{-2} cases.

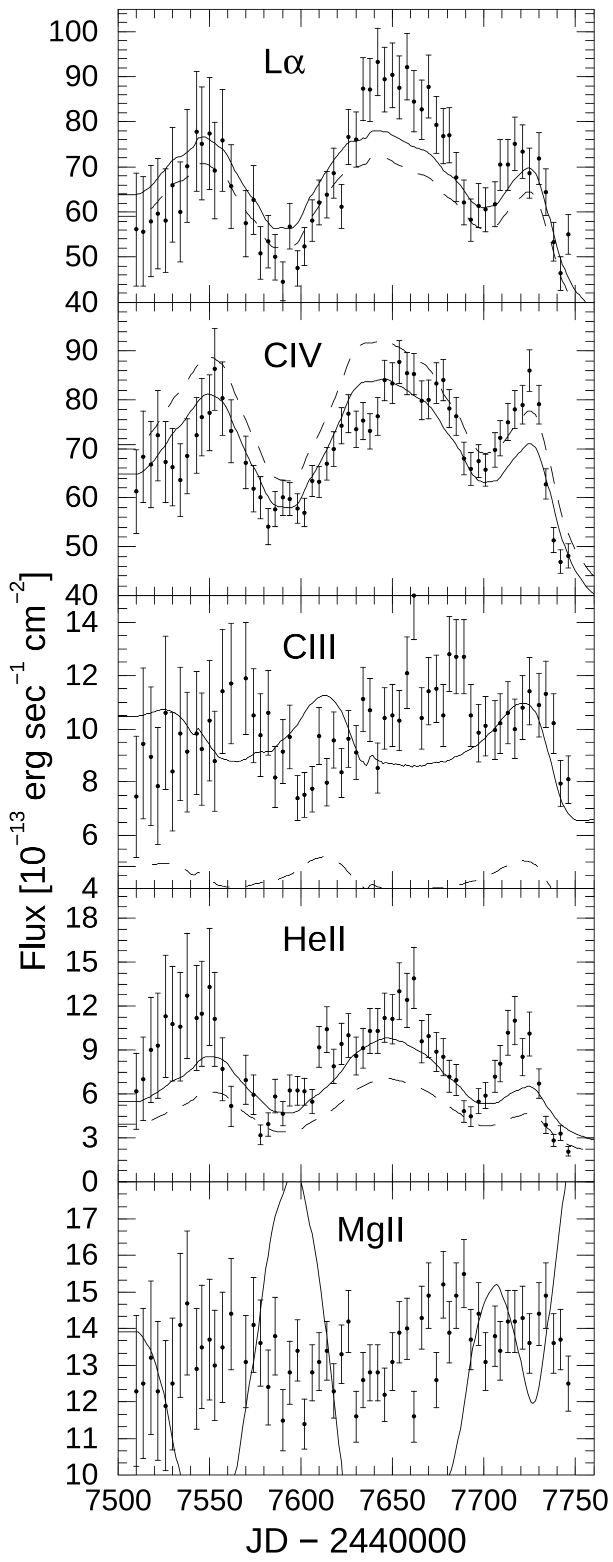

Fig. 5.5.— Simulated light-curves (curves) compared with observations for a model with $s = 2$, $p = 1.5$, $N(r = 1) = 10^{12.4}$ cm^{-3}, $N_{col}(r = 1) = 10^{24}$ cm^{-2}, $r_{in} = 3$ lt-days, and $r_{out} = 25$ lt-days. The solid lines represent models with different normalization factors for different lines. Dashed lines represent models where the same normalization factor is used for all lines (i.e. a single optimized covering factor).

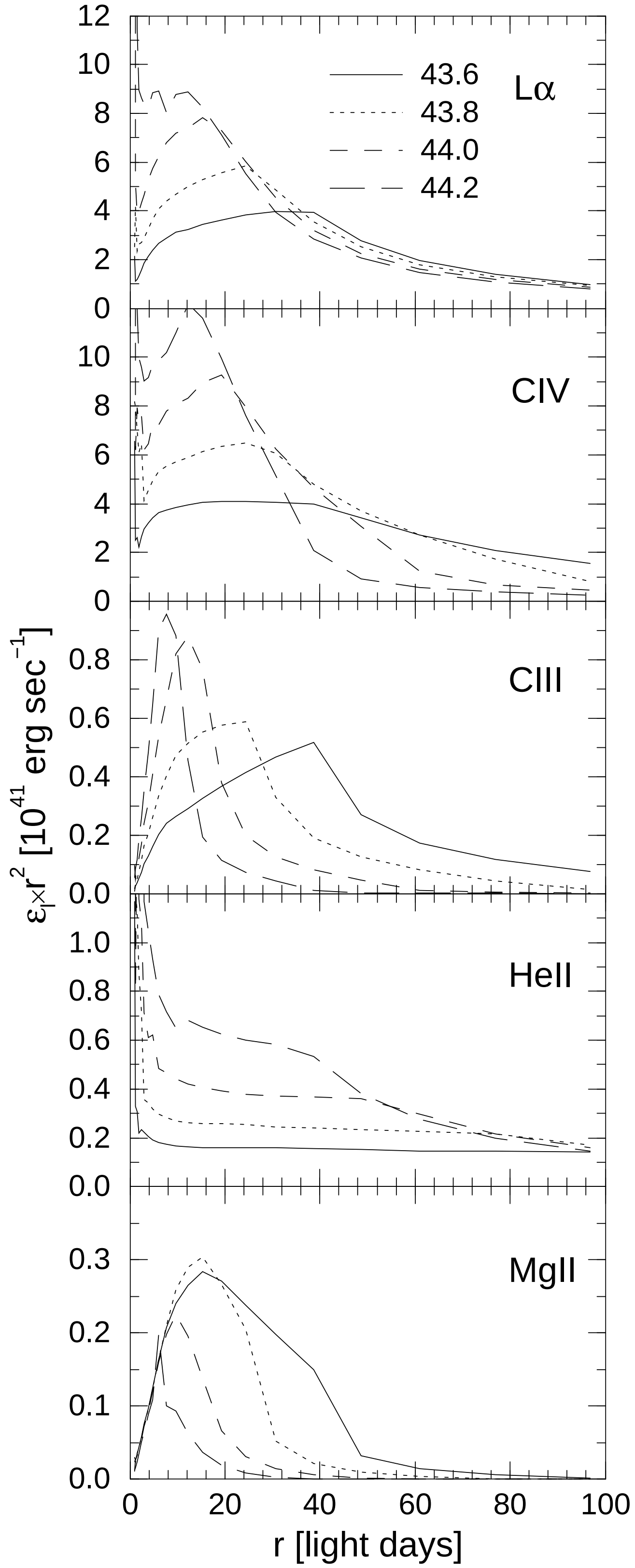

Fig. 5.6.— Line emission per unit solid angle versus r for the 5 emission lines modeled in Fig. 5.5.

As shown in § 5.3.1, $s = 2$ models are practically ruled out. Regarding cases with $s = 1.5$ and $s = 1$, we have found that in both cases there are lower and upper limits on the gas density. For $N(r = 1) \lesssim 10^{11}$ cm^{-3}, the $s = 1.5$ models result in reverse response (like the $s = 2$ models) and the $s = 1$ models produce wrong line ratios (in particular in these low density models the C III] λ1909 to Si III] λ1895 line ratio does not agree with the observations, see § 5.3). For $N(r = 1) \gtrsim 10^{12.5}$ cm^{-3}, the line ratios (e.g., He II /Lyα) in both s cases do not agree with the observations. Hence, our study shows that the BLR density in NGC 5548, is in the range of $10^{12.5} > N(r = 1) > 10^{11}$ cm^{-3}. This is true for all models with $N_{col}(r = 1) \gtrsim 10^{23}$ cm^{-2}.

A general trend found for all values of s is that as p increases from 1 to 2 (i.e., more weight is given to clouds closer to the central source) the amplitude of the modeled light curves is in better agreement with the observations and so are most line ratios (an exception is the Lyα/Mg II line ratio - see discussion below). Hence, models with higher p are preferred.

A common problem in all models is the too weak Mg IIλ2798 line. While we do not have a complete explanation for this, we suspect that it is due to one of two reasons: either the transfer of this line is inaccurately treated, similar to the case of the Balmer lines (discussed in § 5.2.2), or else it is caused by the thousands of highly broadened Fe II lines, in that part of the spectrum, that make the measured line intensity highly uncertain (see for example the discussion in Wills, Netzer and Wills, 1985; Maoz et al. 1993). Below we discuss the possibility of enhanced metallicity which also does not cure this problem. This is a definite failure of our model and is the reason for excluding this line when computing the χ^2 and the normalization factor for Eq. 5.6.

Another common trend is the improved χ^2 score for larger r_{out}. In general, models with r_{out} in the range 70 to 100 lt-day, agree better with the observations compared with models with $r_{out} < 70$ lt-days. We also found that the models are not very sensitive to the exact value of r_{in} and the best value is 3 lt-days.

Considering the above trends and limitations, and using the χ^2 score for the four chosen emission lines, we find that models with $s = 1$ best fit the observed spectra and models with $s = 1.5$ give somewhat inferior fits. An example of one of the best cases is a model with $s = 1$, $N_{col}(r = 1) = 10^{24}$ cm^{-2}, $N(r = 1) = 10^{11.4}$ cm^{-3}, $r_{in} = 3$ lt-days and $r_{out} = 100$ lt-days. The light curves produced in this case are shown in Fig. 5.7 for various values of p. The trend of improved fit with increasing p is evident for all lines except, as explained, for Mg II. The reduced χ^2 scores for the set of four emission lines are 4.5 for the $p = 1$ model, 3.1 for the $p = 1.5$ model, and 2.2 for the $p = 2$ model.

A note about the χ^2 score is in order. Our best models are characterized by $\chi^2 \sim 2$ which, statistically, is not very significant. This is somewhat arbitrary since enlarging the estimated errors by 50% (which can be attributed to to systematic measurement errors or model uncertainty) will result in $\chi^2 < 1$.

5.3.3 Different Composition

As noted earlier, almost all previous studies used solar composition material. In order to test the sensitivity of the results to the metal abundance, we ran our best fitted model (Fig. 5.7) with all metal abundances increased by a factor two. The results are generally similar to the solar composition model, with somewhat larger χ^2 score (slightly stronger C III] and slightly weaker Lyα and C IV). In view of this we have not investigated other compositions.

5.3.4 Reddening

Reddening can affect line ratios as well as the apparent shape of the continuum. Here we investigate the possibility that the intrinsic continuum differs, in luminosity and SED, from the observed one and the intrinsic line luminosities are larger than those observed. This would have an effect on the gas distribution in the source since the amount of continuum energy reprocessed by this gas, and the level of ionization, are different under these conditions.

Galactic reddening toward NGC 5548 is discussed by Wamsteker et al. (1990) who estimated it to be $E(B-V) = 0.05$. These authors noted the possibility of additional internal extinction which they have estimated to be of the same order of the galactic reddening. Following this, we have assumed an internal extinction identical to the galactic extinction, i.e., total extinction of $E(B-V) = 0.1$.

We have investigated the effect of reddening by modifying the SED in our best fit model (§ 5.3.2 as shown in Fig. 5.7) assuming the above $E(B-V)$. New line luminosities

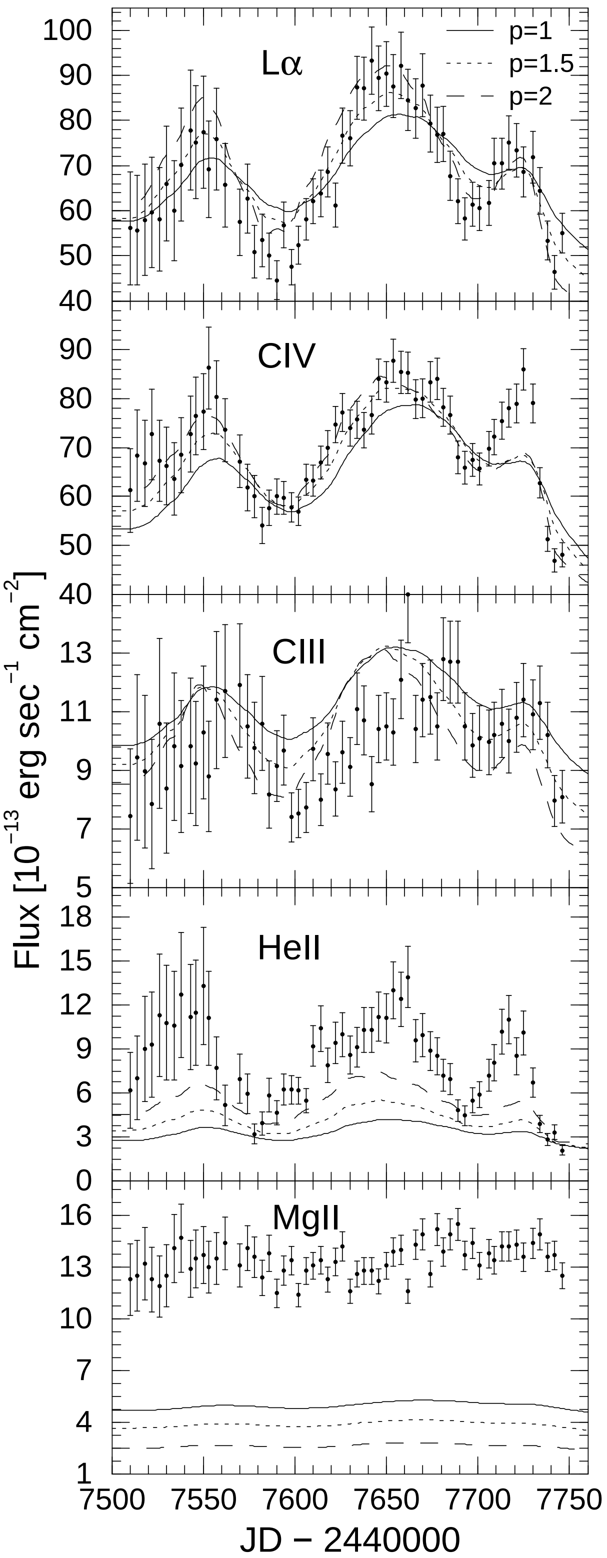

Fig. 5.7.— Simulated light-curves compared with observations for models with $s = 1$, $N(r = 1) = 10^{11.4}$ cm^{-3}, $N_{col}(r = 1) = 10^{24}$ cm^{-2}, $r_{in} = 3$ lt-days and $r_{out} = 100$ lt-days: solid line - $p = 1$; dotted line - $p = 1.5$; dashed line - $p = 2$. Note that $p = 2$ model is, by far, the best.

were obtained by using extinction correction factors from Seaton (1979). Dereddening the observed SED is more complicated since our adopted continuum is made of a collection of power-laws. The adopted SED is presented in Fig. 5.8e (dot-dashed line). It was normalized to fit the reddened $\lambda1337$ light curve, in order to be consistent with the observations (see explanation in § 5.3).

The results of this model are essentially identical to those of the unreddened case and are, therefore, not presented. This is not surprising in view of the further tests that we have conducted that are discussed below.

5.3.5 Different SED

Several theoretical ideas (e.g. Binette et al. 1989, Clavel & Santos-Lleo 1990) as well as observational evidence (e.g., Romano & Peterson 1999 and references therein) point to a change in the SED during continuum variation. This is expected since the shape of the optical-UV continuum is known to undergo large changes (e.g. Wamsteker et al. 1990, Clavel et al. 1991). Regarding the X-ray continuum variations, these are of a different time scale, and different amplitude, compared with the UV variations. It is therefore likely that the shape of the UV-X-ray ionizing continuum is a complicated function of the source luminosity. Unfortunately, there is little observational study of such changes and we can only estimate the effect by testing various possible SEDs and their effect on changes in the emission line spectrum.

We have carried out calculations with various possible schemes shown in Fig. 5.8. The first case (Fig. 5.8a) is the standard SED (the one used in all previous models, see Fig. 5.1 and solid line in Fig. 5.8e) shown here at 11 pre-chosen fluxes. Next we have tried different shape SEDs. In doing so we are not interested in the radio-FIR part of the continuum hence we did not alter the shape and level of the spectrum below a frequency of 0.01 Ryd. We also keep the flux above 20 Ryd constant since the *average* X-ray and γ-ray flux does not change on time scales similar to the optical–UV time scale (although it is changing very strongly on shorter time scales). Keeping in mind the observed variation in the optical-UV continuum slope, we assume that the flux change at 3 Ryd is a factor 2 larger than the flux change at 0.12 Ryd (the 0.12 and 3 Ryd are two of the energies used to define our SED). This is causing the optical-UV continuum to become harder as the

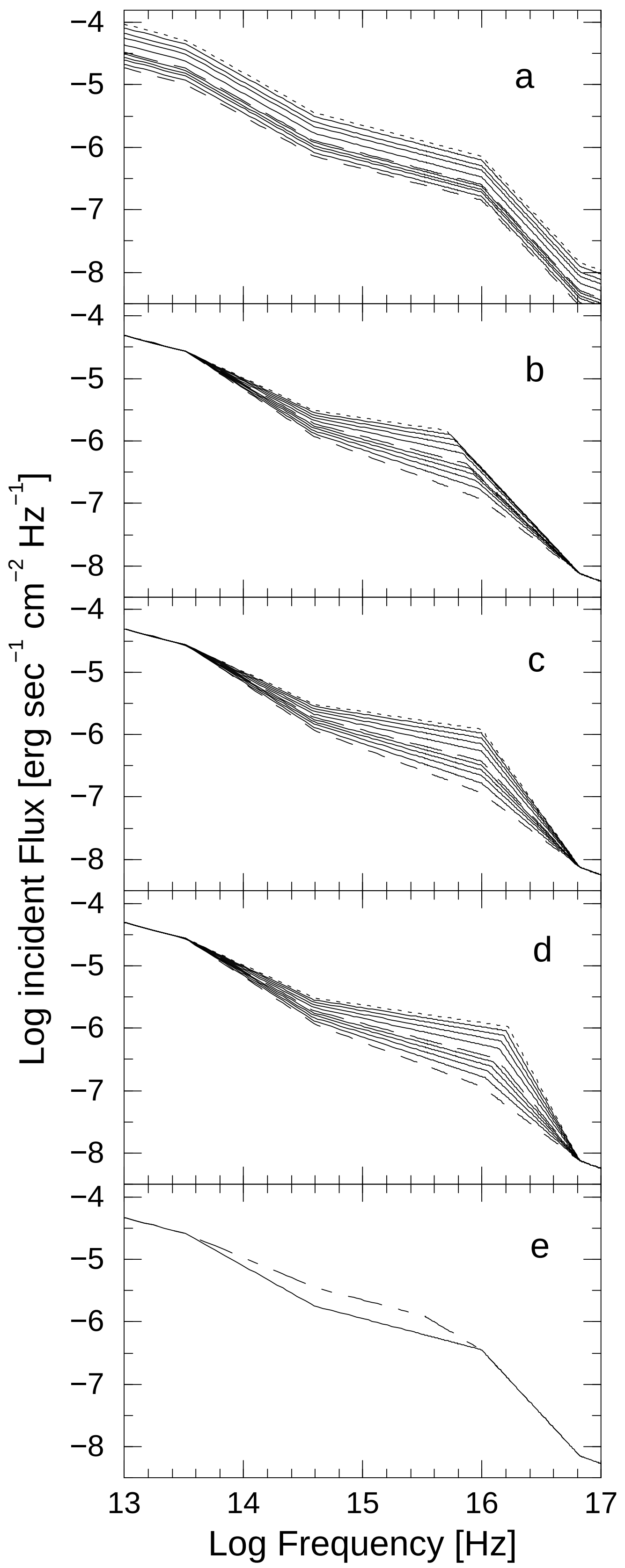

Fig. 5.8.— Different SEDs used in this work (see text for details). We show the SED illuminating a cloud positioned at $r = 10$ lt-days with $N = 10^{10.4}$ cm^{-3} and $N_{col} = 10^{23.3}$ cm^{-2}.

continuum luminosity increases and is consistent with observations (Clavel et al. 1991). We have normalized the SEDs such that the variable flux at 1337Å remains consistent with the observations. The different SEDs for this scheme are presented in Fig. 5.8c. We have used them to compute a new $\epsilon_l(r, L(t))$ grid for $s = 1$ model and to produce light curves for $p =$ 1,1.5 and 2. The agreement of these results with the observations is not as good as our best fit, constant shape SED model (§ 5.3.2 and Fig. 5.7) — the χ^2 score is about a factor 2 worse.

The reason for the inferior fit is related to the relative number of low and high energy ionizing photons. In particular, we attribute it to the relative number of ionizing photons above 4 Ryd. In our original model (Fig. 5.8a) the relative number of those photons is higher than in the variable SED model (Fig. 5.8c). To verify this, we have tested two other schemes. In the first scheme (Fig. 5.8b), as the continuum flux increases the break point at 3 Ryd moves, gradually, to *lower* frequencies (to 1.5 Ryd when the continuum flux is highest). Thus, there are even fewer ionizing photons above 4 Ryd compared with the scheme shown in Fig. 5.8b. Indeed, the resulting χ^2 score is much worse (by about a factor 3.5) compared with the constant SED scheme.

In the second scheme (Fig. 5.8d), the break point moves to *higher* frequencies as the continuum flux increases (from 3 Ryd when the flux is lowest to 5 Ryd when the flux is highest). The relative number of ionizing photons with energy larger than 4 Ryd increases with continuum luminosity. The resulting χ^2 is indeed better - see Fig. 5.9. In fact, the last scheme gives the very best fit of all our models, to the He II line light curve. However, the fits to the other lines (Lα, C IV , and C III]) are somewhat poorer and the overall χ^2 slightly worse (a factor 1.5) compared with the constant SED case.

The above examples show that our model results are, indeed sensitive to the assumed SED and its changes in time. Interestingly, the light curve fits point to a change which is opposite to the one suggested by Binette et al. (1989). We suspect that by scanning a large grid of parameters with such variable SED we can improve our best result. This is beyond of the scope of the present work.

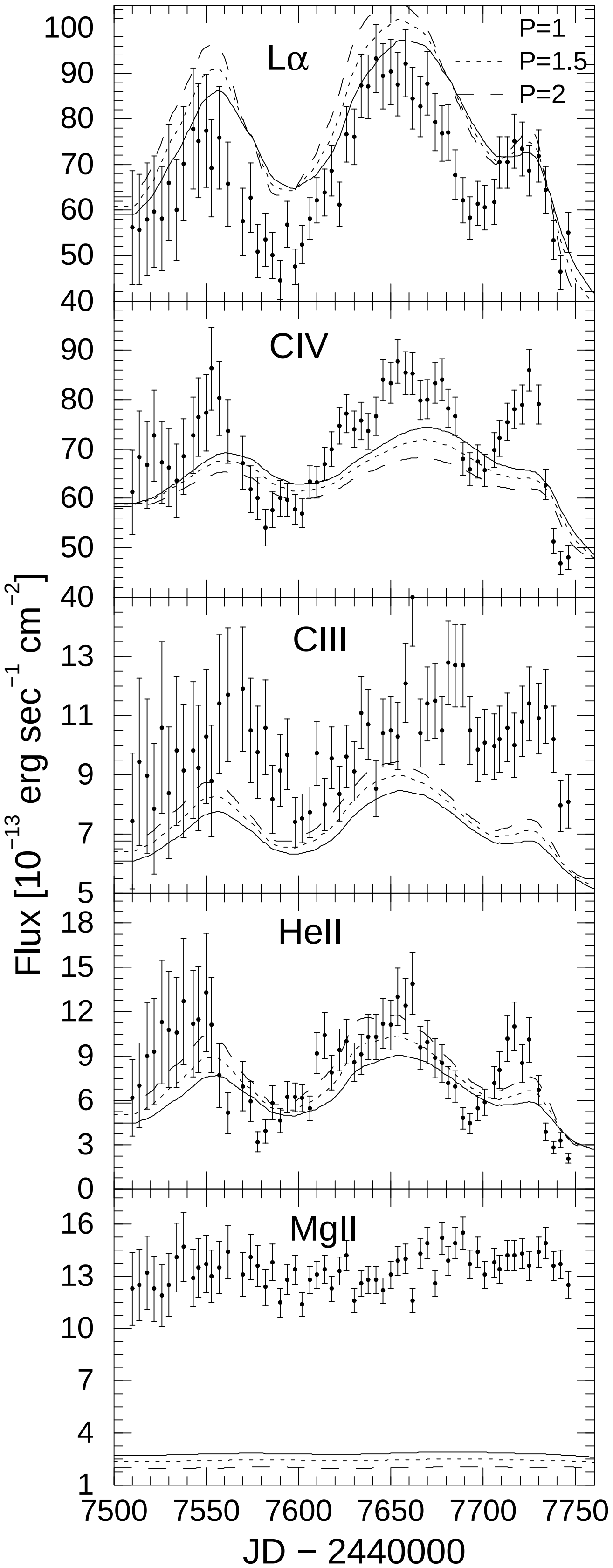

Fig. 5.9.— Same as Fig. 5.7 for a model with variable shape SED (Fig. 5.8d).

5.3.6 Covering Factor

We have computed the covering factor by integrating Eq. 5.8 as described in § 5.2.2. For models with $s = 2$ we find a covering factors between 0.5 (for $p = 2$) to 0.95 (for $p = 1$). This is much higher than predicted for typical AGNs but is in agreement with the results of Goad & Koratkar (1998) who find for their $N \propto r^{-2}$ model a covering factor of $\sim$0.7. As explained, fitting the light curves of several lines simultaneously, we can rule out models with $s = 2$. The too high covering factor seems to confirm our conclusion.

Models with $s = 1.5$ and $s = 1$ result in smaller covering factors. For our best model with $s = 1$ we find a covering factor of 0.25 for $p = 1$, 0.28 for $p = 1.5$, and 0.30 for $p = 2$. This is in good agreement with previous estimates and is consistent with the no-obscuration assumption of our model.

5.4 Discussion and Comparison With Other Studies

Several past models are detailed enough to allow meaningful comparison with our calculations.

1. Our models are inconsistent with the r^{-2} density law. This is in disagreement with the study of Goad and Koratkar (1998) despite of the good agreement with their range of acceptable densities and the lower limit on the column density. Goad and Koratkar (1998) did not explore a large parameter space, in particular, they only considered a limited range of density laws. We suspect that their conclusion regarding $s = 2$ models is related to the use of mean time lags, rather than detailed fits to the observed light curves.

2. Dumont et al. (1998) used a three zone model and reached several conclusions based on time-averaged properties. They noted three problems arising from their modeling: an energy budget problem, a line ratio problem, and line variability problem. The first two are most probably related to the use of Balmer line intensities as prime elements in evaluating their model results. As explained, we have not included the Balmer lines in our fit since we consider present day photoionization models to be inadequate in this respect. Regarding the line ratio, we find good agreement with observations for both high and low ionization lines. We suggest

that even a three-zone model, like the one used by Dumont et al., is too simplified to account for the continues gas distribution in NGC 5548.

3. "Locally Optimally-emitting Clouds" (LOCs) models (Baldwin et al. 1995, Korista et al. 1997) have been suggested to explain the broad line spectrum of AGNs. The models assume clouds with a range of density and column density at every point in the BLR. This is very different from our assumption of a specific density and column density at each radius. LOCs must be put into a real test by checking whether they result in light curves that are in better agreement with the observations, compared with the simpler models tested here.

   There are two obvious ways to compare the two models. First, in LOC models the incident central source flux "selects" clouds at certain radii to be efficient emitters of certain lines while at other radii, other lines are more efficiently produced. Thus, successful LOC models of NGC 5548 should resemble ours, in their run of density and column density for the most efficient emitting component. Second, future work along the lines suggested here should test multi-component models (i.e. various densities at each location) against the observed light-curve. This will make them similar, in some respect, to LOC models. Finally, we must comment that present day LOC models are too general and do not contain full treatment of shielding and mixing of the various coexisting components.

4. Alexander and Netzer (1994; 1997) suggested that BLR clouds may be bloated stars (BSs) with extended envelopes. In their work they fitted the emission-line intensities, profiles and variability to the mean observe AGN spectrum. One of the conclusions is that the density at the edge of the BSs (the part emitting the lines) falls off like $r^{-1.5}$, where r is the distance from the central source to the BS, and the number density of the BSs falls off like r^{-2}. These two trends are in good agreement with our preferred values of s and p. While the BS model is consistent with the mean time-lags measured in intermediate luminosity AGNs, it remains to be seen whether it can fit, in detail, the time dependent spectrum of objects like NGC 5548.

5.5 Summary

We have presented a new scheme to model the BLR in AGNs. It combines photoionization calculations with reverberation mapping and assumes gradual changes of density and column density as a function of distance from the central source. Using this scheme we were able to constrain the physical conditions in the BLR and put limits on the important physical parameters. The present work addresses only spherical BLRs. Future work will hopefully generalize it to other geometries.

When applying the scheme to NGC 5548, we were able to reconstruct four out of the five observed UV emission-line light curves. We found that a large population of optically thin-clouds (due to low density and/or column density) results in a reversed response to continuum variations. Such models are therefore excluded. We also excluded models where $N \propto r^{-2}$ and favor models where the density scales as $r^{-1.5}$ or r^{-1}. We have placed a lower limit of $N_{col}(r=1) \gtrsim 10^{23}$ cm^{-2} on the column density of the clouds. We have used the results to place limits on the density of the BLR. For NGC 5548, this must be in the range of $10^{12.5} > N(r=1) > 10^{11}$ cm^{-3}.

We have studied a range of possible SEDs, including one which resulted from applying a reddening correction with $E(B-V)$=0.1. The one that produces the best agreement with the observations is an SED where the relative number of $E > 4$ Ryd photons increases with the AGN luminosity.

Chapter 6

Summary and Suggestions for Future Work

The first part of this thesis presented the results of an intensive optical spectrophotometric monitoring of the Seyfert galaxy NGC 4151. This campaign, in 1993, lasted for two months and had a typical temporal resolution of one day. This is the first ever optical reverberation mapping campaign with such a dense sampling for such a long period. The variations of the various optical continuum bands were between 17% and 35%, with decreasing amplitude towards longer wavelengths. The continuum bands were found to vary in phase, with a lag of < 1 day. The broad Hα line flux varied by $\sim 12\%$ and the broad Hβ flux by $\sim 30\%$. The Hα and Hβ light curves follow the continuum variations with a lag of $0-3$ days, in contrast to previous results where a time lag of 9 ± 2 days was found. This may be related to a different variability timescale of the *ionizing* continuum, or to a real change in the BLR gas distribution during the 5.5 years interval between the two campaigns.

The main part of this thesis presented spectrophotometric results for a large, optically-selected, quasar sample. The observations lasted for 7.5 years, with typical temporal sampling of a few months. This is the longest and most successful quasar reverberation mapping campaign, so far. It is also the first study to show clear correlations and well defined time lags between the continuum and the Balmer-line light curves in quasars. While the Seyfert 1 galaxies that have been studied in this way in the past all have optical luminosities smaller than 1.5×10^{44} ergs s^{-1}, the new sample allowed us to measure time lags in AGNs with luminosities up to 10^{46} ergs s^{-1}. Our work increased the available luminosity range for studying the size-mass-luminosity relations in AGNs by two orders of magnitude and *doubled* the number of objects suitable for such studies. Using new techniques, we were able to determine the time lags for 17 out of 28 objects in the sample.

We have combined our results with data for 17 Seyfert 1 galaxies having reliable time lag measurements to produce a sample of 34 AGNs for which we uniformly estimated the size, mass, and luminosity. Our main finding is that the BLR size, R_{BLR} scales with the 5100 Å luminosity as $L^{0.70\pm0.03}$. This is significantly different from earlier findings and is also in contradiction with simple theoretical expectations, both suggesting $R_{BLR} \propto L^{0.5}$. We have also found that the velocity field of the BLR scales inversely with the luminosity, $v_{FWHM} \propto L^{-0.27\pm0.01}$. Combining the measured R_{BLR} with the observed FWHMs, we have obtained a mass-luminosity relation for AGNs, $M \propto L^{0.5\pm0.1}$, which, however, has a large intrinsic scatter.

In the last part of the thesis we presented a new scheme for BLR modeling. The scheme combines photoionization calculations with reverberation mapping. The model assumes a change of density and column density as a function of distance from the central source, and allows different radial dependences. We tested the model on NGC 5548 and were able to reconstruct four out of the five observed UV emission-line light curves. We excluded models where $N \propto r^{-2}$ and favor models where the density scales as $r^{-1.5}$ or r^{-1}. We also placed a lower limit of $N_{col}(r=1) \gtrsim 10^{23}$ cm^{-2} on the column density of the clouds and limited their density to be in the range of $10^{12.5} > N(r=1) > 10^{11}$ cm^{-3}, at the fiducial distance of 1 lt-day.

It is important to continue testing and developing the above theoretical model. This includes the following suggestions:

A. There are excellent monitoring data sets for a few more objects (e.g., NGC 4151, NGC 3516, NGC 7469). The model will enable to put limits on the physical parameters of the BLRs in those objects.

B. The model has been tested only on spherical geometries. However, some studies suggest that the BLR has a different geometry, such as a disk or a bi-conical structure (e.g., Pérez et al. 1992). Testing such geometries will hopefully result in the most acceptable BLR geometry.

C. We need to add a velocity field to the model (Bottorff et al. 1997). This will enable testing several aspects of BLR dynamics.

D. Fine-tuning of the parameters used in the first version of the model is required. This includes changes in the SED and a range of density and column density at every location.

Our PG monitoring program showed the usefulness of long term monitoring of high luminosity AGNs. By now we have a sample of more then 30 AGNs with well determined size, mass and luminosity. However, there is a need to carry out a systematic comparison of the UV and X-ray properties of those sources. Such work will enable the study of the innermost region where the UV and X-ray continuum are thought to originate. An example can be seen in a recent work of Wandel & Boller (1998) who suggested a model connecting the BLR size and the X-ray radiation from the accretion disk. So far, the predictions of such models could only be tested on Seyfert galaxies. The current sample provides BLR size determinations in PG quasars, and will enable testing such a model over a much larger luminosity range.

The PG spectra we have obtained require more studying. We plan to measure and cross-correlate many continuum bands, from the shortest to the longest wavelength, in order to test for wavelength-dependent time lags. Recently, Collier et al. (1998) found continuum lags of $\sim$1 day in NGC 7469. For quasars such time lags should be of the order of few days or a week and hence might be found in a few of the best sampled quasars in our PG sample. This will have important implications to the structure of the continuum source. Studying the line profiles and their variations will probe the BLR dynamics. In particular, we plan to study the time lag between the flux in the blue and the red wings of the lines to test for outflow or inflow motions.

The PG quasars monitoring campaign has increased the luminosity range of objects with known time lags (and hence known BLR size) by two orders of magnitude. However, our PG sample is luminosity and redshift limited. In order to increase the luminosity range to above 10^{46} ergs s^{-1} we need to monitor high redshift quasars. We estimate that we will have to monitor such quasars once every few months ($\sim$3) which, on a medium size telescope, will require one or two nights each run. We expect first results within two to three years with full campaign that will last some 5 to 10 years. Having these results will enable us to test the emission line response to the continuum variation in the highest luminosity quasars. Such a future project will bring to completion the reverberation studies of all AGNs with luminosity in the range of 10^{41} to 10^{48} ergs s^{-1}.

References

Alexander, T. 1997, in Astronomical Time Series, ed. D. Maoz, A. Sternberg, & E. M. Leibowitz (Dordrecht: Kluwer), 163

Alexander, T., & Netzer, H. 1994, MNRAS, 270, 781

Alexander, T., & Netzer, H. 1997, MNRAS, 284, 967

Alloin, D., Clavel, J., Peterson, B. M., Reichert, G. A., & Stirpe, G. M., 1994, in Frontiers of Space and Ground-Based Astronomy, ed. W. Wamsteker, M. S. Longair, & Y. Kondo (Dordrecht: Kluwer), 423

Alloin, D., et al. 1995, A&A, 293, 293

Antonucci, R. R. J., & Cohen, R. D. 1983, ApJ, 271, 564

Antonucci, R. 1993, ARAA, 31, 473

Avrett,E. H., & Loeser, R. 1988, ApJ, 331, 211

Bahcall, J.N., Kozlovsky, B., and Salpeter, E.E., 1972, ApJ, 171, 467

Baldwin, J., Ferland, G., Korista, K., & Verner, D. 1995, ApJL, 455, L119

Baribaud, T., & Alloin, D. 1990, A&A, 236, 346

Berriman, G., Schmidt, G.D., West, S.C., and Stockman, H.S. 1990, ApJS, 74, 869

Binette, L., Prieto, A., Szusziewicz, E., & Zheng, W. 1989, ApJ, 343, 135

Blandford, R.D., 1990, in Active Galactic Nuclei, ed. Courvoisier, T.J.-L., and Mayor M. (Berlin: Springer-Verlag), 161

Blandford, R.D., & McKee, C.F., 1982, ApJ, 255, 419

Boroson, T. A., & Green, R. F. 1992, ApJS, 80, 109

Bottorff, M., Korista, K. T., Shlosman, I., & Blandford, D. R. 1997, ApJ, 479, 200

Boyle, B. J., Fong, R., Shanks, T., & Peterson, B. A. 1987, MNRAS, 231, 897

Clavel, J. & Santos-Lleo, M. 1990, A&A, 230, 3

Clavel, J., et al. 1990, MNRAS, 246, 668

Clavel, J., et al. 1991, ApJ, 366, 64

Clavel, J., et al. 1992, ApJ, 393, 113

Coleman, G. D., Wu, C. C., & Weedman, D. W. 1980, ApJS, 43, 393

Collin-Souffrin, S., & Dumont, A.-M. 1989, A&A, 166, 13

Collier, S., et al. 1998, ApJ, 500, 162

Courvoisier, T.J.-L., et al. 1990, A&A, 234, 73

Crenshaw, D. M., & Blackwell, J. H., Jr. 1990, ApJ, 358, L37

Crenshaw, D. M., et al. 1996, ApJ, 470, 322

Dietrich, M., et al. 1998, ApJS, 115, 185

Dumont, A. -M., Collin-Souffrin, S., & Nazarova, L. 1998, A&A, 331, 11

Edelson, R. A., & Krolik, J. H. 1988, ApJ, 333, 646

Edelson, R. A., et al. 1996, ApJ, 470, 364

Evans, I.N., et al. 1993, ApJ, 417, 82

Erkens, U., et al. 1995, A&A, 296, 90

Ferland, G. J., Korista, K. T., Verner, D. A., Ferguson, J. W., Kingdon, J. B. & Verner, E. M. 1998, PASP, 110, 761

Ferland, G. J., Peterson, B. M., Horne, K., Welsh, W. F., & Nahar, S. N. 1992, ApJ, 387, 95

Gaskell, C. M. 1994, in Reverberation Mapping of the Broad-Line Region in AGN, ed. P. M. Gondhalekar, K. Horne, & B. M. Peterson (San Francisco: ASP), 111

Gaskell, C. M., & Peterson, B. M., 1987, ApJS, 65, 1

Gaskell, C. M., & Sparke, L. S. 1986, ApJ, 305, 175

George, I. M., Turner, T. J., Netzer, H., Nandra, K., Mushotzky, R. F., & Yaqoob, T., 1998, ApJS, 114, 73

Gilbert, A. M., Eracleous, M., Filippenko, A. V., & Halpern, J. P. 1999, American Astronomical Society Meeting, 194, #73.02

Giveon U., Maoz, D., Kaspi, S., Netzer, H., & Smith, P. S. 1999, MNRAS, 306, 637 (Paper III)

Goad, M., & Koratkar, A. 1998, ApJ, 495, 718

Gondhalekar, D. M., et al. 1986, MNRAS, 222, 71

Gondhalekar D. M. 1990, MNRAS, 243 443

Hook, I. M., McMahon, R. G., Boyle, B. J., & Irwin, M. J. 1994, MNRAS, 268 305

Horne, K. 1994, in Reverberation Mapping of the Broad-Line Region in AGN, eds. P. M. Gondhalekar, K. Horne, & B. M. Peterson (San Francisco: ASP), 23

Horne, K. 1997, in Astronomical Time Series, eds., D. Maoz, A. Sternberg, and E. Leibowitz (Dordrecht: Kluwer), 109

Jackson, N., et al. 1992, A&A, 262, 17

Joly, M., Collin-Souffrin, S., Masnou, J. L., & Nottale, L. 1985, A&A 152, 282

Kaspi, S., & Netzer H. 1999, ApJ, in press

Kaspi, S., et al. 1996a, 470, 336

Kaspi, S., Ibbetson, P. A., Mashal, E., & Brosch, N. 1995, Wise Obs. Tech. Rep., No 6

Kaspi, S., Smith, P. S., Maoz, D., Netzer, H., Jannuzi, B. T. 1996, ApJ, 471, L75

Keel, W.C., and Allan, P.M., 1991, in Variability in AGNs, ed. H.R. Miller and P.J. Wiita, (Cambridge), 83

Kellermann, K. I., Sramek, R., Schmidt, M., Shaffer, D. B., Green, R. 1989, AJ, 98, 1195

Kinney, A. L., Calzetti, D., Bohlin, R. C., McQuade, K., Storchi-Bergmann T., & Schmitt, H. R. 1996, ApJ, 467, 38

Koratkar, A. P., & Gaskell, C. M. 1989, ApJ, 345, 637

Koratkar, A. P., & Gaskell, C. M. 1991, ApJS, 75, 719

Koratkar, A. P., Pian, E., Urry, C. M., & Pesce, J. E. 1998, ApJ, 492, 173

Korista, K. T. 1991, AJ, 102, 41

Korista, K. T. et al. 1995, ApJS, 97, 285

Korista, K. T., Baldwin, J., Ferland, G., & Verner, D. 1997, ApJS, 108, 401

Krolik, J. H., & Done, C. 1995, ApJ, 440, 166

Krolik, J. H., Horne. K., Kallman, T. R., Malkan, M. A., Edelson, R. A., and Kriss, G. A. 1991, ApJ, 371, 541

Laor, A, & Netzer, H. 1989, MNRAS, 238, 897

Laor A., Fiore, F., Elvis, M., Wilkes, B. J., & McDowell, J. C. 1997, ApJ, 477, 93

Lawrence, A., 1987, PASP, 99, 30

Leighly, K. M., et al. 1997, ApJ, 483, 767

Maoz, D. 1994, in Reverberation Mapping of the Broad-Line Region in AGN, ed. P. M. Gondhalekar, K. Horne, & B. M. Peterson (San Francisco: ASP), 95

Maoz, D. 1997, in Emission Lines in Active Galaxies: New Method and Techniques, ed. B. M. Peterson, F.-Z. Cheng, & A. S. Wilson (San Francisco: ASP), 138

Maoz, D. et al. 1993, ApJ, 404, 576

Maoz, D., Smith, P. S., Jannuzi, B. T., Kaspi, S., Netzer, H. 1994, ApJ, 421, 34

Maoz, D., & Netzer, H. 1989, MNRAS, 236, 21

Maoz, D., et al. 1990, ApJ, 351, 75

Maoz, D., et al. 1991, ApJ, 367, 493

Marshall, H. L., et al. 1997, ApJ, 479, 222

Miller, J. S., & Stone, R. P. S. 1993, Lick Obs. Tech. Rep., No 66

Nandra, K., et al. 1993, MNRAS, 260, 504

Nandra, K, Clavel, J., Edelson, R. A., George, I. M., Malkan, M. A., Mushotzky, R. F., Peterson, B. M., & Turner, T. J. 1998, 505, 594

Netzer, H. et al. 1990, ApJ, 353, 102

Netzer, H. et al. 1996, MNRAS, 279, 429

Netzer, H. 1990, in Active Galactic Nuclei, ed., T. J. -L. Courvoisier and M. Mayor (Berlin: Springer-Verlag), 57

Netzer, H. 1991, in Variability of Active Galaxies, ed. W. J., Duschl, S. J., Wagner, & M. Camenzind (Berlin: Springer-Verlag), 107

Netzer, H. 1996, ApJ, 473, 781

Netzer, H., & Maoz, D. 1990, ApJ, 365, L5

Netzer, H., & Peterson, B. M. 1997, in Astronomical Time Series, eds., D. Maoz, A. Sternberg, and E. Leibowitz (Dordrecht: Kluwer), 85

Neugebauer, G., Green, R.F., Matthews, K., Schmidt, M., Soifer, B.T., and Bennett, J., 1987, ApJS, 63, 615

O'Brien, P. T., Gondhalekar, P. M., & Wilson, R. 1988, MNRAS, 233, 801, 845

O'Brien, P. T., & Gondhalekar, P. M. 1991, MNRAS, 250, 377

O'Brien, P. T., & Harries, T. J. 1991, MNRAS, 250, 133

O'Brien, P. T., Goad, M. R., & Gondhalekar, P. M. 1994, MNRAS, 268, 845

O'Brien, P. T., et al. 1998, ApJ, 509, 163

Oknyanskij, V. L., Lyutyi, V. M, & Chuvaev, K. K. 1994, in Multi-Wavelength Continuum Emission of AGN, ed. T. J. -L. Courvoisier & A. Blecha (Dordrecht: Reidel), 401

Padovani, P. 1998, in New Horizons from Multi-Wavelength Sky Surveys, IAU 179 Symposium, ed. B. J. McLean, D. A. Golombek, J. J. E. Hayes & H. E. Payne (Dordrecht: Kluwer), 257

Pérez, E., Penston, M. V., & Moles, M., 1989, MNRAS, 239, 55, 75

Pérez, E., Robinson, A., & de la Funte, L. 1992, MNRAS, 256, 103

Penston, B.M. 1991, in Variability of Active Galaxies, ed. Duschl, W.J., Wagner, S.J., and Camenzind, M. (Berlin: Springer-Verlag), 47

Penston, M. V., Penston, M. J., & Sandage, A. 1971, PASP, 83, 783

Peterson, B. M. 1988, PASP, 100, 18

Peterson, B. M. 1991, ApJ, 368, 119

Peterson, B. M. 1993, PASP, 105, 247

Peterson, B. M. 1997, 'An intoduction to Active Galactic Nuclei', (Cambridge Uneversity Press)

Peterson, B. M., Pogge, R. W., Wanders, I., Smith, S. M., & Romanishin, W. 1995, PASP, 107, 579

Peterson, B. M., & Cota, S. A. 1988, ApJ, 330, 111

Peterson, B. M., & Wandel A. 1999, ApJL, submitted (astro-ph/9905382)

Peterson, B. M. & Gaskell, C. M. 1991, ApJ, 368, 152.

Peterson, B. M., Wanders, I., Bertram, R., Hunley, J. F., Pogge, R. W., & Wagner, R. M. 1998a, ApJ, 501, 82

Peterson, B. M., Wanders, I., Horne, K., Collier, S., Alexander, T., Kaspi, S., & Maoz, D. 1998b, PASP, 110, 660

Peterson, B. M., et al. 1994, ApJ, 425, 622

Peterson, B. M., et al. 1999, ApJ, 510, 659

Pijpers, F. P., & Wanders, I. 1994, MNRAS, 271, 183

Press, W. H., Teukolsky, S. A., Vetterling, W. T, & Flannery, B. P. 1992, Numerical Recipes, Second Edition (Cambridge: University press), 660

Prestwich, A. H., Wright, G. S., & Joseph, R. D. 1992 ApJS, 80, 205

Reichert, G. M., et al. 1994, ApJ, 425, 582

Robinson, A. 1994, in Reverberation Mapping of the Broad-Line Region in AGN, ed. P. M. Gondhalekar, K. Horne, & B. M. Peterson (San Francisco: ASP), 152

Rodríguez-Pascual, P. M., et al. 1997, ApJS, 110, 9

Romano, P., & Peterson, B. M. 1999, in Structure and Kinematics of Quasars Broad Line Regions, eds. Gaskell, C. M., Brandt, W. N., Dietrich, M., Dultzin-Hacyan, D., and Eracleous, M. San Francisco: ASP), in press

Romano, P., Marziani, P., & Dultzin-Hacyan, D. 1998, ApJ, 495, 222

Sitko, M. L. 1990, ApJS, 72, 777

Santos-Lleó, M., et al. 1997, ApJS, 112, 271

Santos-Lleó, M., et al. 1999, in preparation

Savage, B. D., & Mathis, J. S. 1979, ARA&A, 17, 73

Schmidt M., & Green, R. F. 1983, ApJ, 269, 352

Seaton, M. J. 1979, MNRAS, 187, 73

Shields, C. J., Ferland, G. J., & Peterson, B. M. 1995, ApJ, 441, 507

Sitko, M. L. 1990, ApJS, 72, 777

Stirpe, G. M., et al. 1994, ApJ, 425, 609

Tagliaferri, G., Bao, G., Israel, G. L., Stella, L., & Treves, A. 1996, ApJ, 465, 181

Ulrich, M.H., Courvoisier, T.J.-L., & Wamsteker, W. 1993, ApJ, 411, 125

Usher, P.D. 1978, ApJ, 222, 40

van Groningen, E., & Wanders, I., 1992, PASP, 104, 700

Wamsteker W., et al. 1990, ApJ, 354, 446

Wandel A., & Boller, T. 1998, A&A, 331, 884

Wandel, A., & Yahil, A. 1985, ApJ, 295, L1

Wandel, A., Peterson, B. M., & Malkan M. A. 1999, ApJ, in press (astro-ph/9905224)

Wanders, I. 1994, in Reverberation Mapping of the Broad-Line Region in AGN, ed. P. M. Gondhalekar, K. Horne, & B. M. Peterson (San Francisco: ASP), 127

Wanders, I., & Peterson B. M. 1996, ApJ, 466, 174

Wanders, I., et al. 1997, ApJS, 113, 69

Warwick, R. S., et al. 1996, ApJ, 470, 349

Welsh, W. F., Peterson, B. M., Koratkar, A. P., & Korista, K. T. 1998, ApJ, 509, 118

White, R. J., & Peterson, B. M. 1994, PASP, 106, 879

Wills, B. J. 1999, in Quasars and Cosmology, A.S.P. Conference Series, ed. G. Ferland, J. Baldwin (San Francisco: ASP)

Wills, B. J., Netzer, H., and Wills, D. 1985, ApJ, 288, 94

Winge, C., Peterson, B. M., Horne, K., Pogge, R. W., Pastoriza, M. G., & Storchi-Bergmann, T. 1995, ApJ, 445, 680

Winge, C., Peterson, B. M., Pastoriza, M. G., & Storchi-Bergmann, T. 1996, ApJ, 469, 648

Wisotzki, L., Wucknitz, O., Lopez, S., & Sorensen, A. N. 1998, A&A, 339, L73

Woltjer, L., 1990, in Active Galactic Nuclei, ed. Courvoisier, T.J.-L., and Mayor M. (Berlin: Springer-Verlag), 1

Yaqoob, T., Warwick, R. S., Makino, F., Otani, C., Sokoloski, J. L., Bond, I. A., & Yamauchi, M. 1993, MNRAS, 262, 435

Zamorani, G., Giommi, P., Maccacaro, T., & Tananbaum, H. 1984, ApJ, 278, 28

Zheng, W. 1988, ApJ, 324, 801

Zheng, W., & Burbidge E. M., 1986 ApJ, 306, L67

Zheng W., Burbidge, E. M., Smith, H. E., Cohen, R. D., & Bradley, S. E. 1987, ApJ, 322, 164

Zheng W., Kriss, G. A., Telfer. R. C., Grimes, J. P., & Davidsen A. P. 1997, ApJ, 475, 469

תקציר

מטרת עבודה זו היא למדוד את הגודל של אזור הקווים הרחבים בגרעינים פעילים של גלקסיות ולקבוע יחסים תצפיתיים בין הבהירות, המסה וגודל אזור הקווים הרחבים באובייקטים אלו. העבודה כוללת תוצאות מתצפיות חדשות בשילוב נתונים מהספרות וכמו כן מודלים תאורטים חדשים של גרעינים פעילים של גלקסיות.

הפרק השני של תזה זו מציג תוצאות מפרוייקט ניטור ספקטרופוטומטרי, בעזרת טלסקופים קרקעיים, של גלקסית הסיפרט **NGC4151**. לא נמצאו כל עדויות להפרש זמנים בין השינויים בשטף הרצף בתחום האופטי לבין השינויים בשטף הרצף והקווים בתחום העל-סגול. עבור קווי הפליטה **Hα** ו-**Hβ** מצאנו הפרש זמנים של 0-3 ימים, בשונה מאוד מתוצאות קודמות בהן נמצא הפרש זמנים של 9±2 ימים. הבדל זה יכול לנבוע מסקלת זמן שונה של השתנות הרצף *המיינן*, או כתוצאה משינוי אמיתי בהתפלגות הגז באזור הקווים הרחבים.

תוצאות מפרוייקט ניטור ספקטרופוטומטרי של 28 קוואזרי פאלומר-גרין, שנמשך 7.5 שנים, מוצגות בפרק השלישי. זמן הדגימה האופייני הוא 1-4 חודשים עם 20-70 תצפיות בכל אובייקט. בכל האובייקטים מצאנו שנויים בשטף הרצף ובקווי הפליטה. ב- 17 אובייקטים בהם הדגימה היתה מספיק טובה, מצאנו שהשינויים בעוצמת שטף קווי בלמר עוקבים אחרי השינויים בעוצמת הרצף, עם הפרש זמן מסדר גודל של 100 ימים. עבודת מחקר זו מרחיבה לכן את טווח הבהירות של גרעינים פעילים, לצורך חקירת היחסים בין גודל מסה ובהירות, בשני סדרי גודל ומכפילה את מספר האובייקטים. כאשר אנו משלבים, בפרק הרביעי, את התוצאות עבור 17 הקוואזרים עם תוצאות עבור 17 גלקסיות סיפרט 1 שנמדדו בעבר, אנו מוצאים שגודל אזור הקווים הרחבים פרופורציוני לבהירות האובייקט (באורך גל של **5100Å**) בחזקת 0.70±0.03, בשונה באופן משמעותי ממחקרים קודמים ומתחזיות תאורטיות פשוטות. תוצאה זו מרמזת שפרמטר היינון בגרעינים הפעילים הוא פונקציה יורדת של הבהירות. כאשר מניחים שתנועות הגז הפולט קווים נשלטות ע״י גרביטציה, אנו מוצאים שהמסה המרכזית פרופורציונית לבהירות בחזקת 0.5±0.1. תוצאה זו אינה עקבית עם ההנחה שבכל גרעיני הגלקסיות בהירות הגרעין הפעיל היא שבר קבוע של בהירות אדינגטון. בנוסף אנו מוצאים אנטיקורלציה בין הרוחב במחצית הגובה של קווי בלמר לבין בהירות הגרעינים הפעילים, כך שהרוחב תלוי בבהירות בחזקת 0.27±0.01-.

לסיום, בפרק החמישי מוצג מודל חדש עבור אזור הקווים הרחבים. המודל כולל חישובי פוטו-יינון עבור מספר רב של עננים בגיאומטריה קבועה מראש והשוואה של עוצמת הקוים המחושבים מהמודל עם עקומות האור התצפיתיות של קווים אלו. התאמת מספר קווים בו זמנית מאפשרת הגבלה של פרמטרי המודל, כמו צפיפות החלקיקים וצפיפות העמוד באזור הקווים הרחבים, צורת הרצף המיינן והפיזור הרדיאלי של העננים פולטי הגז. יישום המודל לגבי גלקסית הסיפרט **NGC5545** איפשר לנו לשחזר בהצלחה 4 עקומות אור של קווי פליטה שונים בתחום העל-סגול של הספקטרום.

עבודה זו מוקדשת לזיכרם של אחי ואבי, רונן ושאול כספי, אשר עזרו לי ועודדו אותי *במהלך עבודה זו אך לדאבוננו לא זכו לראות בהשלמתה.*

עבודה זו נעשתה בהנחייתו של

פרופסור חגי נצר

בית הספר לפיסיקה ואסטרונומיה

אוניברסיטת תל אביב

TEL AVIV UNIVERSITY אוניברסיטת תל-אביב

RAYMOND AND BEVERLY SACKLER
FACULTY OF EXACT SCIENCES
SCHOOL OF PHYSICS & ASTRONOMY

הפקולטה למדעים מדוייקים
ע"ש ריימונד ובברלי סאקלר
בית הספר לפיסיקה ואסטרונומיה

השתנות קווים ורצף
ויחסי גודל-מסה-בהירות
בגרעינים פעילים של גלקסיות

חיבור לשם קבלת התואר "דוקטור לפילוסופיה"

מאת

שי כספי

הוגש לסנאט של אוניברסיטת תל-אביב

אלול תשנ"ט